8-24-2015

Optical Measurements of Whitecaps and Bubbles During Large Scale Wave Breaking in the Southern Ocean

Kaylan L. Randolph
University of Connecticut - Storrs, kaylan.randolph@uconn.edu

Optical Measurements of Whitecaps and Bubbles During Large Scale Wave Breaking in the Southern Ocean

Kaylan Randolph

University of Connecticut

2015

Abstract

Wave breaking contributes to climate relevant processes, such as the production of sea salt aerosols and the exchange of gas (*e.g.* CO_2, CH_4, DMS, water vapor) and heat between the ocean and atmosphere. Quantifying these processes, however, has been hampered by the lack of field data under high wind conditions and the inherent challenges in measuring whitecaps. Here, optical tools were developed to estimate metrics of whitecaps and bubbles associated with wave breaking along the polar front zone of the Atlantic sector of the Southern Ocean. In this study, wind speeds exceeded 15 m s^{-1}, significant wave heights routinely surpassed 4 m, fractional whitecap coverage exceeded 5%, and bubble plumes penetrated to over 10 m depth in the water column. With a single channel above-water radiometer mounted on a ship, metrics were developed to quantify wave breaking intensity, duration and decay rate, and fractional whitecap coverage. Radiometric estimates of whitecap coverage followed a cubic dependence with wind speed and captured more of the decaying bubble plume area than methods using high-resolution digital imagery. Optical measurements of the near forward volume scattering function and the critical scattering angle for bubbles (~80°) were used to detect deeply penetrating bubbles ranging from 0.5 to 125 μm radius. When extrapolated to 4 m depth, our estimates suggest that the small bubbles here could be supplying ~36% of the total void fraction and likely contributed to the supersaturation of low solubility gases. Finally, preliminary results from a least-squares inversion technique applied to measurements of the bulk optical volume scattering function suggest that a persistent, small (mode radius~0.2 μm) bubble population with a narrow size distribution contributed between 5% (low wind) and 20% (high wind) to the total backscattering during the experiment. Under high wind conditions, foam

and bubbles serve to enhance the magnitude and alter the spectral distribution of light leaving the surface ocean, which can impact penetration of light to depth and associated heating rates. These optical tools can be used to better quantify air-sea processes related to wave breaking throughout the ocean and the potential impact on global climate.

Optical Measurements of Whitecaps and Bubbles During Large Scale Wave Breaking in the Southern Ocean

Kaylan Randolph

B.S. Indiana University 2005

M.S. Indiana University 2007

A Dissertation

Submitted in the Partial Fulfillment of the

requirements for the degree of

Doctor of Philosophy

at the

University of Connecticut

2015

Approval Page

Doctor of Philosophy Dissertation

Optical Measurements of Whitecaps and Bubbles During Large Scale Wave Breaking in the Southern Ocean

Presented by

Kaylan Randolph

Major Advisor_____
Heidi M. Dierssen

Associate Advisor_____
James B. Edson

Associate Advisor_____
Edward C. Monahan

Associate Advisor_____
Michael S. Twardowski

University of Connecticut

2015

Acknowledgements

This dissertation is the product of effort by many. My education and the science presented here is the result of the undying commitment of my committee members, a group of incredible professors, and my family.

From the first moment I met her, Dr. Heidi Dierssen provided energy, opportunities, and brilliant ideas through which I gained an incredible education and confidence. She immediately introduced me to many of her colleagues in the Ocean Optics community—a group of people I am honored to know, learn from, and work with. Her first introduction was Dr. Michael Twardowski, who quickly became a key member of my advisory committee. Through his brilliance, patience and guidance, I learned how to do science, as opposed to just thinking about it. Fortunately, Dr. James B. Edson also agreed to serve on my committee—his mountain of experience, good nature and cleverness took me, and this work, far. My final committee member, Dr. Edward C. Monahan, committed himself completely to this work and to me as his student. His conscientiousness, generosity, and effective teaching were vital to my education and this investigation. The professors at the University of Connecticut, Avery Point are talented in their research and in educating. Some have since retired and I feel so fortunate to have sat in their classrooms. I owe a debt of gratitude to two professors in particular, Drs. James O'Donnell and Dmitriy Leykekhman who spent hours upon hours teaching me concepts, which were often, admittedly, brand new. They introduced new ways of thinking altogether—I am so very grateful.

I so appreciate the Marine Sciences community at Avery Point. The support of the staff is truly unmatched and the graduate student community is so generous with encouragement. I came through the program with John Doyle, Yunyun Zhuang, and Alejandro Cifuentes—three people with whom I spent many hours and look forward to spending many more. I also thank my labmates, Dirk Aurin and Chris Buonassissi, whom I loved working with.

My family has supported all of my adventures in every single way possible and this has been no exception. They seem to have an infinite amount of patience, time, thoughts and advise for me. Also, the love, encouragement, and generosity I receive from my family in Chile has touched me to the core. Alejandro Cifuentes, my husband and favorite collaborator, was and is instrumental to this work. He often has a diametrically different perspective from my own, for which I am so thankful. He has taught me more than I could have every hoped or dreamed to learn from one individual.

This work was largely funded by a grant awarded to Dr. Heidi Dierssen by NASA's Ocean Biology and Biogeochemistry Program. I am eternally grateful.

Table of Contents

1. Introduction……1
   1.1. Background……..1
   1.2. Objectives……2
   1.3. Approach……..3
2. Optical measurements of small deeply penetrating bubble populations generated by breaking waves in the Southern Ocean……..7
3. Novel methods for optically measuring whitecaps under natural wave breaking conditions parameterized in the Southern Ocean……28
   3.1. Introduction……30
   3.2. Background……...33
      3.2.1. Radiometric Quantities……...33
      3.2.2. Time-to-space comparison.……34
   3.3. Development of Method……36
      3.3.1. Instruments and configuration……..36
      3.3.2. Identifying Whitecap Features……..37
      3.3.3. Wave breaking metrics……..41
   3.4. Measurements……43
      3.4.1. Radiometry……44
      3.4.2. Upper Ocean Dynamics……45
   3.5. Assessment……46
   3.6. Conclusions……65
4. Evaluation of the spectral reflectance of whitecap and bubbles on ocean color remote sensing…..…77
   4.1. Background……97
   4.2. Methodology……..……...80
      4.2.1. Radiometry……..……...81
      4.2.2. Whitecap detection and metrics……82
      4.2.3. Meteorological and oceanographic measurements…..…….83
      4.2.4. Time-to-space comparison……83
      4.2.5. Optical and analytical measurements……84
   4.3. Results and discussion……..……84
      4.3.1. The wind speed-whitecap coverage relationship……..……84
      4.3.2. Enhancement in the mean spectral reflectance due to whitecaps…….86
      4.3.3. Reflectance of individual whitecaps……89
   4.4. Conclusions……..106
5. Epilogue……...107
   5.1. Background……..107
   5.2. Methodology…..……..……...110
      5.2.1. Measurements of the volume scattering function and inversion technique.……111

5.2.2. Validation dataset……113
5.3. Results and discussion……114
5.3.1. The VSF classification of particle populations……117
5.4. Future directions for the quantification of the bubble signal in remote sensing of ocean color and uncertainty analysis……122
5.5. Appendix A. ……122

1. Introduction

1.1. Background

Breaking waves on the ocean surface are areas of significant importance to air-sea interaction. Whitecaps foster climate relevant physical and chemical processes in the ocean, including the production of sea salt aerosols, mixing processes, and air-sea gas (*e.g.* CO_2, CH_4, DMS, etc.) and heat exchange. Efforts to parameterize these processes in climate models incorporate whitecap coverage (*e.g.*, Monahan and Spillane [1984], Liss and Merlivat [1986], Asher *et al.* [2002], Fairall *et al.* [2003]). The parameterizations have been developed by coupling coverage estimates from high-resolution digital images and simultaneously collected meteorological and oceanographic measurements (*e.g.* wind speed, friction velocity, near-surface atmospheric stability, etc.; see Goddijn-Murphy *et al.* [2011]). More recent approaches to measuring whitecap coverage include the use of both the traditional thresholding technique applied to digital imagery and a spatial separation technique, used to differentiate stage A and B coverage based on the wave field, brightness, texture, and slope [*Callaghan and White*, 2009; *Scanlon and Ward*, 2013]. However, these traditional methods can miss a portion of the mature whitecap and bubble plume that is responsible for the production of sea-salt aerosols and can impact heat flux [*Monahan et al.*, 1986; *Andreas et al.*, 1995]. Hence, accurate measurements of whitecap coverage and the associated bubble populations are sought after.

Whitecaps and bubbles also have a pronounced effect on the magnitude and shape of visible light leaving the ocean surface (*e.g.*, Moore *et al.* [2000], Stramski and Tegowski [2001], Terill *et al.* [2001], and Zhang *et al.* [2002]). The magnitude of light reflected from the sea surface can be significantly enhanced due to foam and bubble entrainment from breaking waves on temporal scales of seconds to minutes. Remote sensing of foam shows a spectrally flat response, but as the whitecap matures marked spectral shape changes occur. Bubbles also have a unique optical signature: an air bubble in water has a relative refractive index of 0.75 and so a bubble that is large relative to the wavelength of light will produce

internal reflection within the water medium at approximately 82°, dubbed "the critical scattering angle." The scattering efficiency for bubbles at this angle is an order of magnitude greater than other oceanic particle types [Zhang et al., 2002]. If air bubbles are present in the water column, enhanced scattering at the critical angle will be observed and can be measured using volume scattering sensors [Zhang et al., 2002; Twardowski et al., 2012]. Consequently, optical and radiometric techniques can be used to measure both foam and bubbles generated by whitecaps.

Ocean color imagery and limited field data suggest that the Southern Ocean has high remote sensing reflectance (R_{rs}) relative to other oceans (Figure 1a). Other studies have attributed very high backscattering in the polar front zone of the Southern Ocean to elevated concentrations of unidentified very small particles (*e.g.*, Reynolds *et al.* [2001]) and of calcite producing coccolithophores (*e.g.* Balch *et al.* [2011]). Using optical methods, this thesis will address whether high backscattering in the Southern Ocean may be also be associated with whitecaps and bubble entrainment by breaking waves from the consistent high winds in the region, which elevate the amount of upward radiance from the sea surface (Figure 1b).

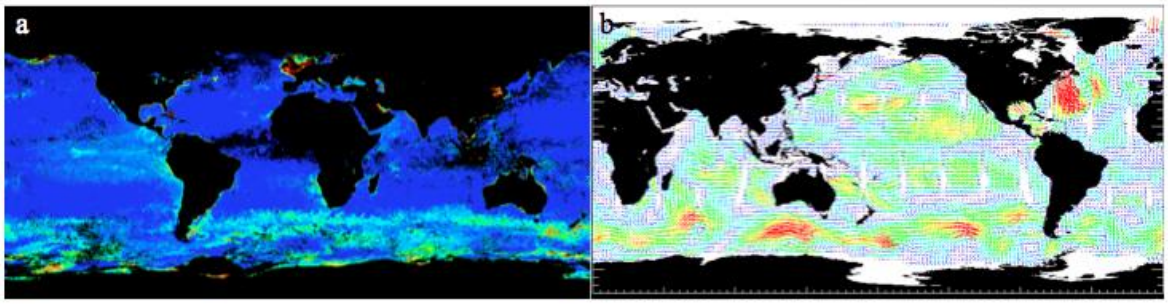

Figure 1: The bright Southern Ocean waters showing unusually high (a) normalized water leaving radiance (nL_w555) measured by MODIS AQUA (b) and mean wind speeds measured by QuikSCAT during March 2008.

1.2. General Objectives

Here, optical and radiometric tools and novel analyses are used to measure whitecaps, bubbles, and other particles during a large range of wind and wave conditions along the polar front zone of the Atlantic sector of the Southern Ocean as a part of the Southern Ocean Gas Exchange Experiment [*Ho et al.*, 2011]. Questions related to whitecap coverage (*i.e.*, stage A and B) and bubble entrainment (*i.e.* size distribution and concentration) are addressed with the goal of fulfilling three objectives. The first objective is to estimate the size distribution, concentration, and evolution of bubble populations introduced by breaking waves in a high wind environment and to assess their potential contribution to the supersaturation of low solubility gases (Chapter 2). The second objective is to develop novel optical methods to estimate wave breaking statistics, including the fractional coverage, duration, decay rate, and average brightness (*e.g.*, albedo) of whitecaps using above water radiometry from ships (Chapter 3). The third is to assess the spectral nature of whitecaps and their contribution to ocean color (Chapter 4). Finally, to address the hypothesis that at least a portion of the elevated reflectance measured using ocean color sensors in the Southern Ocean is due to bubbles, the relative contribution of backscattering material (*e.g.*, bubbles, coccolithophores and coccoliths, colloids, diatoms, and other phytoplankton species) was estimated and preliminary results from the investigation are presented in the epilogue.

1.3. Approach/strategy

In this thesis, an investigation on the contribution of bubbles and foam to backscattering in the Southern Ocean, specifically during times of strong physical forcing (*e.g.*, high winds) is presented. This investigation was conducted as a part of the Southern Ocean Gas Exchange Experiment (SOGasEx) on the NOAA R.V. Ronald H. Brown in the Atlantic sector of the Southern Ocean (50°S 40°W), March 7, 2008 through April 4, 2008 (Figure 2). The primary objective of SOGasEx was to measure gas transfer at high wind speeds (> 10 m s^{-1}, long fetch) and to identify additional predictors, aside from wind, for estimating gas transfer (Ho *et al.*, 2011). A Lagrangian approach was taken to study biogeochemical processes and two tracer patches of 4800 L of SF_6 and ^3He infused seawater, referred to as Patch 1 and Patch 2, were deployed during the experiment (Figure 2; Ho *et al.*, 2011).

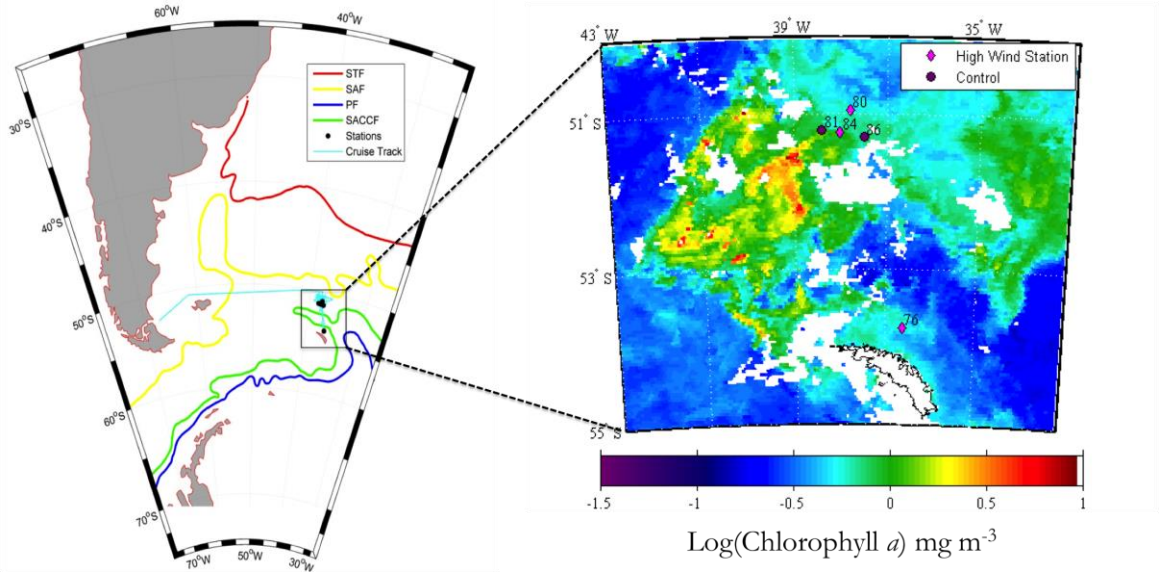

Figure 2: South Atlantic sampling region and station locations (18 total) overlayed on the satellite-derived average chlorophyll (mg m^{-3}) from the MODIS Aqua sensor (nominal 4 km resolution) for the month of March 2008. The white patches in the image indicate areas with no data due to cloud-cover.

In Chapter 2, light scattering measurements, collected at high frequency in the surface water of the Southern Ocean during high wind conditions, are used to identify and estimate the size distribution of bubble populations generated by large-scale wave breaking. The optical approach extends the bubble size distribution toward smaller sizes than are routinely measured using acoustical methods. The hypothesis that the deeply penetrating, very small bubbles (<60 um) make a significant contribution to the total void fraction and the supersaturation of low solubility gases is explored by extrapolating the bubble size distributions measured here to shallower depths and applying the model of *Woolf and Thorpe* [1991].

The hypothesis that, because of the high backscattering efficiency of foam and bubbles, measurements of upwelling radiance can be used to retrieve whitecap metrics is explored in Chapter 3. If so, above-water radiometry can provide a simple and robust methodology for estimating whitecap coverage, breaking intensity and decay rates. A different sampling approach and viewing geometry is used for the ship-based radiometric method compared to the traditional digital imaging approach for estimating whitecap coverage; therefore, validation exercises are applied to identify the portion of the whitecap feature captured by each measurement technique. Finally, because estimates of gas transfer and sea salt aerosol production are still estimated using parameterizations based on wind speed, the optimal fit of the radiometrically estimated whitecap coverage to the instantaneous wind speed is investigated.

In addition to an enhancement in the magnitude of reflectance, whitecaps also show a marked influence on the spectral shape of reflectance, producing errors in the correction routines used to process ocean color imagery and in the estimation of ocean color derived biogeochemical parameters from space. In Chapter 4, the whitecap correction routine used to process ocean color imagery is evaluated for its effectiveness in the Southern Ocean using optical, radiometric, meteorological and oceanographic measurements collected during the Southern Ocean Gas Exchange Experiment. The mean spectral enhancement in reflectance over a large footprint (~1 km^2) due to the presence of whitecaps and the average spectral lambertian equivalent reflectance of individual whitecaps are presented.

Finally, initial analyses on the contribution of individual particle (including bubble) populations to backscattering in the energetic Southern Ocean are presented in the epilogue. With the goal of understanding reflectance under the influence of whitecaps, the contribution by bubbles, very small particles or colloids, coccolithophores and detached coccoliths, and other phytoplankton species to the total backscattering is explored using a least-squares inversion technique applied to surface measurements of the bulk optical volume scattering function. The results of the inversion are validated using field measurements of bubbles, acid labile backscattering, and the size-fractionated phytoplankton assemblage.

Collectively, these investigations begin to explore the hypothesis that optical backscattering and reflectance has variable causes and is driven by both biological and physical processes.

2. Optical measurements of small deeply-penetrating bubble populations generated by breaking waves in the Southern Ocean

This chapter was published in the Journal of Geophysical Research in December 2014 (Randolph, K., H. M. Dierssen, M. Twardowski, A. Cifuentes-Lorenzen, and C. J. Zappa (2013), Optical measurements of small deeply penetrating bubble populations generated by breaking waves in the Southern Ocean, J. Geophys. Res. Oceans, 119, 757–776, doi:10.1002/2013JC009227)

AGU PUBLICATIONS

JGR

Journal of Geophysical Research: Oceans

RESEARCH ARTICLE

10.1002/2013JC009227

Key Points:

- Bubble size distributions (0.5–60 μm radius) were measured during wave breaking
- Bubbles $\leq$30 μm in radius supplied ~30% of the void fraction at 4 m depth
- Bubble populations were presented in the context of wind and wave conditions

Correspondence to:
K. Randolph,
kaylan.randolph@uconn.edu

Citation:
Randolph, K., H. M. Dierssen, M. Twardowski, A. Cifuentes-Lorenzen, and C. J. Zappa (2013), Optical measurements of small deeply penetrating bubble populations generated by breaking waves in the Southern Ocean, *J. Geophys. Res. Oceans*, *119*, doi:10.1002/2013JC009227.

Received 16 JULY 2013
Accepted 4 JAN 2014
Accepted article online 10 JAN 2014

Optical measurements of small deeply penetrating bubble populations generated by breaking waves in the Southern Ocean

Kaylan Randolph[1], Heidi M. Dierssen[1], Michael Twardowski[2], Alejandro Cifuentes-Lorenzen[1], and Christopher J. Zappa[3]

[1]Department of Marine Sciences, University of Connecticut, Groton, Connecticut, USA, [2]WET Labs Inc., Narragansett, Rhode Island, USA, [3]Lamont-Doherty Earth Observatory of Columbia University, Palisades, New York, USA

Abstract Bubble size distributions ranging from 0.5 to 125 μm radius were measured optically during high winds of 13 m s^{-1} and large-scale wave breaking as part of the Southern Ocean Gas Exchange Experiment. Very small bubbles with radii less than 60 μm were measured at 6–9 m depth using optical measurements of the near-forward volume scattering function and critical scattering angle for bubbles (~80°). The bubble size distributions generally followed a power law distribution with mean slope values ranging from 3.6 to 4.6. The steeper slopes measured here were consistent with what would be expected near the base of the bubble plume. Bubbles, likely stabilized with organic coatings, were present for time periods on the order of 10–100 s at depths of 6–9 m. Here, relatively young seas, with an inverse wave age of approximately 0.88 and shorter characteristic wave scales, produced lower bubble concentrations, shallower bubble penetration depths, and steep bubble size distribution slopes. Conversely, older seas, with an inverse wave age of 0.70 and longer characteristic wave scales, produced relatively higher bubble concentrations penetrating to 15 m depth, larger bubble sizes, and shallower bubble size distribution slopes. When extrapolated to 4 m depth using a previously published bubble size distribution, our estimates suggest that the deeply penetrating small bubbles measured in the Southern Ocean supplied ~36% of the total void fraction and likely contributed to the transfer and supersaturation of low-solubility gases.

1. Introduction

Bubble populations are recurrently introduced into the surface ocean by wind-generated, large-scale breaking waves. During high wind regimes, the transfer of lower-solubility gases (i.e., N_2 and O_2) is thought to become largely a bubble-mediated process [*Broecker and Siems*, 1984; *Woolf and Thorpe*, 1991; *Vagle et al*., 2010]. Small, deeply penetrating bubbles dissolve even when the gas is saturated with respect to the atmosphere due to hydrostatic pressure and surface tension effects. As depth increases, the supersaturating effect of bubbles increases and the range of bubble sizes contributing to the gas flux narrows and shifts toward smaller sizes [*Woolf*, 1997; *Vagle et al*., 2010]. The smallest bubbles collapse completely contributing 1–2 times more to the gas flux than the large bubbles that transfer only a fraction of their volume before rising out of the water column [*Hamme and Emerson*, 2006]. To date, bubble measurements, particularly in the smallest size ranges, are incomplete largely due to technological limitations [*Woolf et al*., 2007].

Optical and acoustical techniques have been utilized for measuring oceanic bubble size distributions. Acoustical methods have been developed to sample the entire bubble cloud at high temporal and spatial resolution. The most commonly employed technique uses measurements of acoustical attenuation at multiple frequencies corresponding to the resonant frequencies of the bubbles present [*Medwin*, 1970; *Medwin and Breitz*, 1989; *Farmer et al*., 1998; *Vagle and Farmer*, 1998]. Generally, resonant peaks over a frequency range of 5–400 kHz are used to capture bubble sizes from 20 to 500 μm in radius.

Past studies have used optical methods to resolve bubbles with radii as small as 10 μm [*Su et al*., 1987; *O'Hern et al*., 1988], but such methods sample only small volumes of water (generally mm^3 to cm^3) and cannot easily resolve the spatial and temporal variability inherent to bubble plumes. One of the most frequently cited bubble data sets was acquired using a photographic method [*Johnson and Cooke*, 1979]. More recently, *Deane and Stokes* [2002] used a video microscope to capture images of bubble plumes at time

periods on the order of milliseconds, but only bubbles larger than ~80 μm in radius were measured. Consequently, the shape of the bubble size distribution in the small size classes is still in question.

Here new technology based on light scattering properties is used to identify bubbles in the water column and to estimate bubble size distributions during large-scale wave breaking (section 3.1). An air bubble in water has a relative refractive index of 0.75 and so bubbles produce a unique pattern of scattering. A bubble that is large relative to the wavelength of light will produce internal reflection within the water medium at approximately 82°, dubbed "the critical scattering angle." The scattering efficiency for bubbles at this angle is an order of magnitude greater than other oceanic particle types [*Zhang et al*., 2002]. No other natural mechanism is known to augment scattering at this angle in oceanic waters. If air bubbles are present in the water column, enhanced scattering at the critical angle will be observed and can be measured using volume scattering sensors [*Zhang et al*., 2002; *Twardowski et al*., 2012]. In addition, optical methods based on laser diffraction are used to estimate the size distribution of oceanic particles, including bubbles [*Agrawal and Pottsmith*, 2000].

Bubble size distributions from 0.5 to 125 μm radius, measured optically at 6–9 m depths, are presented here. These bubbles were measured in open ocean conditions during the Southern Ocean Gas Exchange Experiment (SO GasEx) [*Ho et al*., 2011]. A portion of the bubble size distribution extends toward smaller size classes than previously measured, however, where the size distribution overlaps with those previously reported, the shape and slope were compared for consistency (section 3.2). The evolution of each bubble event was traced through time using the high-frequency (1 Hz) measurements of bubble number concentration and size distribution slope (section 3.3).

Bubble size distributions and bubble plume characteristics are a direct result of the wind and wave conditions. Therefore, the bubble observations measured here were coupled with wind and wave statistics to aid in the interpretation of the bubble size distribution, slope and number concentration, bubble plume penetration depth, and void fraction (section 3.4). In order to assess the significance of small bubbles (<30 μm) to the total void fraction, an extrapolation of the bubble size distribution to 4 m was conducted (section 3.5). Finally, the potential bubble-mediated air-sea transfer of low-solubility gases (i.e., O_2) was considered within the context of dissolved gas measurements presented by *Moore et al*. [2011] and by extension of the *Woolf and Thorpe* [1991] wind-based oxygen supersaturation model to the smaller bubble sizes measured here (section 3.6).

2. Methodology

This investigation was conducted on the NOAA ship the *R.V. Ronald H. Brown* in the Atlantic sector of the Southern Ocean (50°S, 40°W), 7 March to 4 April 2008. The primary objective of SO GasEx was to measure gas transfer at high wind speeds (>10 m s^{-1}) and to identify predictors, in addition to wind, for estimating gas transfer [*Ho et al*., 2011]. A Lagrangian approach was taken to study relevant chemical and biological processes. Two tracer patches were deployed lasting 6 and 15 days in duration, respectively. This study focuses on five total stations, including two stations sampled during high wind conditions and two control stations (sampled during low wind conditions) within Patch 2 and a single station sampled during high wind conditions 300 km north of South Georgia Island.

2.1. Optical Measurements

An optical package was deployed close to noon daily in the center of the patch area. Sensors on the package included a MASCOT volume scattering meter (WET Labs) and a LISST-100X diffractometer particle size analyzer (Sequoia Scientific, Inc.), positioned 15 cm apart. The optical package was suspended approximately 3 m from the starboard side of the ship using a winch. Measurements were collected as a 30 min time series. As a result of the strong wind and wave conditions, the package was deployed at deeper (>5 m) depths and oscillated vertically between 6 and 9 m. The close proximity of the package to the ship during deployment was not ideal and some contamination could have resulted. However, the location of the winch relative to the ship's thrusters (12–26 m distance) and the position of the ship while on-station, with the bow heading into the wind, helped to minimize these effects.

Bubble populations were determined using both the MASCOT measurements of the wide-angle volume scattering function and the LISST measurements of the particle size distribution. The presence of bubbles was identified based on enhancements in the volume scattering function at the critical angle. The

measurement of particle size distribution, determined from the near-forward diffraction of light, distinguished particles primarily on size and not composition. Hence, the measured concentration of particles included all suspended particles, as well as bubbles. During high wind and wave events, simultaneous enhancements occurring in both the VSF at the critical angle and in the particle concentration measured using the LISST were indicative of bubbles (see below).

2.1.1. Measurements of Critical Angle Scattering

Bubbles were detected from enhancements in critical angle scattering, determined from measurements of the volume scattering function (VSF). The VSF, $\beta(\theta)$, describes the angular distribution of scattered light

$$\beta(\theta)=dI(\theta)/EdV \quad (\mathrm{m}^{-1}\mathrm{sr}^{-1}) \tag{1}$$

where I is the scattered intensity in the direction θ by the volume dV, with incident irradiance E. The VSF between 10° and 170° (in 10° increments) was measured at high frequency (20 Hz) using a MultiAngle SCattering Optical Tool (MASCOT, WET Labs). Details of the MASCOT design, calibration, and data processing are described in *Sullivan and Twardowski* [2009] and *Twardowski et al*. [2012].

The shape of the VSF augmentation at the critical angle, relative that that measured during low wind conditions, is indicative of the concentration of the bubbles present. Critical angle scattering observations containing bubbles were identified by comparing the distribution of the high wind observations to a single control, calculated as the mean of the measurements collected during low wind speeds and no wave breaking. The critical angle scattering data from each station were normalized by the sum of the data record to facilitate the direct comparison of distribution shapes. The appropriate statistical distribution was applied to the data using the Kolmogorov-Smirnof test ($\alpha = 0.05$) as the metric for determining the optimal fit. Statistical measures were calculated accordingly. Measurements of bubbles were identified as the portion of the probability density function of critical angle scattering measurements collected during high winds not intersecting with the distribution of the control.

2.1.2. Measurement of Bubble Size Distributions

Measurements of the particle size distribution (PSD), the size and number of all particles 0.5–125 μm in radius, including bubbles, were determined using the LISST-100X Type B (Laser In Situ Scattering and Transmissiometry, Sequoia Scientific, Inc.). The LISST measures laser diffraction, specifically the near-forward volume scattering function (0.07°–15° in water), at 32 logarithmically spaced silicon ring detectors. The volumetric particle concentration is nominally determined using the scattering intensity across the 32 detectors and an inverse transform based on Mie theory. The term "particle" here includes organic, inorganic, and air-filled (bubble) particles. The term "particulate" refers to all solid particles (i.e., inorganic and organic particles) and excludes bubbles. LISST data were processed following *Agrawal and Pottsmith* [2000] and *Andrews et al*. [2011]. Issues exist with the matrix inversion of the LISST raw scattering data, particularly at the large angles, which correspond to the smallest particle sizes. A "rising tail" in the particle size distribution can result when high concentrations of submicron particles are present. The raw scattering measurements were filtered using a three-point running average to smooth small irregularities caused by the presence of nonspherical particles [*Agrawal and Traykovski*, 2001]. The particle number distribution was calculated from the volumetric distribution assuming spherical particles in the assemblage and normalizing by the width of each logarithmically spaced size bin.

During times of enhanced critical angle scattering, bubble size distributions were obtained from the LISST by removing the background particle size distribution from the total particle distribution. A power law approximation was fit to the bubble size distribution data, such that:

$$n(a)=N_0 a^{-\xi} \tag{2}$$

[*Buonassissi and Dierssen*, 2010]. The equivalent spherical particle radius, a, is a nondimensional ratio of the actual particle size to a_0, where a_0 equals 1 μm. The dimensionless ξ is the exponent, also referred to as the bubble size distribution slope. The concentration factor, N_o, is the bubble differential number concentration at a_0 (number of bubbles per cubic meter per micron radius increment). The model was fit using the least squares estimator of the log-transformed variables. Bubble concentrations below 1000 m^{-3} $\mu\mathrm{m}^{-1}$ radius

were considered statistically undersampled and were excluded from the slope calculations. The bubble size distributions have been presented with units of number m^{-3} μm^{-1} radius. The void fraction (F), the volumetric fraction of air in water, was determined following:

$$F = \frac{4\pi}{3V}\int a^3 n(a)da \tag{3}$$

where V is the volume sampled, a is radius, and $n(a)$ is the number density of the measured size distribution. Void fractions were calculated from the measured bubble size distributions.

2.2. Measurements of the Upper Ocean Dynamics

Neutral wind speeds at the reference height of 10 m (U_{10}), were measured using an air-sea flux package deployed on the jack-staff of the ship [*Edson et al.*, 2011]. The wave frequency spectrum from 0.03 to 1.2 Hz was determined by combining measurements from a Wave Monitoring System (WaMoS II), a laser altimeter (Riegl LD-90), and a Shipborne Wave Height Meter (Tsurumi Seiki Co., LTD) [*Cifuentes-Lorenzen et al.*, 2013]. Wavefield statistics, including the significant wave height of the dominant waves (H_s) and the phase speed at the spectral peak (c_p) were determined from the measured wave frequency spectrum. Variables describing the state of the wind-wavefield, including inverse wave age or wind forcing (U_{10}/c_p) were also derived from the measured wave number and frequency spectra. For open ocean conditions, high inverse wave age values (i.e., $U_{10}/c_p > 0.82$) are considered young or developing seas, while low values (i.e., $U_{10}/c_p < 0.82$) are considered old or decaying seas. The threshold, $U_{10}/c_p \sim 0.82$, is considered mature or fully developed. Measurements of whitecap coverage were determined using high-resolution digital images.

Bubble clouds were identified in measurements of acoustic backscatter (120 kHz) over 15 m of the water column. The Acoustic Doppler Current Profiler (ADCP) collected data at high sampling frequency (2 Hz) in 75 bins, each measuring 25 cm. The portion of the signal attributable to bubbles, referred to as the acoustic backscatter anomaly, was determined by the removal of the mean signal of backscatter known to be bubble free. The ADCP was deployed on a drifting, autonomous MAPCO$_2$ Buoy. Bubble measurements collected acoustically and optically were coincident in time, however they were not collocated. Here, open ocean conditions with an unlimited fetch and relatively constant wind direction supported the assumption of spatial homogeneity in the physical conditions within a mesoscale range.

Bubble penetration depths, obtained from measurements of acoustic backscatter anomaly, and the associated wind and wave conditions were compared to those reported by *Thorpe* [1992] for consistency. *Thorpe* [1992] presented the scaling of bubble plume penetration depth (d_0) to the dominant wavelength at the spectral peak (λ_p). *Thorpe* [1992] considered the values of d_0/λ in the context of the forcing using inverse wave age, where, for U_{10}/c_p of 0.6 to 2, d_0/λ ranges from 0.04 to 0.2. This approach was based on the spectral peak of the wavefield. For older seas ($U_{10}/c_p < 0.82$), breaking in the spectral peak is minimized and displaced toward higher frequencies, within shorter, steeper waves [*Terray et al.*, 1996; *Babanin et al.*, 2007; *Gemmrich et al.*, 2008; *Banner and Morison*, 2010]. Consequently, the characteristic wave scale was used in order to delineate the wind-wave region of the spectra. This scale was used in the dispersion relation for deep water waves to retrieve the mean characteristic wavelength, λ_w [*Cifuentes-Lorenzen*, 2013]. These values were compared to the d_0/λ of 0.04–0.2 (for $0.6 \leq U_{10}/c \leq 2$) reported by *Thorpe* [1992]. Ultimately, the wind and wave statistics used here could be used in future studies to estimate bubble penetration depths.

2.3. Extrapolation of the Bubble Size Distribution to a Shallower Depth

Bubble size distributions near the base of the bubble plumes ($\geq$5 m) were measured as a part of this study. Bubble number concentration, for each radius increment, decays exponentially with depth [*Thorpe*, 1982; *Woolf*, 1997] and the void fractions measured at 6–9 m are very small (generally $\leq 10^{-8}$). The bubble size distributions measured here were extrapolated to shallower depths to assess the potential contribution of the small bubbles ($a < 60$ μm) to the void fraction and gas transfer processes. The SO GasEx bubble size distributions were extrapolated to 4.1 m using the observations of *Terrill et al.* [2001]. The *Terrill et al.* [2001] measurements were collected under wind and wave conditions ($U_{10} = 15$ m s^{-1}; $H_s = 3.2$ m) comparable to this study at a location in the North Pacific near Point Conception, CA. The depth and radius-dependent size distribution $N(a, z)$ is defined as:

$$N(a,z)=n(a)g(z) \tag{4}$$

In equation (4), $n(a)$ is the radius-dependent power law distribution (equation (2)) and $g(z)$ is the exponential decay behavior of the bubble size distribution with depth defined by *Woolf* [1997] as:

$$g(z)=e^{-z/L} \tag{5}$$

Here, z and L are the depth and attenuation depth (in meters), respectively. The attenuation depth (L) is the decay rate of the bubble concentration with depth. The functional behavior of the bubble size distribution with depth is determined using:

$$N(a,z)=Ba^{-\xi}e^{-z/L} \tag{6}$$

where B is a coefficient of proportionality. Assuming a constant size distribution slope, ξ, a solution for B was determined from

$$N_i=B_i e^{-z_i/L} \tag{7}$$

where $i=1$ is the SO GasEx bubble size distribution and $i=2$ is the *Terrill et al.* [2001] bubble size distribution. The value for L was selected so that continuity between the *Terrill et al.* [2001] data and the SO GasEx extrapolated bubble size distribution was achieved. A length of approximately 1 m is typical [*Thorpe*, 1986; *Woolf and Thorpe*, 1991; *Woolf*, 1997]. The bubble size distributions measured here were not extrapolated above $1/2H_s$, where extrapolations are likely no longer valid [*Baldy*, 1988].

3. Results

Measurements were conducted from yearday 69 to 92, at stations north of South Georgia Island in a region characterized by moderate phytoplankton biomass and high wind conditions. The majority of stations were sampled on the eastern edge of a high chlorophyll (0.4–1 mg m^{-3}) patch at latitude 51°S, as shown in the satellite-derived average chlorophyll imagery for March 2008 (Figure 1). From yearday 75 to 77, stations were sampled 300 km further south at latitude 54°S in waters surrounding South Georgia Island. Wind speed throughout the experiment varied from <1 to 20 m s^{-1} [*Edson et al.*, 2011]. This study focuses on bubble measurements made during periods of high wind speeds ($U_{10} \approx 13$ m s^{-1}) recorded on yeardays 76, 80, and 84. Two stations measured during low wind conditions ($U_{10} \approx 3$–5 m s^{-1}) on yeardays 81 and 86 were used as control stations (Figure 2).

3.1. Optical Measurements of Bubbles

During the days with high wind speeds of approximately $U_{10} \approx 13$ m s^{-1} (yeardays 76, 80, and 84), bubbles were detected at 6–9 m in both optical and acoustical measurements. Measurements of the angular scattering of light, the VSF from 10° to 170°, confirm the temporary presence of bubbles with enhanced scattering at the critical angle, $\beta(80)$ (Figure 3). Figures 3a, 3c, and 3e show the change in the shape of 1 Hz averaged VSF measurements throughout the 30 min time series for the three stations experiencing high wind conditions. The normalized VSF data averaged to 1 Hz are also shown on a two-dimensional plot to emphasize the magnitude of the increase in critical angle scattering (Figures 3b, 3d, and 3f). To evaluate the relative angular shape of the VSF, each measured VSF was normalized to the mean of the time series at each angle. Hence, a value of 1 is expected for each angle when the VSF is similar to the mean VSF in the water column. For all three stations, enhancements of more than twofold to threefold in critical angle scattering occurred periodically throughout the 30 min deployment. Other changes in the VSF shape also occurred, including enhancements in backscattering (90°–170°), sometimes by more than a factor of 2, during bubble events (Figures 3b, 3d, and 3f). Mie modeled scattering suggests the small peak present in the VSF occurring near 130° is likely caused by the presence of particulate material with a relative refractive index of approximately 1.20, similar to calcite [*Zhang et al.*, 2002]. According to *Balch et al.* [2011], coccolithophores and coccoliths were present and contributed 1–23% of the total backscattering at these stations.

Critical angle enhancements in the VSF were not observed during the low wind conditions, as illustrated by Figure 4. The measurements of the VSF collected during high wind speed conditions on yearday 84

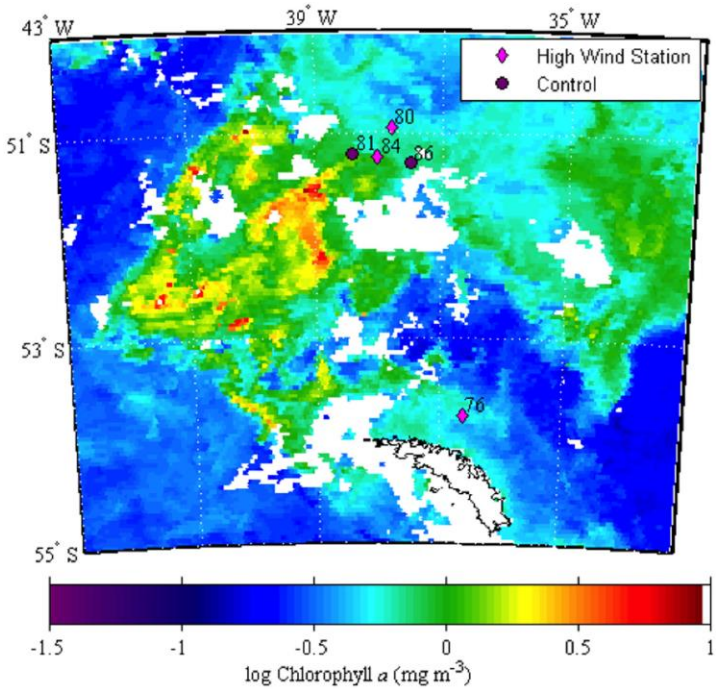

Figure 1. South Atlantic sampling region and station locations (labeled with the yearday) overlayed on the satellite-derived average chlorophyll *a* (mg m^{-3}) from the MODIS Aqua sensor (nominal 4 km resolution) for the month of March 2008. Three stations were sampled during high wind conditions (pink diamonds) and two were sampled during low wind conditions (purple circles). The white patches in the image indicate areas with no data due to cloud cover.

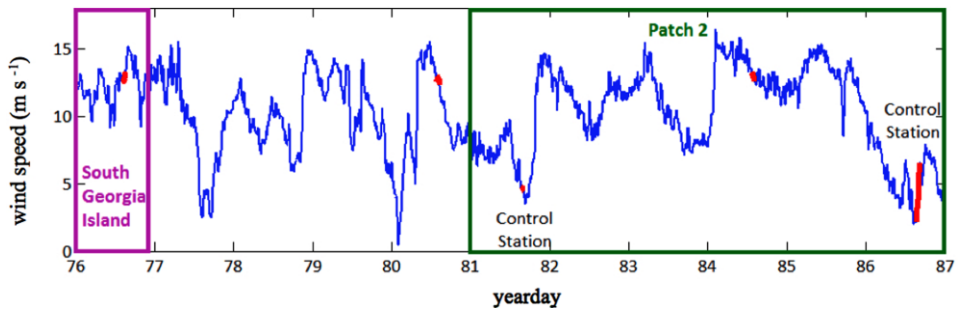

Figure 2. The wind speed record for SO GasEx, where the red highlighted regions identify the ≈30 min time periods during which the bubble data were collected. The mean wind speed (U_{10}) from each sampling period is reported in Table 1. The wind speed stayed relatively constant for all stations during sampling except on yearday 86, during which the wind speed increases by 3 m s^{-1} (red line). Day 80 and stations within Patch 2 (green box) correspond to 50.6°S, 38°W. Time before Patch 2 was spent approximately 300 km north of South Georgia Island (53.8°S, 36.6°W).

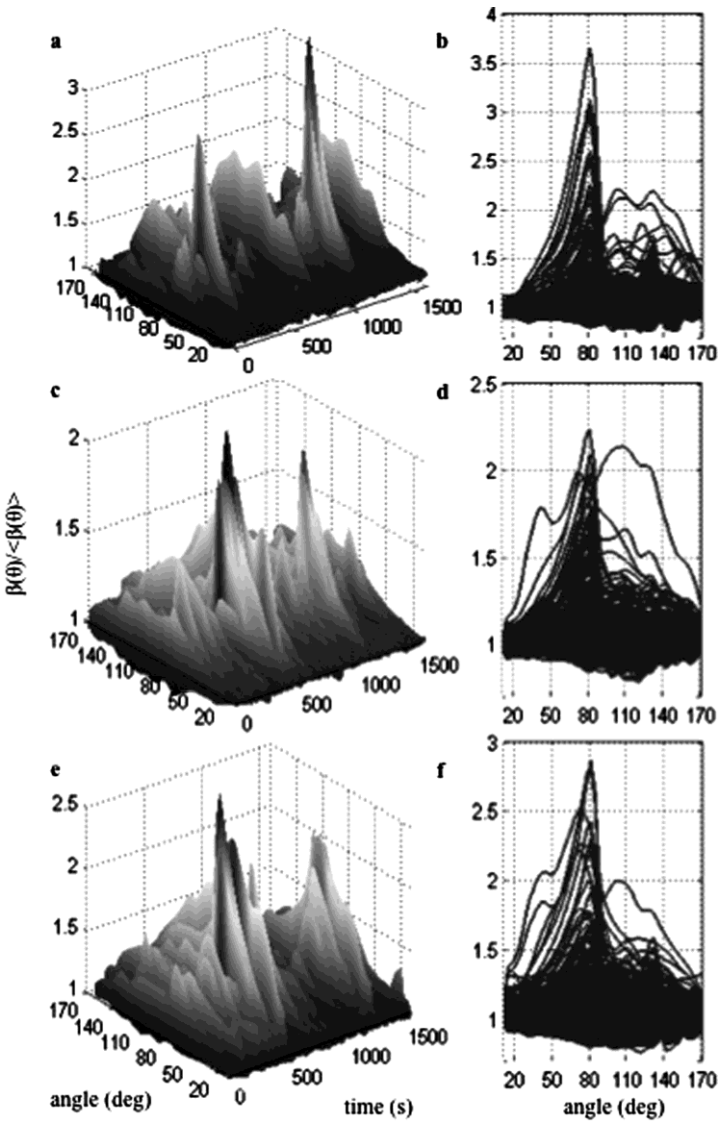

Figure 3. High-frequency (1 Hz) time series measurements of the mean normalized volume scattering function (VSF) for the three stations in the Southern Ocean measured during periods of high wind ($U_{10} \sim 13$ m s^{-1}) on yeardays (a) 76, (c) 80, and (e) 84 show temporary (75–180 s) enhancements in scattering at several angles. The most pronounced temporary enhancements occur at and around the critical angle scattering angle (~80°), due to bubble entrainment. The temporary enhancement in scattering in the backward direction (measured from 90° to 170°) is also apparent. (b, d, and f) The same data as in Figures 3a, 3c, and 3e, but replicated on a two-dimensional axis in order to more easily evaluate the magnitude of critical angle scattering at 80°. Enhancements of twofold to threefold occurred periodically throughout the 30 min deployments at all three stations (Figures 3b, 3d, and 3f).

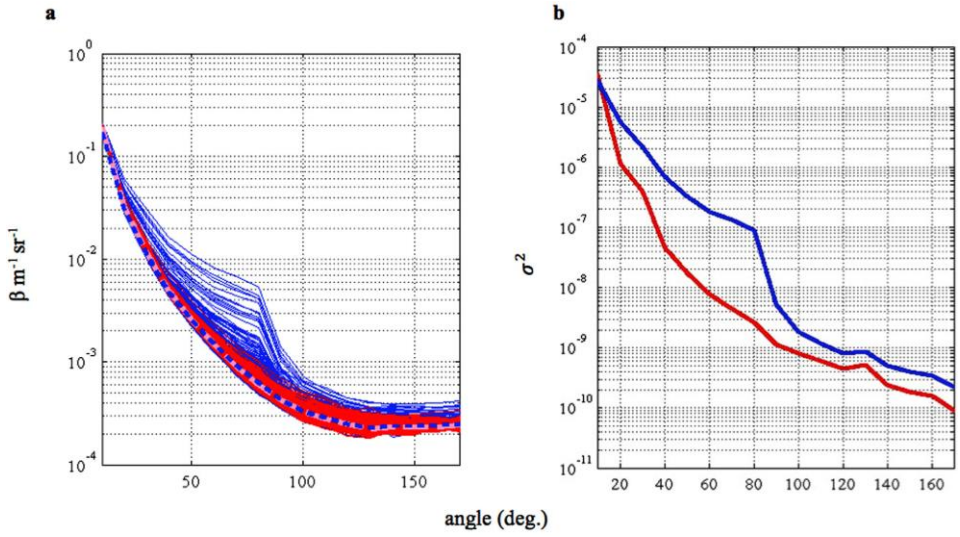

Figure 4. (a) MASCOT measured full VSF collected at a 1 Hz sampling frequency (each line represents the 1 Hz data) during periods of high (yearday 84; $U_{10} \approx 13$ m s^{-1}, blue lines; mean is blue dashed line) and low (yearday 86; $U_{10} \approx 3$ m s^{-1}, red lines; mean is pink dashed line) wind conditions for stations with similar particulate populations and background optical properties. (b) The variance of the high-frequency VSF time series collected during the periods of high (blue line) and low (red line) winds are plotted as a function of angle. Relative to the variance of the VSF time series collected during low wind conditions (red), the variance of the VSF collected during high wind conditions (blue) is enhanced at all angles. The variance of the VSF at the critical angle (80°) is approximately 2 orders of magnitude higher during periods of high wind relative to periods of low wind.

($U_{10} = 13$ m s^{-1}; Figure 4, blue lines) were compared to the VSF measurements collected during low wind conditions on yearday 86 ($U_{10} = 3$ m s^{-1}; Figure 4, red lines). Each line represents a VSF collected at a sampling frequency averaged to 1 Hz. These two stations had similar water column properties and amounts of total suspended material and chlorophyll *a*, but were sampled under markedly different wind and wave conditions. As expected, the VSF measured during low wind conditions showed no enhancement in scattering at the critical angle. Instead, a conventional oceanic VSF, with large amounts of light scattered in the forward direction (10°–90°) and less than 3% of the light scattered in the backward direction (90°–180°) was observed. Such VSFs, declining smoothly from 90° to 180°, are found throughout the world's oceans [*Sullivan and Twardowski*, 2009] and are used in radiative transfer modeling [*Fournier and Forand*, 1994; *Mobley et al.*, 2002]. In contrast, the VSF measured at stations experiencing high wind conditions showed an enhancement in scattering across all angles and at the critical angle in particular when bubbles were present (Figure 4, blue lines).

Moreover, the VSF at the critical angle $\beta(80)$ measured over the time series followed a different statistical distribution for the low and high wind stations. The low wind data are nearly lognormally distributed (Figure 5a, dotted line) and centered at the mean value of 5.5. In contrast, $\beta(80)$ data collected during high wind conditions were not normally distributed, but closely followed a Generalized Extreme Value (GEV) type II (or Fréchet) distribution (Figure 5a). For these stations, the central tendency is similar, but the tail shape parameter k, were heavily positively skewed ($0.24 < k < 0.32$) due to the intermittent presence of bubbles (Figure 5a, dashed lines). The variance of critical angle scattering collected during yeardays 76, 80, and 84 was also much higher ($3.7 \times 10^{-9} \leq \sigma^2 \leq 1.2 \times 10^{-8}$) relative to the control ($\sigma^2 = 7.2 \times 10^{-10}$). For yeardays 76, 80, and 84, 16% 12%, and 21% of the critical angle scattering measurements exceeded the range of the control (Figure 5b, dashed lines).

Various measurements indicate the presence of sufficient dissolved organic material to coat bubbles. Absorption by colored dissolved organic matter at 412 nm ranged from 0.03 to 0.1 m^{-1}. Globally

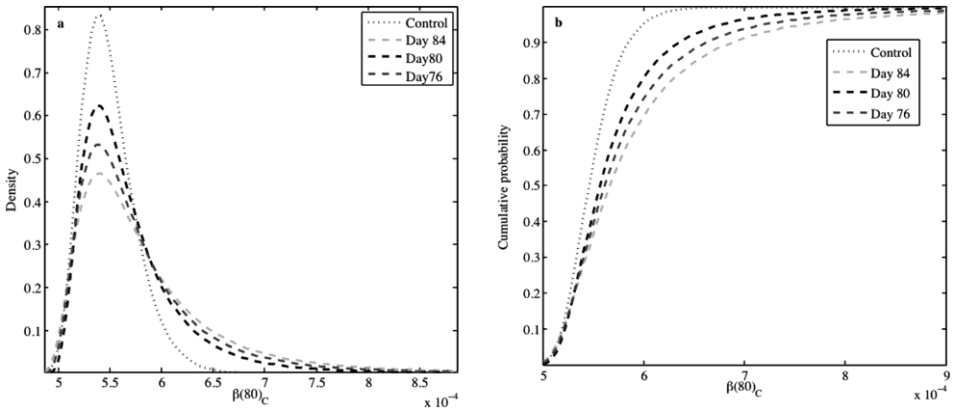

Figure 5. (a) The probability density distribution of critical angle scattering normalized by the cumulative sum of $\beta(80)$ for each station ($\beta(80)_C$), for stations experiencing high wind conditions, yeardays 84 (light gray, dashed line), 80 (black, dashed line), and 76 (dark gray, dashed line) compared to the mean of the control stations experiencing low wind conditions (control, dotted line). (b) The cumulative probability distribution of $\beta(80)$ for stations experiencing high wind conditions, yeardays 76, 80, and 84 (dashed lines), showed 16%,12%, and 21% of critical angle scattering measurements exceeded the range of the control (dotted lines), respectively. The variance of critical angle scattering collected during yeardays 76, 80, and 84 was high ($3.7 \times 10^{-9} \leq \sigma^2 \leq 1.2 \times 10^{-8}$) relative to the control ($\sigma^2 = 7.2 \times 10^{-10}$).

representative values of colored dissolved organic matter for comparison, including coastal values, fall within the range of 0.003–10 m^{-1} [*Twardowski et al*., 2004]. Similarly, discrete measurements of total and dissolved organic carbon during SO GasEx were within the range of 56–72 μM and 50–76 μM, respectively (P. Vlahos, personal communication, 2009). These concentrations are consistent with those used in the analysis of *Detwiler and Blanchard* [1978], for which bubbles became coated within 5 s of entrainment.

3.2. Measurements of the Bubble Size Distribution

The LISST measured bubble size distributions ranged from 0.5 to 125 μm radius; however, no bubbles with greater than 60 μm were detected at the depth of measurement (Figure 6). Bubble injections occurred on all days during which high winds were measured and the events typically lasted from tens to over a hundred seconds in duration. The shaded regions in Figure 6 represent the range in the bubble size distribution records averaged to a 1 Hz sampling frequency. The lines represent the mean and standard deviation of the bubble size distribution for each bubble event. On yearday 76, two bubble events occurred 13.5 min apart and lasted 150 and 180 s in duration. Similarly, on yearday 80 two distinct bubble events lasting 160–180 s in duration were measured. The most dense and intense bubble events were measured on yearday 84. The first event produced a 10-fold increase in critical angle scattering lasting 75 s in duration. A second isolated event occurred 5 min later, lasting 140 s in duration. Finally, the time series ended with a seemingly long period (512 s), during which the VSF fluctuated from high to low critical angle scattering. It is possible that these bubbles are part of a large plume that is being advected past the instrument package or that the bubbles are being recirculated. Alternatively, bubbles measured during this event could be part of a larger bubble plume than the other plumes measured. The background particulate population within the size range measured by the LISST did not change significantly over the course of the 30 min time series on any of the stations.

A power law was fit to each 1 Hz bubble size distribution spectrum over the size range sampled for which bubble populations exceed 10^3 m^{-3} μm^{-1} between 2 and 40 μm (Table 2). Though the use of a power law fit is simplistic and offers only a first-order approximation [*Buonassissi and Dierssen*, 2010], it is commonly used to describe bubble size distributions [i.e., *Medwin*, 1977; *Vagle and Farmer*, 1992; *Woolf*, 1997]. Mean slopes, ξ, for the bubble size distributions collected on yeardays 76, 80, and 84 were 4.6, 4.1, and 3.6, respectively. A range in measured slopes, generally 2.9–5.1, was measured throughout the lifetime of the bubble events. A number of fine-scale features are apparent in the measured bubble size distributions and could be associated with uncertainties in the measurements. For example, a change in the slope occurs between

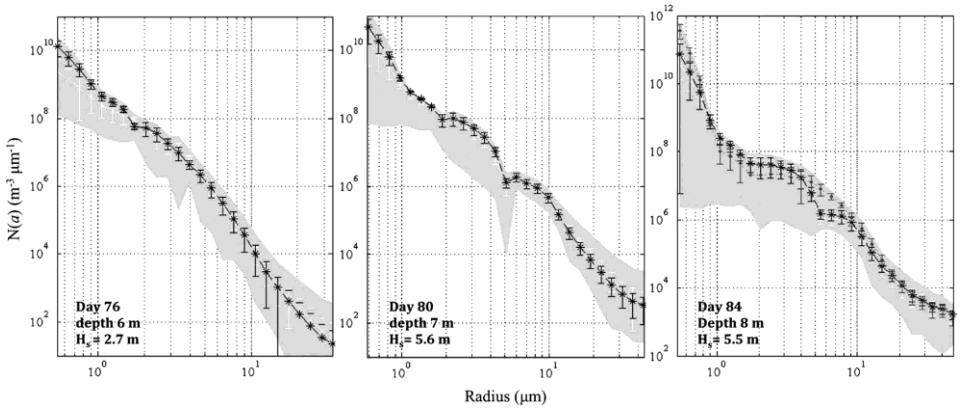

Figure 6. Bubble size distributions measured with the LISST instrument during high wind conditions (≈13 m s^{-1}) on yeardays (a) 76, (b) 80, and (c) 84. The shaded region represents the range in the BSD records collected at 1 Hz sampling frequency. The lines represent the mean and standard deviation of the BSD for each bubble event. (a) On yearday 76, two bubble events occurred 13.5 min apart and lasted 150 (black asterisk) and 180 s (white x) in duration. (b) On yearday 80, two distinct bubble events lasting 160 (black asterisk) to 180 s (white x) in duration were measured. (c) Three events occurred on yearday 84. The first two lasted 75 s (black asterisk) and 140 s (white x) in duration. The time series ended with a seemingly long (512 s) event, during which the VSF fluctuated from high to low critical angle scattering. The range in bubble size distribution slope, depth of measurement, and oceanographic conditions are reported in Table 2 for each station.

1 and 2 μm radius, such that small bubbles followed a shallower slope and large bubbles, a relatively steeper slope. Very steep slopes for the smallest size classes ($0.5 \leq a \leq 1$ μm) could be an artifact of the measurement where "rising tails" in the distribution can be produced by stray light, irregularly shaped, or submicron particles [*Agrawal and Pottsmith*, 2000; *Buonassissi and Dierssen*, 2010; *Andrews et al.*, 2011]. The LISST inversion method is still being refined, therefore the uncertainty associated with the fine-scale dips and peaks in the size distribution and the accuracy of such features are being considered in future research. However, it is also possible that the discontinuities in the power law slope of the bubble size distribution could be delineating lognormally distributed subpopulations of bubbles with different temporal and spatial dynamics [see *Zhang et al.*, 2011; *Czerski et al.*, 2011; *Twardowski et al.*, 2012].

A comparison between the bubble size distributions presented here and previously published size distributions [i.e., *Johnson and Cooke*, 1979; *Farmer and Vagle*, 1989; *Breitz and Medwin*, 1989; *Phelps and Leighton*, 1998; *Pascal et al.*, 2010] shows a general consistency in the size distribution shape, except for the absence of the peak that appears in many published bubble size distributions (Table 3; Figure 7 adapted from *Brooks et al.* [2009]). The average slopes of the size distributions measured in the Southern Ocean were slightly steeper (mean $\xi = 4.6$, 4.1, and 3.61) than the majority of the published slopes ($\xi \sim 3$–4). Also, substantial differences in the magnitude of bubble concentration were observed between bubbles measured here and those presented in previously published research within the radius range of 10–25 μm (the size classes included in all of the plotted bubble size distributions).

The small bubbles sizes measured at 6–9 m depth during SO GasEx yielded void fractions $O(10^{-8}-10^{-7})$, whereas bubble populations near the surface typically correspond to void fractions $O(10^{-4})$ (Table 2). The volume contribution of air by the smallest size classes ($a < 10$ μm) was not negligible. As small bubbles were incrementally included in the integration from large to small sizes, the total void fraction continued to increase, though at a lower rate relative to that contributed by larger ($a > 10$ μm) bubble sizes (Figure 8). Exclusion of the smallest bubbles in the calculation of the total void fraction would ultimately result in an order of magnitude underestimation.

3.3. The Evolution of Bubble Events

The evolution of the bubble population during events was investigated in the 1 Hz data collected using the LISST. As a result of the wave conditions, the optical instruments were not held at a fixed depth for the

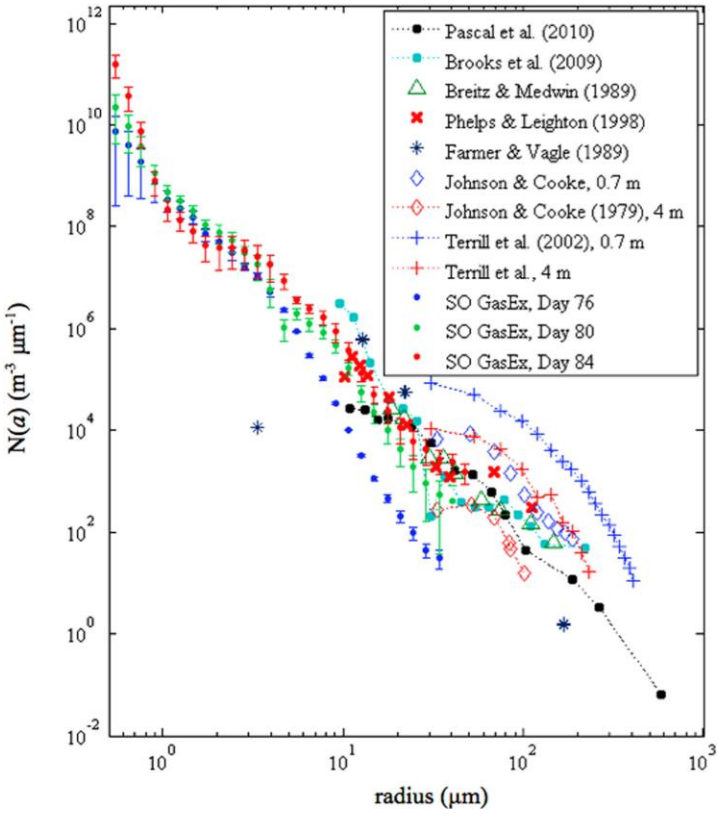

Figure 7. Adapted from *Brooks et al.* [2009]. A comparison between mean and standard deviation of the bubble size distributions from SO GasEx collected on yeardays 76 (blue), 80 (green), and 84(red) to those by *Breitz and Medwin* [1989] (triangles), *Johnson and Cooke* [1979] (diamonds), *Phelps and Leighton* [1998] (x's), and *Farmer and Vagle* [1989] (asterisks). Also included are the BSDs measured during DOGEE [*Pascal et al.*, 2011] (black dots) and the UK-SOLAS SEASAW (blue dots) projects. See Table 3 for the oceanographic conditions, measurement techniques, and locations associated with the previously published BSDs shown.

duration of the time series. In order to account for this, the data were bin averaged based on the peak frequency of the pressure measurement collected by the LISST. For yeardays 76, 80, and 84, the peak frequency of package motion followed the period of the swell and occurred at 0.172, 0.106, and 0.094 Hz, corresponding to periods of 5.8, 9.4, and 10.7 s, respectively. Both the bubble number concentration and the size distribution changed throughout the evolution of the bubble event until the bubble cloud was no longer detectable, at which time scattering at the critical angle and the concentration of particles returned to background levels. However, no statistically significant trend in the composition of the bubble population (i.e., steepening or flattening of the bubble size distribution) was found throughout the evolution of the bubble events (Figure 9).

3.4. Bubble Measurements in the Context of Wind and Wave Dynamics

During moderate to high wind conditions (up to 19 m s^{-1}), large-scale wave breaking and bubble entrainment was observed during the course of the experiment. Figure 10 shows the time series record of wind speed (white line) and acoustic backscatter anomaly (surface coloration) with depth, indicating a relatively

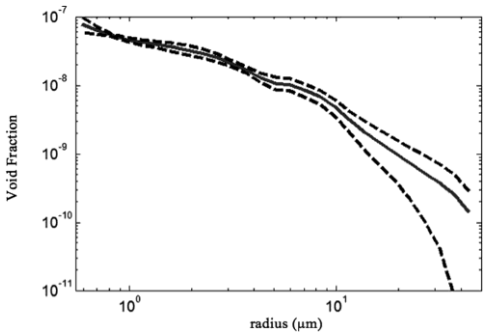

Figure 8. An example of the cumulative void fraction of air in water (dimensionless) calculated from large to small size classes for the first bubble event occurring on yearday 80, where the solid black line is the mean and the dashed gray lines denote one standard deviation above and below the mean.

stable subsurface bubble layer. An acoustic backscatter anomaly of 0 indicated water devoid of bubbles and a high value indicated dense bubble plumes.

Differences exist between the bubble size distributions measured at each station due, in part, to the prevailing physical forcing conditions (Table 1). No statistical relationships can be investigated between the bubble populations and environmental conditions measured here due to the limited number of stations. However, the physical conditions associated with the measured bubble populations were reported to aid in both the interpretation of the observed bubble events and in identifying the locations of measurements within the bubble plumes.

The prevailing physical forcing conditions during yeardays 80 and 84 were similar. The mean significant wave height and inverse wave age measured on yeardays 80 and 84 were 3.8 and 3.4 m and 0.73 and 0.64 (Table 1). Large breaking events under strong wind forcing led to the vertical extension of bubble plumes deep into the surface water column on yearday 84. Measurements of the acoustic backscatter anomaly identified bubble penetration depths of up to 15 m, with a high intensity range occurring between the surface and 6 m (Figures 11a and 11c). The mean penetration depth normalized by the characteristic wavelength (λ_w) for yearday 84 was 1.12 (Table 2). A bubble plume penetration depth ranging from 7.7 to 11.6 m was estimated for yearday 80, assuming the normalized penetration depth scaling from yeardays 76 and 84. The longer characteristic wavelengths measured on these yeardays (λ_w of 9.7 and 10.6 m) resulted in more intense plumes with a slowly decaying mean bubble radius with depth relative to yearday 76 (Table 1). During yeardays 80 and 84, bubbles as large as 50 μm in radius were measured.

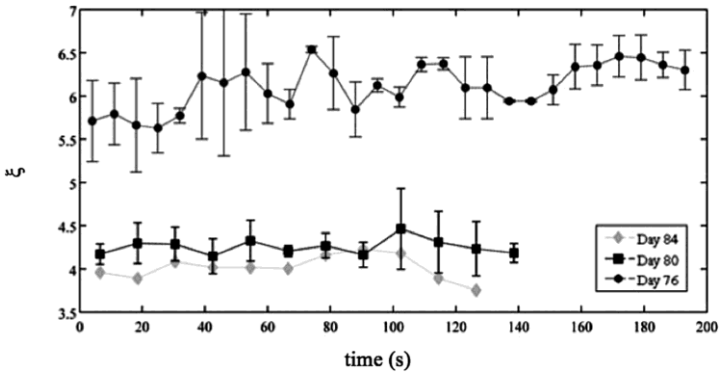

Figure 9. The bubble plume evolution was traced through time using the power law slope fit to the low-pass filtered BSDs from 5 to 30 μm (ξ'). The time-dependent ξ' for all events at each station were averaged to analyze trends in the bubble size distribution throughout bubble events. The error bars are standard deviations. The average of the two bubble events occurring on yearday 76 showed a slight increasing trend over time (gray circles), whereas bubble events on yeardays 80 (2 events, black squares) and 84 (1 event, gray diamonds) showed no significant trend over time.

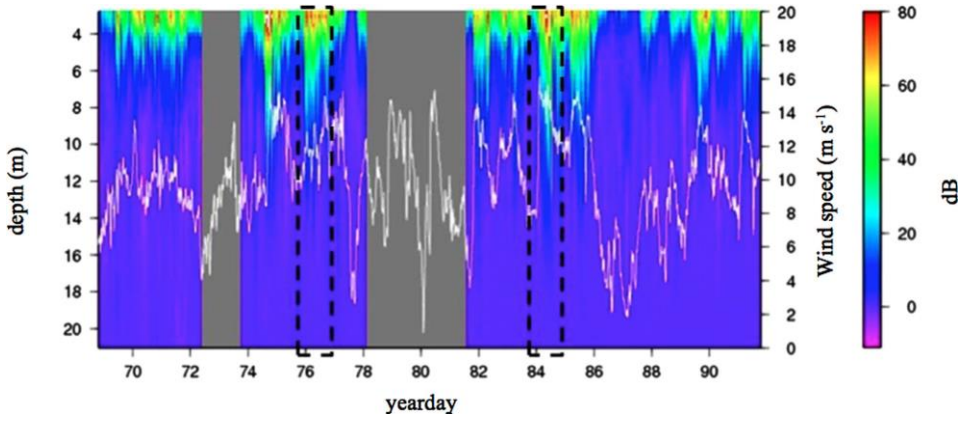

Figure 10. Acoustic backscatter anomaly (dB) and wind speed record (white line) for the SO GasEx experiment. The acoustic backscatter anomaly is a measure of the density of bubbles within the water column, where a high acoustic backscatter anomaly corresponds to dense bubbles. An acoustic backscatter anomaly of 0 means no bubbles are detected. The periods of high winds, yeardays 76 and 84, are identified with black dashed boxes. The gray box indicates the time period during which no acoustic data were collected (i.e., yearday 80).

Smaller significant wave height (H_s = 2.8 m) and shorter characteristic wavelength (λ_w = 5.8 m) measurements were observed on yearday 76. This resulted in lower intensity bubble clouds at depth and maximum bubble sizes that did not exceed 30 μm in radius. The most intense breaking events observed on yearday 76 produced penetration depths exceeding 10 m. However, bubble plumes generally did not extend beyond 5 m (Figures 11a and 11b). The mean normalized penetration depth (d/λ_w) measured during yearday 76 was 0.90 (Table 2).

3.5. Extrapolation of the Bubble Size Distribution to Shallower Depths

The discrepancies in concentration and slope between the bubble size distributions measured here and previously published bubble size distributions are likely due to the depth of measurement. Between 6 and 9 m, few bubbles larger than 50 μm radius were measured. Measurements of the acoustic backscatter anomaly (dB) suggest that the bubble size distributions collected in the Southern Ocean are at the base of plumes (Figure 10), consistent with the result of fewer bubbles and steeper size distribution slopes. An extrapolation of the SO GasEx bubble size distribution was completed to estimate the contribution of small bubbles to the void fraction at a shallower depth. The mean bubble size distribution measured at 6–9 m in the Southern Ocean was extrapolated to a depth of 4.1 m using a power law fit to the SO GasEx and *Terrill et al.* [2001] bubble size distributions (equation (2)) and equations (5–8). An attenuation depth (L) of 1.2 m was assumed in order to guarantee continuity between the *Terrill et al.* [2001] and SO GasEx bubble size distributions at 4 m. This attenuation depth is consistent with the wind speed relationships presented by *Woolf* [1997] and *Thorpe* [1992] and with measurements presented by *Vagle et al.* [2010]. The power law fit to the SO GasEx and *Terrill et al.* [2001] data yielded N values of 3.39×10^9 and 2.44×10^9 and ξ values of 4.1 and

Table 1. A Summary of the Physical Conditions Measured at Five Southern Ocean Stations Including the Mean Neutral Wind Speed (at 10 m) for the Sampling Period (U_{10}, m s^{-1}), Mean Sea Surface Temperature at 5 m (T_w, °C), Mean Air Temperature at 10 m (T_{air}, °C), Mean Measured or Estimated Fractional Whitecap Coverage (WC), Mean Significant Wave Height (H_s, m), Mean Peak Phase Speed (c_p, m s^{-1}), Range of the Inverse Wave Age (U_{10}/c_p), and Mean Characteristic Wavelength (λ_w, m) Based on the Characteristic Phase Speed

Day of Year	U_{10} (m s^{-1})	T_w (°C)	T_{air} (°C)	WC	H_s (m)	c_p (m s^{-1})	U_{10}/c_p (range)	λ_w (m)
76	12.8	3.3	4.6	0.006	2.8	14.2	0.55–1.13	5.8
80	12.7	5.7	7.7	0.002[a]	3.8	19.2	0.52–0.80	8.5
84	13.0	4.9	2.2	0.030	3.4	16.9	0.46–0.85	7.0
86 Control	3.1	4.8	5.1	0.001	2.7	17.1	0.15–0.72	3.6
81 Control	4.6	5.1	6.0	0.001[a]	3.4	14.1	0.10–0.80	3.7

[a]Estimated based on wind speed following *Monahan and Spillane* [1984].

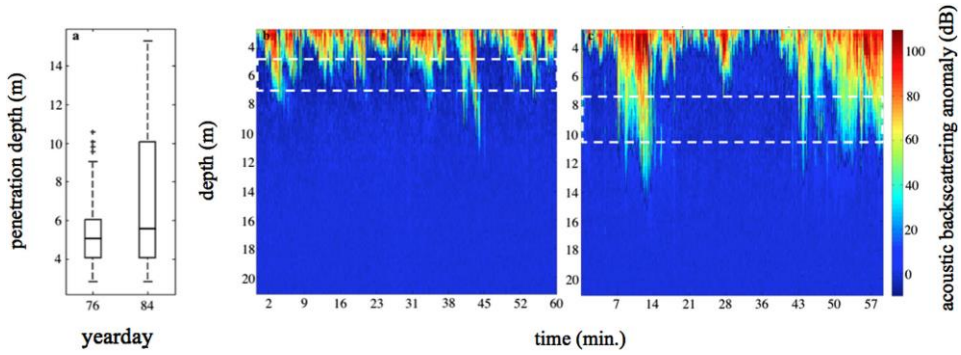

Figure 11. (a) Bubble plume penetration depths estimated using time series measurements of acoustic backscatter anomaly (dB) collected on yeardays, (b) 76, and (c) 84. In Figure 11a, the box denotes the lower quartile, median, and upper quartile penetration depth values. The whiskers show the range of the data and the pluses denote outliers. High temporal resolution plots of the acoustic backscatter anomaly over the 1 h sampling period show intense breaking on (a) yeardays 76 and (b) 84 days produced bubble plumes that extended to 10 and 15 m, respectively. No acoustic data were collected on yearday 80.

3.3, respectively. The depth-dependent bubble size distribution $n(a, z)$ in the range of 8–4 m was given in a stepwise manner following:

$$n(a,z)=\begin{cases} B_1 a^{-\xi_1} e^{-z/L}, & 2 \le a \le 30\ \mu m \\ B_2 a^{-\xi_2} e^{-z/L}, & 30 < a \le 120\ \mu m \end{cases} \quad (8)$$

where B_1 and B_2 are coefficients of proportionality determined using equation (7) (Figure 12). The full ($2 \le a \le 120$ μm), *Terrill et al.* [2001] derived SO GasEx bubble size distribution at 4 m produced a total void fraction of 9.8×10^{-7}. Bubbles $30 < a \le 120$ μm in size contributed 6.3×10^{-7} and the smallest bubbles, $2 \le a \le 30$ μm, contributed 3.5×10^{-7} to the total void fraction.

3.6. The Contribution of Bubbles to Dissolved Oxygen

Supersaturations of up to 5% were measured during high wind conditions in the Southern Ocean. Using the model of *Woolf and Thorpe* [1991] and *Moore et al.* [2011] estimated the bubble-mediated contribution to O_2 supersaturation to be 1%–2% at 5 m during yeardays 76 and 84, respectively. However, the model applied is based on the bubble size distribution measurements of *Johnson and Cooke* [1979] and neglects bubbles <30 μm in size (Figure 13a). *Woolf and Thorpe* [1991] refer to the exclusion of these bubbles as a serious omission because the incremental inclusion of smaller bubble sizes substantially increases the gas injection rate and the projected equilibrium supersaturation (Figure 13b, black dots). The supersaturating effect of bubbles during high wind conditions (i.e., 13 m s^{-1}) could exceed the estimated 1–2% and account for a larger portion of the measured supersaturation (perhaps up to 4–5%) by extending the SO GasEx bubble size distributions measured here to 1 μm (Figure 13b, gray dots).

Table 2. Bubble Size Distribution (BSD) Statistics Collected at Depth (z, m) at Three Stations Experiencing High Wind Conditions (U_{10}, m s^{-1}), Including the Mean Bubble Penetration Depth (d_0, m), the Normalized Penetration Depths (Dimensionless), Which Describe the Relationship Between Bubble Plume Penetration Depth and the Characteristic Wavelength (d/λ_w), the Mean and Range of Power Law Slopes of the BSD Extending From 2 to 40 μm Radius (ξ), the Logarithmic Concentration Factor (N_o, m^{-3} μm^{-1}), and the Mean Void Fraction (F) of all Events for Each Station

Day of Year	z (m)	U_{10} (m s^{-1})	d_0 (m)	d/λ_w	ξ ($2 < a \le 40$) Mean (range)	BSD N_0 (m^{-3} μm^{-1})	F
76	6.0 (±1)	12.8	5.2	0.90	4.6 (4.2–5.1)	10.7	10^{-8}
80	6.8 (±1.5)	12.7	7.7–8.4[a]	Unknown	4.1 (3.9–4.3)	10.6	10^{-7}
84	8.6 (±2)	13.0	6.9	0.99	3.6 (2.9–3.8)	10.4	10^{-7}

[a]Estimated range in penetration depths based on the normalized penetration depth scaling from days 76 and 84.

Table 3. Summary of Conditions Associated With Previously Published Bubble Size Distributions Shown in Figure 14 Including the Depth of Measurement, the Mean Wind Speed ($\overline{U}_{10}$: m s^{-1}), Water Temperature (T_w, °C), a Description of the Wave Field, the Instrument Used in Measuring the BSD, and the Location at Which the Measurements Were Collected

Reference	Depth of Measurement (m)	U_{10} (m s^{-1})	T_w (°C)	Wavefield	Measurement Approach, Location
Brooks et al. [2009]	Unknown	≈14	9	$H_s \approx 2.7$	Bubble Camera
Johnson and Cooke [1979]	0.7	11–13	2	$H_s \approx 2.0$	Photographic, St. Margaret's Bay, Nova Scotia
Breitz and Medwin [1989]	0.25	12–15		3 m swell	Acoustic, Monterey Bay
Farmer and Vagle [1989]	0.10	12–14	21.5	5 s period	Acoustic, Atlantic (28°N, 70°W)
Phelps and Leighton [1998]	0.50	10–12		No data	Acoustic, South Hampton Coast ($z = 17$–22 m)
Pascal et al. [2010]	2–3	14	17	$H_s = 2.7$	Acoustic, Fiber optic, North Atlantic

4. Discussion

Concurrent optical measurements of the particle size distribution and the volume scattering of light at the critical angle were used to identify naturally occurring, transient O(10^1–10^2) s, deeply penetrating bubble populations during large-scale wave breaking in the Southern Ocean. This is a very limited data set, containing only three stations for which bubble measurements were collected. No statistical analyses can be performed nor any broad conclusions made about the behavior of the bubbles measured here and their

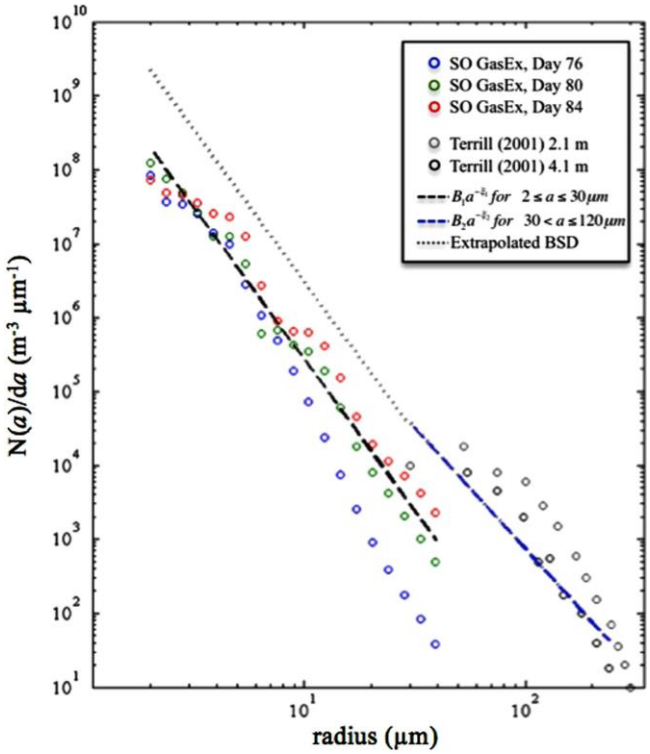

Figure 12. A single mean BSD (black dashed line), calculated from the mean BSDs measured on yeardays 76 (blue circles), 80 (green circles), and 84 (red circles) at 6–9 m in the Southern Ocean, was extrapolated to a depth of 4.1 m using a power law fit to the SO GasEx and *Terrill et al.* [2001] BSDs (gray circles) following equation (8) for $2 \le a \le 30$ (gray dotted line) and $30 < a \le 120$ (blue dashed line). The power law fit to the SO GasEx and *Terrill et al.* [2001] data yielded N values of 3.39×10^9 and 2.44×10^9 and ξ values of 4.1 and 3.3, respectively. Bubbles $30 < a \le 120$ μm in size contributed 6.3×10^{-7} (64%) of the total void fraction of 9.8×10^{-7}, while the smallest bubbles, $2 \le a \le 30$ μm, contributed 3.5×10^{-7} (36%).

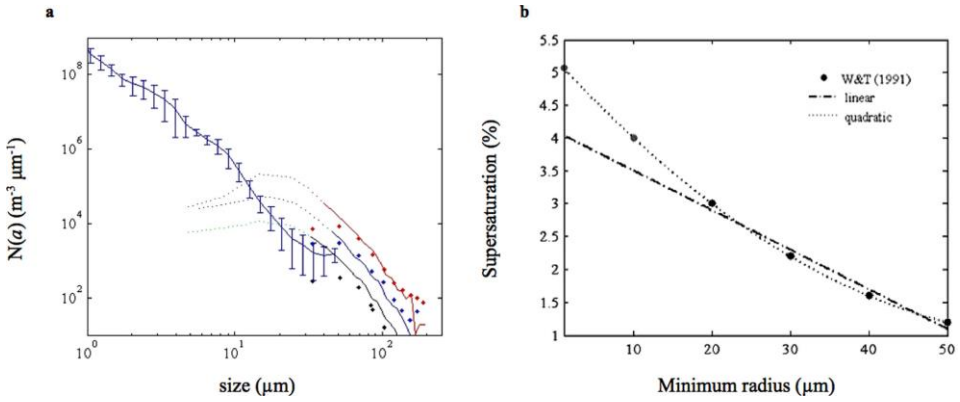

Figure 13. (a) *Moore et al.* [2011] estimated the bubble-mediated contribution to O_2 supersaturation to be 1%– 2% at 5 m during yeardays 76 and 84, respectively, using (a) the data of *Johnson and Cooke* [1979] at 0.7 m (red line), 1.8 m (blue line), and 4 m (black line) and (b) the model of *Woolf and Thorpe* [1991].For a 13 m s^{-1} wind speed, the model suggests that a maximum of 3% supersaturation will result using Johnson and Cooke's data, for which the minimum bubble radius is 20 µm (Figure 13b, black dots). Using the average bubble size distribution (BSD) measured during SO GasEx with a minimum radius of 1 µm (Figure 13a, blue line, with standard deviation), the predicted oxygen equilibrium supersaturation at 14 m s^{-1} wind speeds (gray dots) assuming a quadratic relationship (dotted line) and a linear relationship (dot-dashed line) suggest maximum suspersaturations of up to 4 and 5%, respectively.

relationship the wind and wavefield dynamics. However, these are some of the first measurements of such small bubbles at depth, particularly under natural wave breaking conditions, and their evolution, persistence, and potential contribution to air-sea flux of lower solubility gases is considered further below.

4.1. Measurements of Small Bubbles at Depth

The bubble size distributions presented here were collected during 13 m s^{-1} mean wind speeds. Though the mean wind speed was consistent throughout the three stations, the prevailing sea state produced bubble clouds with different intensities and therefore, different size distributions. The state of the wavefield is a function of the energy flux from the wind (i.e., wind history and fetch) [*Thorpe*, 1992; *Sullivan and McWilliams*, 2010]. The wind history (along an increasing trend) likely contributed to the nature of the bubble size distributions measured on yearday 76. During day 76, younger seas and shallower bubble penetration depths were measured. As a result, steeper bubble size distribution slopes and fewer large bubbles were measured (see Figure 7). Large breaking events under strong forcing led to the vertical extension of bubble plumes deep into the surface water column on yeardays 80 and 84. Bubble penetration depths of up to 15 m, more than $3H_s$, were measured. During days 80 and 84, bubble measurements were collected within a decreasing wind trend (from 15 m s^{-1}). Larger bubble sizes and shallower bubble size distribution slopes were measured at these stations.

The *Thorpe* [1992] parameterization relating bubble plume penetration depth to the wavelength of the dominant waves produced normalized penetration depths of 0.1–0.2 under forcing conditions comparable to those in the presented here. The Thorpe approach, modified here using the characteristic wavelength, produced a near 1:1 relationship between the mean bubble plume penetration depth and mean characteristic wavelength. For SO GasEx, the penetration depth scaling according to significant wave height follows $H_s < d_o < 4H_s$.

The average Southern Ocean bubble size distributions show a general consistency with previously measured bubble size distributions. The order of magnitude difference in concentration between those measured here and the previously published bubble distributions is likely due to the depth of measurement; here, bubble size distributions were collected near the base of the bubble plumes. This is particularly true for yearday 76, during which steep slopes were measured at the base of the bubble plumes. On yeardays 84 and 80, bubble measurements were collected approximately three quarters of the way down the plume,

due to the deep vertical extension of bubbles. As a result, bubble size distributions measured on those days produced slopes comparable to previously published values.

The Southern Ocean bubble size distributions measured as a part of this study decreased exponentially from small to large sizes and were not peaked. Many previously published bubble size distributions measurements show a hypothetical peak in the distribution between 20 and 60 μm that tails off at smaller sizes [i.e., *Johnson and Cooke*, 1979; *Kolovayev*, 1976; *Walsh and Mulhearn*, 1987] (see Figure 8). The presence of the peak has been justified theoretically due to the pressure effects on bubbles at depth. The peak at intermediate sizes, and the narrowing of the bubble size distribution with depth, has been attributed to the smallest bubbles having undergone dissolution and large, buoyant bubbles rising out of the water column. However, the presence of a peak could be the result of limitations in the acoustic and photographic methods used [*Kingsbury and Marston*, 1981; *Vagle and Farmer*, 1992]. A new optical approach applied by *Zhang et al*. [2002] for retrieving the bubble size distribution using inversion techniques supported the existence of submicron bubbles with concentrations on the order of 10^{12} m^{-3}. These results provide additional support for the presence of bubbles down to submicron sizes with concentrations following a power law distribution.

Detection of small bubbles at 6–9 m supports the existence of a mechanism that prolongs the process of bubble dissolution, aiding in their temporary persistence. The stabilization of microbubbles by the adsorption of organic substances could be at play here. Organic coatings can make bubbles mechanically stable by hindering compression and altering buoyancy, thus increasing residence times. Once coated, microbubbles have a size-dependent resistance to pressure, where resistance is inversely proportional to size [*Johnson and Cooke*, 1980]. Laboratory experiments by *Thorpe et al*. [1992] tested the effects of incrementally increasing particulate concentrations on bubble size distributions at 4 m depth. The result was a steep bubble size distribution (no peak) covering a range in radii from 0 to 10 μm, as was observed in the SO GasEx bubble size distributions. In the absence of candidate coating material, *Thorpe et al*. [1992] observed a peak in the bubble size distribution at $a \approx 40$ μm, where small bubbles fell off steeply due to rapid dissolution. The *Thorpe et al*. [1992] results in combination with the particulate and total and dissolved organic carbon measured during SO GasEx support the hypothesis that the bubbles measured here are coated [*Detwiler and Blanchard*, 1978; *Thorpe et al*., 1992].

4.2. Evolution and Persistence of Small Bubbles

Deep-going bubble plumes evolve mainly under the influence of advection, turbulent diffusion, dissolution, and buoyancy forces [*Thorpe*, 1982; *Baldy*, 1988]. Bubbles in the size regime measured here (<60 um) are thought to completely disappear by dissolution [*Merlivat and Memery*, 1983; *Keeling*, 1993]. Small bubbles measured during SO GasEx were measured over time periods on the order of 10–100 s. The potential fate of the bubbles measured here was investigated by analyzing changes in the size distribution over time. We expected that the SO GasEx bubble size distributions would maintain a flatter size distribution slope throughout bubble events, since the principle loss mechanism was likely dissolution. No statistically significant trends were observed in the bubble size distribution slope over time for the older seas encountered on yeardays 80 and 84. We hypothesize that the small bubbles were terminated by dissolution at a rate independent of size, which would result in a constant slope [*Garrett et al*., 2000]. For the younger seas encountered on yearday 76 and measurements made closer to the base of the bubble plume, a slight steepening in slope was observed over time, indicating the potential for preferential loss of larger bubbles. This result could indicate buoyancy as the dominant bubble removal process [*Garrett et al*., 2000].

4.3. Small Bubble Contribution to the Void Fraction

If dissolution is the dominant mechanism by which the deeply penetrating SO GasEx bubbles are terminated, then they could be relevant to the transfer and supersaturation of the surface ocean with low-solubility gases in near-equilibrium conditions [*Woolf and Thorpe*, 1991; *Garrett et al*., 2000]. Void fractions for the bubble densities measured at 6–9 m depth ranged from 10^{-7} to 10^{-9} and were composed entirely of bubbles from 0.5 to 60 μm in size. The volume contribution of air by the smallest size classes ($a < 10$ μm), previously unmeasured, was not negligible. As small bubbles are incrementally included in the integration from large to small sizes, the total void fraction continues to increase, though at a lower rate relative to that contributed by larger ($a > 10$ μm) bubble sizes (Figure 9). Exclusion of the smallest bubbles in the calculation of the total void fraction would ultimately result in an underestimation by over an order of magnitude.

Void fractions of this magnitude are considered to be insignificant when compared to the void fractions of 10^{-2} to 10^{-4} found near the surface. It is the deep-going bubbles, however, that contribute to the supersaturation of lower-solubility gases. The supersaturating effect of bubbles increases linearly with depth [*Woolf and Thorpe*, 1991; *Woolf*, 1997]. In order to assess the contribution of small bubbles to the void fraction at shallower depths, the mean SO GasEx bubble size distribution was extrapolated to 4 m using the data of *Terrill et al*. [2002], extending the SO GasEx bubble size distribution to 125 μm. The SO GasEx bubble size distribution at 4 m produced a total void fraction O(10^{-6}). Bubbles 30–125 μm in size contributed 64% of the void fraction. The remaining 36% of the void fraction was supplied by bubbles less than 30 μm in radius.

Dissolved O_2 was generally near saturation or supersaturated during SO GasEx, specifically throughout yeardays 76 and 84 discussed here (no O_2 data were collected during yearday 80) [*Moore et al*., 2011]. According to *Moore et al*. [2011], diffusive and bubble-mediated processes, rather than vertical entrainment (i.e., mixing), were largely responsible for the exchange and supersaturation of low-solubility gases during SO GasEx. The analysis of *Moore et al*. [2011] estimates the bubble contribution to O_2 using the peaked bubble size distribution of Johnson and Cooke, extending only to 30 μm. The supersaturating effect of bubbles during high wind conditions (i.e., 13 m s^{-1}) could exceed the estimated 1–2% and account for a larger portion of the measured supersaturation (perhaps up to 4–5%) by extending the bubble size distribution down to 1 μm.

5. Conclusions

Measurements of critical angle (~80°) scattering, which only arise from the difference in refractive index between air and water, and near-forward scattering together can be used to detect very small bubbles. Here measurements of scattered light at the critical angle with the MASCOT instrument and near-forward scattering with the LISST instrument demonstrated the presence of small bubbles at 6–9 m depth in the Southern Ocean. These are some of the first measurements of deeply penetrating bubbles under natural wave-breaking conditions and in different sea states.

Near-forward scattering of red light measured with the LISST instrument was used to estimate the bubble size distribution down to a bubble radius of 0.5 μm. Here, exponentially increasing concentrations of bubbles were found down to the smallest size class. This is one of the first studies to use the LISST to directly measure bubbles and we have noted several potential errors associated with the instrument. However, there was strong agreement between the bubble number concentration and size distribution slope between those measured here and from previously published research for the commonly measured size classes.

Bubbles measured during SO GasEx were exclusively very small bubbles ($a < 60$ μm) producing void fractions O(10^{-8}–10^{-7}). Extrapolation of the bubble size distributions measured at 6–9 to 4 m depth extended the maximum bubble size to 120 μm radius and produced a void fraction on the order of 10^{-6}. Although mainly composed of the larger bubbles, the small (<30 μm radius) previously neglected bubbles supplied 36% of the total void fraction. Therefore, the nature of the bubble size distribution down to the smallest size classes is particularly relevant in quantifying the bubble-mediated transfer and supersaturation of low-solubility gases. The supersaturating effect of bubbles could exceed the estimated 1–2%–4–5% by extending the bubble size distribution down to 1 μm.

The data set presented here is limited to only a handful of stations; nonetheless, it provides a foundation for more theoretical and experimental research on the existence, prevalence, persistence, and implications of such small bubbles in the ocean. Future research will involve further validation of and investigation into the presence and fate of such small bubbles, including their size distributions, the associated physical mechanisms producing the plumes, and their contribution to air-sea gas flux.

Acknowledgments
This research was supported by NASA's Ocean Biology and Biogeochemistry Program (NNX08AB10G, Dierssen). Additional support was also provided by NOAA (NA07OAR4310094, Zappa) and NSF (0647667, Zappa). We thank Scott Freeman and Christopher Buonassissi for the collection of optical data, James Edson and Wade McGillis for the collection and processing of the meteorological and acoustical data, Barney Balch for providing helpful comments, Dmitriy Leykekhman for assistance in data analysis, and Thomas Moore and Michael DeGrandpre for providing O_2 measurements. We also thank three anonymous reviewers and Xiadong Zhang for providing helpful comments that have substantially strengthened this paper.

References

Agrawal, Y. C., and H. C. Pottsmith (2000), Instruments for particle size and settling velocity observations in sediment transport, *Mar. Geol.*, *168*(1–4), 89–114, doi:10.1016/S0025-3227(00)00044-X.

Agrawal, Y. C., and P. Traykovski (2001), Particles in the bottom boundary layer: Concentration and size dynamics through events, *J. Geophys. Res.*, *106*(C5), 9533–9542, doi:10.1029/2000JC900160.

Andrews, S. W., D. M. Nover, J. E. Reuter, and S. G. Schladow (2011), Limitations of laser diffraction for measuring fine particles in oligotrophic systems: Pitfalls and potential solutions, *Water Resour. Res.*, *47*, W05523, doi:10.1029/2010WR009837.

Babanin, A. V., M. L. Banner, I. R. Young, and M. A. Donelan (2007), Wave-follower field measurements of the wind-input spectral function. Part III: Parameterization of the wind-input enhancement due to wave breaking, *J. Phys. Oceanogr.*, *37*(11), 2764–2775, doi:10.1175/2007JPO3757.1.

Balch, W. M., D. T. Drapeau, B. C. Bowler, E. Lyczskowski, E. S. Booth, and D. Alley (2011), The contribution of coccolithophores to the optical and inorganic carbon budgets during the Southern Ocean Gas Exchange Experiment: New evidence in support of the "Great Calcite Belt" hypothesis, *J. Geophys. Res.*, *116*, C00F06, doi:10.1029/2011JC006941.

Baldy, S. (1988), Bubbles in the close vicinity of breaking waves: Statistical characteristics of the generation and dispersion mechanism, *J. Geophys. Res.*, *93*(C7), 8239–8248, doi:10.1029/JC093iC07p08239.

Banner, M. L., and R. P. Morison (2010), Refined source terms in wind wave models with explicit wave breaking prediction. Part I: Model framework and validation against field data, *Ocean Modell.*, *33*(1–2), 177–189, doi:10.1016/j.ocemod.2010.01.002.

Breitz, N. D., and H. Medwin (1989), Instrumentation for in situ acoustical measurements of bubble spectra under breaking waves, *J. Acoust. Soc. Am.*, *86*, 739–743.

Broecker, H. C., and W. Siems (1984), The role of bubbles for gas transfer from water to air at higher windspeeds: Experiments in the wind-wave facility in Hamburg, in *Gas Transfer at Water Surfaces*, edited by W. Brutsaert and G. H. Jirka, pp. 229–236, Kluwer Acad., Dordrecht, Holland.

Brooks, I. M., et al. (2009), Physical exchanges at the air–sea interface: UK–SOLAS field measurements, *Bull. Am. Meteorol. Soc.*, *90*(5), 629–644, doi:10.1175/2008BAMS2578.1.

Buonassissi, C. J., and H. M. Dierssen (2010), A regional comparison of particle size distributions and the power law approximation in oceanic and estuarine surface waters, *J. Geophys. Res.*, *115*, C10028, doi:10.1029/2010JC006256.

Cifuentes-Lorenzen, A., J. B. Edson, C. J. Zappa, and L. Bariteau (2013), A multisensor comparison of ocean wave frequency spectra from a research vessel during the southern ocean gas exchange experiment, *J. Atmos. Oceanic Technol.*, *30*, 2907–2925, doi:10.1175/JTECH-D-12–00181.1.

Cifuentes-Lorenzen, A. P. (2013), The wave boundary layer over the open ocean and the implications to air-sea interaction, PhD dissertation, Univ. of Conn., Storrs.

Czerski, H., M. Twardowski, X. Zhang, and S. Vagle (2011), Resolving size distributions of bubbles with radii less than 30 μm with optical and acoustical methods, *J. Geophys. Res.*, *116*, C00H11, doi:10.1029/2011JC007177.

Deane, G. B., and M. D. Stokes (2002), Scale dependence of bubble creation mechanisms in breaking waves, *Nature*, *418*(6900), 839–844, doi:10.1038/nature00967.

Detwiler, A., and D. C. Blanchard (1978), Aging and bursting bubbles in trace-contaminated water, *Chem. Eng. Sci.*, *33*(1), 9–13, doi:10.1016/0009–2509(78)85061-1.

Edson, J. B., C. W. Fairall, L. Bariteau, C. J. Zappa, A. Cifuentes-Lorenzen, W. R. McGillis, S. Pezoa, J. E. Hare, and D. Helmig (2011), Direct covariance measurement of CO_2 gas transfer velocity during the 2008 Southern Ocean Gas Exchange Experiment: Wind speed dependency, *J. Geophys. Res.*, *116*, C00F10, doi:10.1029/2011JC007022.

Farmer, D. M., and S. Vagle (1989), Waveguide propagation of ambient sound in the ocean-surface bubble layer, *J. Acoust. Soc. Am.*, *86*(5), 1897–1908.

Farmer, D. M., S. Vagle, and A. D. Booth (1998), A free-flooding acoustical resonator for measurement of bubble size distributions, *J. Atmos. Oceanic Technol.*, *15*(5), 1132–1146, doi:10.1175/1520-0426(1998)015<1132:AFFARF>2.0.CO;2.

Fournier, G. R., and J. L. Forand (1994), Analytic phase function for ocean water, in *Ocean Optics XII* [online], vol. *2258*, edited by J. S. Jaffe, pp. 194–201, SPIE, The International Society for Optics and Photonics, Bergen, Norway. [Available at http://dx.doi.org/10.1117/12.190063.]

Garrett, C., M. Li, and D. Farmer (2000), The connection between bubble size spectra and energy dissipation rates in the upper ocean, *J. Phys. Oceanogr.*, *30*(9), 2163–2171, doi:10.1175/1520-0485(2000)030<2163:TCBBSS>2.0.CO;2.

Gemmrich, J. R., M. L. Banner, and C. Garrett (2008), Spectrally resolved energy dissipation rate and momentum flux of breaking waves, *J. Phys. Oceanogr.*, *30*, 2163–2171.

Hamme, R. C., and S. R. Emerson (2006), Constraining bubble dynamics and mixing with dissolved gases: Implications for productivity measurements by oxygen mass balance [online], *J. Mar. Res.*, *64*(1), 73–95. [Available at http://www.escholarship.org/uc/item/6c08x8p3.].

Ho, D. T., C. L. Sabine, D. Hebert, D. S. Ullman, R. Wanninkhof, R. C. Hamme, P. G. Strutton, B. Hales, J. B. Edson, and B. R. Hargreaves (2011), Southern ocean gas exchange experiment: Setting the stage, *J. Geophys. Res.*, *116*, C00F08, doi:10.1029/2010JC006852.

Johnson, B. D., and R. C. Cooke (1979), Bubble populations and spectra in coastal waters: A photographic approach, *J. Geophys. Res.*, *84*(C7), 3761–3766, doi:10.1029/JC084iC07p03761.

Johnson, B. D., and R. C. Cooke (1980), Organic particle and aggregate formation resulting from the dissolution of bubbles in seawater, *Limnol. Oceanogr.*, *25*(4), 653–661.

Keeling, R. F. (1993), On the role of large bubbles in air-sea gas exchange and supersaturation in the ocean, *J. Mar. Res.*, *51*(2), 237–271, doi:10.1357/0022240933223800.

Kingsbury, D. L., and P. L. Marston (1981), Mie scattering near the critical angle of bubbles in water, *J. Opt. Soc. Am.*, *71*(3), 358–361.

Kolovayev, P. A. (1976), Investigation of the concentration and statistical size distribution of wind-produced bubbles in the near-surface ocean layer, Oceanology, *Engl. Transl.*, *15*, 659–661.

Medwin, H. (1970), In situ acoustic measurements of bubble populations in coastal ocean waters, *J. Geophys. Res.*, *75*(3), 599–611, doi:10.1029/JC075i003p00599.

Medwin, H. (1977), In situ acoustic measurements of microbubbles at sea, *J. Geophys. Res.*, *82*(6), 971–976, doi:10.1029/JC082i006p00971.

Medwin, H., and N. D. Breitz (1989), Ambient and transient bubble spectral densities in quiescent seas and under spilling breakers, *J. Geophys. Res.*, *94*(C9), 12,751–12,759, doi:10.1029/JC094iC09p12751.

Merlivat, L., and L. Memery (1983), Gas exchange across an air-water interface: Experimental results and modeling of bubble contribution to transfer, *J. Geophys. Res.*, *88*(C1), 707–724, doi:10.1029/JC088iC01p00707.

Mobley, C. D., L. K. Sundman, and E. Boss (2002), Phase function effects on oceanic light fields, *Appl. Opt.*, *41*(6), 1035–1050.

Monahan, E. C., and M. C. Spillane (1984), The role of oceanic whitecaps in air sea gas exchange, in *Gas Transfer at Water Surfaces*, edited by W. Brutsaert and G. H. Jirka, pp. 495–504, D. Reidel, Norwell, Mass.

Moore, T. S., M. D. DeGrandpre, C. L. Sabine, R. C. Hamme, C. J. Zappa, W. R. McGillis, R. A. Feely, and W. M. Drennan (2011), Sea surface pCO_2 and O_2 in the Southern Ocean during the austral fall, 2008, *J. Geophys. Res.*, *116*, C00F11, doi:10.1029/2010JC006560.

O'Hern, T. J., L. D'Agostino, and A. J. Acosta (1988), Comparison of holographic and coulter counter measurement of cavitation nuclei in the ocean, *J. Fluids Eng.*, *110*, 200–207.
Pascal, R. W., et al. (2010), A spar buoy for high-frequency wave measurements and detection of wave breaking in the open ocean, *J. Atmos. Oceanic Technol.*, *28*(4), 590–605, doi:10.1175/2010JTECHO764.1.
Phelps, A. D., and T. G. Leighton (1998), Oceanic bubble population measurements using a buoy-deployed combination frequency technique, *IEEE J. Oceanic Eng.*, *23*(4), 400–410, doi:10.1109/48.725234.
Su, M. Y., S. C. Ling, and J. Cartmill (1987), Optical microbubble measurements in the North Sea, in *Proceedings of Workshop on Natural Mechanisms of Surface Generated Noise*, NATO ASI Ser., Ser. C, Kluwer Acad, Lerici, Italy.
Sullivan, J. M., and M. S. Twardowski (2009), Angular shape of the oceanic particulate volume scattering function in the backward direction, *Appl. Opt.*, *48*(35), 6811–6819.
Sullivan, P., and J. McWilliams (2010), Dynamics of winds and currents coupled to surface waves, *Ann. Rev. Fluid Mech.*, *42*(1), 19–42, doi:10.1146/annurev-fluid-121108–145541.
Terray, E., M. Donelan, Y. Agrawal, W. Drennan, K. Kahma, A. Williams, P. Hwang, and S. Kitaigorodskii (1996), Estimates of kinetic energy dissipation under breaking waves, *J. Phys. Oceanogr.*, *26*, 792–807.
Terrill, E. J., W. K. Melville, and D. Stramski (2001), Bubble entrainment by breaking waves and their influence on optical scattering in the upper ocean, *J. Geophys. Res.*, *106*(C8), 16,815–16,823, doi:10.1029/2000JC000496.
Thorpe, S. (1986), Measurements with an automatically recording inverted echo sounder; ARIES and the bubble clouds, *J. Phys. Oceanogr.*, *16*(8), 1462–1478.
Thorpe, S., P. Bowyer, and D. Woolf (1992), Some factors affecting the size distributions of oceanic bubbles, *J. Phys. Oceanogr.*, *22*, 382–389.
Thorpe, S. A. (1982), On the clouds of bubbles formed by breaking wind-waves in deep water, and their role in air-sea gas transfer, *Philos. Tran. R. Soc. London, Ser. A*, *304*(1483), 155–210.
Thorpe, S. A. (1992), Bubble clouds and the dynamics of the upper ocean, *Q. J. R. Meteorol. Soc.*, *118*, 1–22.
Twardowski, M., X. Zhang, S. Vagle, J. Sullivan, S. Freeman, H. Czerski, Y. You, L. Bi, and G. Kattawar (2012), The optical volume scattering function in a surf zone inverted to derive sediment and bubble particle subpopulations, *J. Geophys. Res.*, *117*, C00H17, doi:10.1029/2011JC007347.
Twardowski, M. S., E. Boss, J. M. Sullivan, and P. L. Donaghay (2004), Modeling the spectral shape of absorption by chromophoric dissolved organic matter, *Mar. Chem.*, *89*(1–4), 69–88, doi:10.1016/j.marchem.2004.02.008.
Vagle, S., and D. M. Farmer (1992), The measurement of bubble-size distributions by acoustical backscatter, *J. Atmos. Oceanic Technol.*, *9*(5), 630–644, doi:10.1175/1520-0426(1992)009<0630:TMOBSD>2.0.CO;2.
Vagle, S., and D. M. Farmer (1998), A comparison of four methods for bubble size and void fraction measurements, *IEEE J. Oceanic Eng.*, *23*(3), 211–222, doi:10.1109/48.701193.
Vagle, S., C. McNeil, and N. Steiner (2010), Upper ocean bubble measurements from the NE Pacific and estimates of their role in air-sea gas transfer of the weakly soluble gases nitrogen and oxygen, *J. Geophys. Res.*, *115*, C12054, doi:10.1029/2009JC005990.
Walsh, A. L., and P. J. Mulhearn (1987), Photographic measurements of bubble populations from breaking wind waves at sea, *J. Geophys. Res.*, *92*(C13), 14,553–14,565, doi:10.1029/JC092iC13p14553.
Woolf, D. K. (1997), Bubbles and their role in air-sea gas exchange, in *The Sea Surface and Global Change*, edited by P. S. Liss and R. A. Duce, pp. 173–205, Cambridge Univ. Press, New York.
Woolf, D. K., and S. A. Thorpe (1991), Bubbles and the air-sea exchange of gases in near-saturation conditions, *J. Mar. Res.*, *49*(3), 435–466, doi:10.1357/002224091784995765.
Woolf, D. K., et al. (2007), Modelling of bubble-mediated gas transfer: Fundamental principles and a laboratory test, *J. Mar. Syst.*, *66*(1–4), 71–91, doi:10.1016/j.jmarsys.2006.02.011.
Zhang, X., M. Lewis, M. Lee, B. Johnson, and G. Korotaev (2002), The volume scattering function of natural bubble populations, *Limnol. Oceanogr.*, *47*(5), 1273–1282.
Zhang, X., M. Twardowski, and M. Lewis (2011), Retrieving composition and sizes of oceanic particle subpopulations from the volume scattering function, *Appl. Opt.*, *50*(9), 1240–1259.

3. Novel methods for optically measuring whitecaps under natural wave breaking conditions parameterized in the Southern Ocean

This chapter is prepared for submission to the *Journal of Atmospheric and Oceanic Technology.*

Novel methods for optically measuring whitecaps under natural wave breaking conditions in the Southern Ocean

Abstract

Breaking waves on the ocean surface mark areas of significant importance to air-sea flux estimates of gas, aerosols, and heat. Traditional methods of measuring whitecap coverage using digital photography can miss features that are small in size or do not show high enough contrast to the background. The geometry of the images collected captures the near surface, bright manifestations of the whitecap feature and miss a portion of the bubble plume that is responsible for the production of sea salt aerosols and the transfer of lower solubility gases. Here, a novel method for accurately measuring both the fractional coverage of whitecaps and the intensity and decay rate of whitecap events using above water radiometry is presented. The methodology was developed using data collected during the austral summer in the Atlantic sector of the Southern Ocean under a large range of wind (speeds of ~1 to 15 m s^{-1}) and wave (significant wave heights ~2 to 8 m) conditions as part of the Southern Ocean Gas Exchange experiment. Whitecap metrics were retrieved by employing a magnitude threshold based on the interquartile range of the radiance or reflectance signal for a single channel (411 nm) after a baseline removal, determined using a moving minimum/maximum filter. Breaking intensity and decay rate metrics were produced from the integration of, and the exponential fit to, radiance or reflectance over the lifetime of the whitecap. When compared to fractional whitecap coverage measurements obtained from high resolution digital images, radiometric estimates were consistently higher because they capture more of the decaying bubble plume area that is difficult to detect with photography. Radiometrically-retrieved whitecap measurements are presented in the context of concurrently measured meteorological (*e.g.*, wind speed) and oceanographic (*e.g.*, wave) data. The optimal fit of the radiometrically estimated whitecap coverage to the instantaneous wind speed, determined using ordinary least squares, showed a cubic dependence. Increasing the magnitude threshold

for whitecap detection from 2 to 3(IQR) produced a wind speed-whitecap relationship most comparable to previously published and widely accepted wind speed-whitecap parameterizations.

3.1. Introduction

Breaking waves on the ocean surface are areas of significant importance to air-sea interaction. Whitecaps foster climate relevant physical and chemical processes in the ocean, including the production of sea salt aerosols, mixing processes, and the exchange of gas (*e.g.* CO_2, CH_4, DMS, water vapor) and heat with the atmosphere. Efforts to parameterize these processes in climate models generally incorporate an estimate of fractional whitecap coverage (*e.g.*, Monahan and Spillane [1984], Liss and Merlivat [1986], Asher *et al.* [2002], Fairall *et al.* [2003]). Typically, whitecap coverage is a combined measurement of both Stages A and B, where Stage A includes the active, spilling crest and a dense, broad bubble spectrum. Stage B is the maturing Stage A whitecap, which covers a larger area and has a relatively narrow bubble spectrum [*Monahan and Lu*, 1990]. During Stage A breaking, large volumes of air are introduced into the surface layer of the ocean (*i.e.*, the α bubble plume). Therefore, air-sea gas transfer velocities are often based on the fractional coverage of Stage A whitecaps, but since the ratio of Stage A to Stage B coverage is roughly a constant, some investigators have related the gas transfer velocity to Stage B coverage (*e.g.* Monahan and Spillane [1984]). The entrained air is fragmented during the Stage A phase, and the resulting bubbles are distributed during the Stage B phase (*i.e.*, β-plume). Bubble processes (*e.g.* dissolution, bursting, etc.) occur during and after this phase [*Monahan and Lu*, 1990]. The Stage B bubble plume is responsible for the production of primary marine aerosols and can impact heat flux [*Monahan et al.*, 1986; *Andreas et al.*, 1995]. Under moderate to high wind conditions (> 7 m s^{-1}), whitecaps can support bubble populations in uniform, persistent (3-4 hour) subsurface plumes (*i.e.* γ-plumes in the usage of Monahan and Lu [1990]), which are relevant to the supersaturation of dissolved gases in the surface ocean [*Thorpe*, 1982; *Monahan*, 1993]. Accurate, practicable techniques for quantifying the coverage and intensity of whitecaps from initiation through decay are necessary to understand these processes.

Traditional methods for estimating total whitecap coverage typically involve the analysis of high-resolution digital imagery for producing a presence/absence coverage result. Historically, imagery was processed manually using a simple "threshold" technique (*e.g.*, Nordberg *et al.*, [1971] Ross and Cardone [1974], Monahan *et al.*, [1984]), where an intensity value is selected which separates whitecaps from the background surface. This is done on an image-by-image or small batch basis because of fleeting changes in ambient illumination. A large dataset is necessary to accurately measure whitecap coverage due to the irregular nature of wave breaking. Hundreds of images must be analyzed per 20 minute sampling period to produce convergent coverage estimates [*Callaghan and White*, 2009]. To facilitate data processing, the AWE (Automated Whitecap Extraction) algorithm was developed as an automated, objective approach for threshold selection [*Callaghan and White*, 2009]. However, AWE and other automated techniques (*e.g.*, grayscale thresholding by Sugihara *et al.* [2007]) require very high quality images free of sun glint and sky reflectance and with homogeneous illumination that are often challenging to obtain in the field.

Threshold techniques have also been used to separate total whitecap coverage into Stage A and B phases using two intensity values (*e.g.*, Ross and Cardone [1974] and Monahan and Woolf [1989]). However, these methods suffer the same pitfalls as the single threshold technique and may not capture consistent portions of the whitecap stages. Recently, a spatial separation approach was developed for differentiating coverage type by incorporating relationships to the wave field, texture, and slope. This multi-parameter method is more robust, but is labor intensive, subjective and requires manual selection of Stage A and B pixels [*Scanlon and Ward*, 2013]. Most importantly, the geometry of the images collected using digital camera systems captures only the near surface, very bright manifestations of the whitecap feature. Whitecaps small in size or which don't produce a sufficiently strong contrast to the background are missed altogether [*Callaghan and White*, 2009]. Furthermore, in every case, the traditional method misses a portion of the bubble plume. Because whitecaps have a pronounced effect on the magnitude of visible light leaving the ocean surface (*e.g.*, Koepke [1984], Frouin *et al.* [1996], Moore *et al.* [2000],

Stramski and Tegowski [2001], Terill *et al.* [2001], and Zhang *et al.* [2002]), they are easily detected in measurements of optical radiance. Simple, high frequency, point-based (small FOV) measurements of radiance can be implemented to capture some of the elusive whitecap features.

The magnitude of light reflected from the sea surface is significantly enhanced due to foam and bubble entrainment from breaking waves on temporal scales of seconds to tens of seconds [*Terrill et al.*, 1998; *Stramski and Tegowski*, 2001]. Foam shows a spectrally flat response in that it reflects equally across all visible wavelengths and appears white (*e.g.*, Stabeno and Monahan [1986], Frouin *et al.* [1996], Moore *et al.* [2000]). As the whitecap matures, the spectrally flat feature takes on a shape. A decrease in reflectance occurs in the red portion of the spectrum due to the strong absorption properties of water molecules [*Frouin et al.*, 1996; *Moore et al.*, 1998]. Furthermore, the spectral shape in the blue and green changes to one dependent on the optical properties of the water (*e.g.*, the measurement is of the bubbles and the water between them) [*Moore et al.*, 1998; *Stramski and Tegowski*, 2001; *Kokhanovsky*, 2004; *Zhang et al.*, 2004]. The effect of whitecaps on the magnitude and shape of visible light leaving the ocean surface have been presented in previously published studies (*e.g.*, Koepke [1984], Frouin *et al.* [1996], Moore *et al.* [2000], Stramski and Tegowski [2001], and Zhang *et al.* [2002]). Most of these measurements were collected over ship generated foam and bubbles (e.g., Moore *et al.* [1998]) or their effects were modeled using radiative transfer (*e.g.*, Stramski and Tegowski [2001]) and none were directly compared to coverage measured simultaneously using traditional techniques (*e.g.*, Monahan and Spillane, 1984).

A novel method for retrieving whitecap coverage and wave breaking intensity metrics using radiance measurements collected from single and double sensors systems deployed on the bow of a ship in the Southern Ocean under a wide range of physical forcing and wave breaking conditions is presented here. The Southern Ocean is an excellent region to develop and test these methods due to the occurrence of strong unimpeded winds resulting in large waves and whitecaps. Whitecap metrics resolved using

radiometry are reported in the context of simultaneously collected meteorological and oceanographic measurements and are compared to whitecap coverage retrievals conducted with traditional digital imaging. Our research has shown high intensity breaking in this region, producing bubble plumes which penetrate to ~10 m depths (*e.g.* Randolph *et al.* [2014]). A major advantage of this method is that it is quantitative and robust, capturing more of the decaying whitecap feature than traditional techniques. Dynamic detector positioning at specific look angles can be employed to optimize the signal to noise ratio.

3.2. Background

3.2.1. Radiometric Quantities

Upwelling radiance from the surface ocean is dependent on the water optical properties, the geometric structure of the incident radiance distribution (*i.e.*, solar zenith angle), the geometry of the surface, and the illumination conditions (*e.g.* cloud cover). It is a directional quantity measured over a time, area, solid angle and wavelength interval. Here, the total upwelling radiance signal above the sea surface, $L_t(\theta, \phi)$, is the spectral distribution of light, or radiant power per unit area, wavelength and solid angle (W m^{-2} nm^{-1} sr^{-1}), emerging from the ocean in polar and azimuthal directions θ and ϕ

$$L_t(\theta,\phi), = \ L_w(\theta,\phi) + L_r(\theta,\phi) + L_{WC}(\theta,\phi)$$

where L_w is the radiance signal of the undisturbed water column, L_{WC} is the radiance signal from whitecaps (*i.e.*, foam and bubbles), and L_r is the surface reflected portion of the incident sky radiance, L_s (Figure 1). Whitecap radiance is not directly measureable, but can be inferred from measurements of L_t.

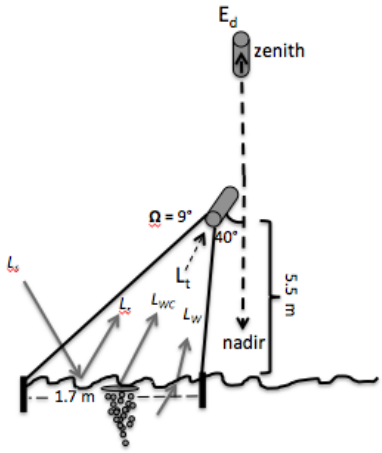

Figure 1: Radiance from the surface ocean under windy conditions. The total measured upwelling radiance, $L_t(\theta, \phi)$ includes the water column component, $L_w(\theta, \phi)$, the whitecap component, $L_{WC}(\theta, \phi)$ and the surface reflected portion, $L_r(\theta, \phi)$, of the incident sky radiance, $L_s(\theta', \phi')$.

3.2.2.Time-to-space comparison

Typically, hundreds of digital images with a large footprint are required per 20-minute sampling interval to retrieve converging estimates of fractional whitecap coverage due to the intermittent, often infrequent, and non-uniform nature of wave breaking [*Callaghan and White*, 2009]. There are trade-offs between producing coverage estimates that are stable (*i.e.*, converging, by increasing the dataset size) and also representative of the forcing conditions. Increasing footprint size produces larger deviations in background pixel intensities (*e.g.*, increasing influence of sky reflectance), making the selection of a threshold for differentiating whitecaps from the background difficult. Smaller footprints, however, require a larger number of images to be used in retrieving accurate coverage estimates. Collecting many high frequency measurements of an ~1 m instantaneous field of view is an alternative (and some say equivalent) to capturing a large area at any instant (*e.g.*, Wang *et al.* [1995] and Moore *et al.* [1998]). A comparison between cameras measuring whitecap coverage within a larger footprint to a microwave radiometer/camera system measuring a small (~1 m^2) footprint produced consistent results, substantiating

the use of high frequency measurements of very small areas for accurately predict spatially-averaged whitecap coverage [*Wang et al.*, 1995]. Similarly, Moore *et al.* [1998, 2000] reported the coverage of thick to residual foam patches by taking many reflectance measurements of a small area on the water surface (1° FOV).

When measuring a small area, the longer the record length, the better the statistical base for any single coverage estimate; however, the associated meteorological and oceanographic conditions change on relatively short time scales. The wrong record length choice could introduce biases in coverage estimates as a result of different sea states and types of breaking (*e.g.*, spillers or plunging breakers). For example, well-developed seas with low frequency, but high intensity breaking would require a longer time series to sample accurately compared to developing seas with high frequency, low intensity breaking. When a generic record length is required, it should be decided based on the lowest frequency of breaking to be resolved.

Our method proposes to use a continuous time series of radiance measurements within a small footprint to represent the spatial estimate of whitecap coverage. The associated spatial coverage of the point-based sampling approach can be approximated and optimized using the length of the footprint and the record and an estimate of the surface drift velocity. For stationary radiance measurements (*i.e.*, speed over ground < 1 m s^{-1}) collected while the ship maintained a constant heading into the wind, the surface area advected past the instrument, *A*, was approximated following

$$A(\Delta t, L, u_o) = \pi\ (L\ u_o\ \Delta t)$$

where *L* is the diameter of the IFOV (m), Δt is the time interval of sampling (*i.e.*, record length), and u_o (m s^{-1}) is the surface drift velocity. The surface drift velocity is assumed to be the advection velocity associated with a passing whitecap and was approximated following Wu [1983]:

$$u_o = \alpha\ u_*$$

where u_* (m s^{-1}) is the atmospheric friction velocity and α is a numerical constant (α = 0.53). Here, record lengths were optimized so that A~1 km^2, a relevant spatial resolution for ocean color data. The whitecap coverage, a, over the time interval Δt is given by

$$a(\Delta t) = A\, w_c$$

where w_c is an estimate of the whitecap coverage given the physical or meteorological conditions (*i.e.*, U_{10}; m s^{-1}).

The number of independent events within the time interval, $N(\Delta t)$ can be estimated from

$$N(\Delta t) = \frac{a(\Delta t)}{a_{wc}}$$

where a_{wc} is the area (m^2) of the individual whitecaps. The number of independent events for a given wind speed can be estimated using the individual whitecap area presented by Bondur and Sharkov [1982].

Finally, the surface renewal time, t_r (s) is the ratio of the diameter of the IFOV to the surface drift velocity.

$$t_r = L/u_o \qquad (5)$$

For example, for a surface drift velocity of 0.3 m s^{-1}, the surface renewal time is 3.3 s (0.30 Hz). An instrument with a sampling rate of 7 Hz (typical for radiometer systems described here) and a Nyquist frequency of 3.5 Hz can be used to resolve features with a maximum surface drift velocity of 3.6 m s^{-1}. These conditions could allow for underway sampling.

3.3. Development of Method

3.3.1. Instruments and configuration

The total contribution of wave breaking to radiance can be captured at high frequency above the sea surface using a multispectral or single channel radiometer (*e.g.*, OCR 500, Satlantic). A single channel radiometer at visible wavelengths (here 411 nm) is sufficient to capture the full whitecap feature (*e.g.*, Stage A through the decaying bubble plume). The radiometer is configured to collect data over an

azimuthal range of 270° across the heading of the ship while the solar zenith angle is above 20°. Sun glint and shadowing effects are minimized by maintaining a viewing direction 120° from the sun's azimuth. A viewing angle 40° from nadir is employed to minimize specular reflectance of the sun's direct beam into the detector [*Mueller et al.*, 2003]. Proper viewing angles can be maintained using a computer-based system that calculates the sun's azimuth angle relative to the ship and adjusts the position of the detector using a stepping motor (see Balch *et al.* [2011]). An integrated dynamic positioning system for radiometers is now commercially available (*e.g.*, Satlantic, LP). The down-looking radiometer is positioned above the water surface to maintain an ~1 m^2 instantaneous field of view. Our analysis found that 20 minute segments of the high frequency, upwelling radiance signal (L_t) could be used to successfully resolve fractional whitecap coverage from $1x10^{-4}$ to 0.07. While a calibrated, dark corrected signal is preferred if making quantitative comparisons of intensity and duration of whitecaps between regions, the data is normalized to a baseline, which removes most of the calibration artifacts and whitecaps are evaluated as relative enhancements to the radiance signal. Under shifting sky conditions, it is not necessary but advantageous to have simultaneously collected downwelling irradiance (E_d) measurement to normalize the radiance to the incident irradiance.

3.3.2. Identifying Whitecap Features

The time series of radiometric measurements are analyzed to retrieve whitecap metrics (*i.e.*, coverage, intensity, duration, and decay rate) following the basic procedure outlined in Figure 2. Whitecap features are retrieved from the total radiance signal after removing a baseline. Unpredictable fluctuations or trends in the illumination conditions or changes in L_w (*e.g.* the color of the water column without bubbles or foam) can result in a non-stationary L_t signal, producing mean and variance values that change over time. A stationary upwelling radiance time series (L_t') can be estimated from the measured, non-stationary L_t signal by applying a moving minimum-maximum filter (*e.g.* Briggs *et al.* [2011]) following Lemire [2006]. Ideally, the baseline captures all changes in illumination conditions, eliminating the need for normalizing L_t to the measured downwelling irradiance at each time step. The baseline also accounts for

magnitude differences in L_t between stations due to spectral changes in the water color itself, or L_w. The moving min-max filter simultaneously finds the minimum and maximum elements within a sliding window of a specified length. The window size is optimized such that the time interval is short enough to remove variations in radiance due to changing illumination conditions, while being long enough not to erode whitecap features. At a minimum, the window size should be at least the length of the longest feature to be retrieved (~40 s). During uniform sky conditions, L_t is stationary over the time interval necessary to capture whitecap metrics and long window lengths are realistic. However, nonuniform skies require shorter window lengths for L_t to approach a stationary condition and potential errors can arise in identifying the limits of the whitecap feature. Here, a single, optimized window size of 15 s was used for all stations with minimal error. If necessary, applying station-specific window sizes (based on the prevailing illumination conditions) is a reasonable approach and is easy to implement.

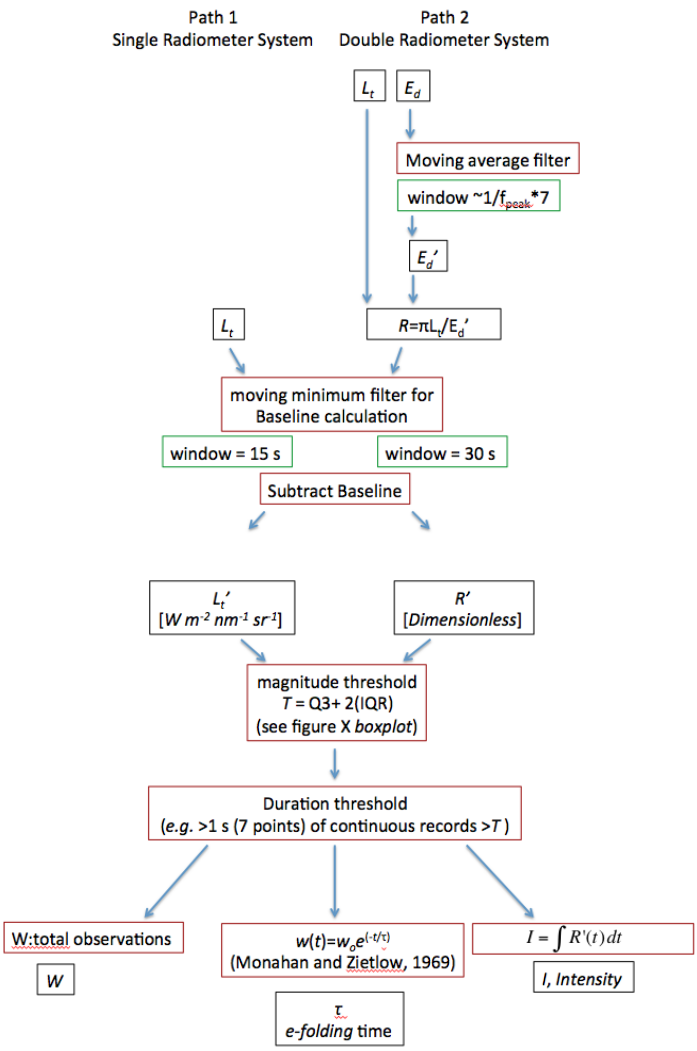

Figure 2: Procedure for retrieving whitecap metrics (*i.e.*, coverage, decay rate and intensity) from measurements of radiance (L_t; Path 1) and irradiance (E_d, optional; Path 2).

Under highly variable sky condition, identification of the whitecap feature can be detected more accurately if downwelling irradiance (E_d; W m^{-2} nm^{-1}) is measured simultaneously with the upwelling radiance. This approach requires the deployment of a second, upward looking radiometer outfitted with a cosine collector, to measure the downward plane irradiance incident on the sea surface (see Figure 2, Path 2). In theory, the pseudo-reflectance term, R (sr^{-1}), which is the ratio of $L_t(t)$ to $E_d(t)$, accounts for

changes in the illumination conditions and produces a stable measurement of the water and whitecaps. Assuming the measured $L_t(\theta, \phi)$ is the same across all viewing directions (θ and ϕ) a Lambertian Equivalent Reflectance (*LER*) can be estimated by multiplying by π and the measurement becomes similar to a dimensionless albedo, hereafter *R'*. The E_d sensor must be deployed in a location where it is unaffected by ship-shadow, typically high up on the jackstaff of a ship [Zibordi *et al.*, 2014]. It is difficult to gimbal the instrument so that it remains plane parallel when deployed on a dynamic platform. For the Southern Ocean, the instrument oscillated between nadir (0°) and ~3° to 5° in any direction [*Cifuentes-Lorenzen et al.*, 2013].

Slight changes in the look angle of the sensor due to ship motion can produce regular fluctuations in the E_d signal at approximately the period of the swell (*e.g.*, ~10 s). Therefore, before calculating *R'*, the high frequency E_d data can be filtered using a technique such as a moving average, where the window length is at least as long as the swell period. Here, the peak frequency of motion-induced fluctuations, determined from the average power spectral density of E_d (~1 min segments) was used as the window length for the moving average filter. This automated and objective filtering approach removes low magnitude variance as a result of changing look angle, but maintains trends in *R'* for use in the calculation of whitecap features following the same baseline removal process described above.

The baseline-removed, *L'* or *R'* record has a distribution that is positively skewed to a degree dependent on the presence of bright foam, bubbles (*e.g.*, the more whitecaps, the heavier the tail), and glint. Glint acts a signal contaminant and presents as randomly occurring, very bright features lasting <2 s in duration. The width of the *L'* or *LER'* distribution (variance, σ^2) is dependent on skylight reflected off of the wavy surface (L_r), another signal contaminant. The frequency and magnitude of variance in the upwelling radiance signal is the result of time-varying features of the different types of waves, including gravity waves on the order of meters in length to capillary waves on the order of millimeters in length, at each time step. The greater the surface reflected skylight, the larger the variance in the background signal

and the more difficult identifying whitecaps becomes, especially in the case of low intensity breaking (*i.e.*, spilling waves).

Whitecaps can be identified in the L_t' or R' record using a number of different methods depending on the needs of the user. Here, a station-specific threshold was determined using a single, objective approach that is fairly robust to outliers. The interquartile range (IQR) of L' or R' was calculated as the difference between the 75th (Q3) and 25th (Q1) percentiles. The magnitude of the IQR is dependent on the surface reflected skylight, which is, in turn, dependent on the wave and illumination conditions. Uniform skies and a flat ocean yield low IQR and variable skies and a roughened sea surface yield high IQR. Outliers (or breaking waves) are defined as samples greater than Q3+ 2(IQR). For normally distributed data, whisker lengths are typically set to 1.5IQR, which corresponds to 2.7σ (or 99.3 coverage). After the threshold has been applied, any remaining non-whitecap, transient bright features (*e.g.*, glint) are removed from the signal using a de-spiking procedure based on feature duration. Any bright features lasting <2 s are considered glint features and deemed non-whitecap.

3.3.3. Wave breaking metrics

Fractional whitecap coverage can be calculated as the fraction of the total record that was identified as a whitecap feature. Coverage can be parsed into stages (*e.g.*, A and the α-plume, B and the β-plume, and finally the γ-plume) by specifying intensity intervals representative of each stage (*e.g.*, Moore *et al.* [1998]). Intensity (or brightness) intervals can be chosen to be consistent with the published physical properties of the A, B and γ-plume stages [*Donelan et al.*, 1972; *Bondur and Sharkov*, 1982b; *Stabeno and Monahan*, 1986; *Bortkovskii*, 1987; *Monahan*, 1989; *Callaghan*, 2013].

The sampling duration for producing statistically robust fractional whitecap coverage estimates must be considered. If the record length is too short, the variance will be too high to produce stable whitecap metrics. In theory, under strong forcing conditions with whitecap coverage O(0.01), 10 whitecap

realizations are retrieved per every 1,000 points recorded, which corresponds to a ~140 s or a 2 minute record. For low coverage days (*e.g.*, *W*~0.001), 10 points of whitecap realizations are retrieved per every 10,000 points recorded, which corresponds to a ~1400 s or 23 min record. For comparison purposes, 20-minute segment lengths, which can resolve fractional coverage O(10^{-4}), are commonly reported when using digital imaging techniques. In reality, whitecaps are non-uniform in space and time and breaking frequency is strongly dependent on the forcing conditions (see Section 2.2). A sensitivity analysis illustrating the space-to-time relationship is presented below based on the Southern Ocean data. Finally, The relationship between neutral wind speeds at 10 m and radiometrically-retrieved whitecap coverage estimates was investigated using ordinary least squares and compared to previously published wind speed-whitecap parameterizations (*e.g.,* Monahan and O'Muirchaertaigh [1980] and Stramska and Petelski [2003]).

The radiometric approach also allows for the estimation of other whitecap metrics beyond fractional coverage. For example, a whitecap decay rate τ can be estimated from R' estimated for individual whitecap events considered to be complete. Following Monahan and Zietlow [1969], τ is calculated as the exponential fit from the L' *or* R' measured at the initial time of the peak (*0*) to the final whitecap realization (t_f) where t is (t_f-t_0) following:

$$LER'^{(t_f)} = LER'(t_0)e^{-t/\tau}$$

The duration and maximum brightness of each measured whitecap was used to identify full or near full events (rather than partial events) for calculating decay rate and intensity metrics. When applied to the upper 75th percentile in duration and brighness, the *e*-folding times produced using the radiometric method were found to be comparable to those published in the literature (*e.g.*, ~3.5 to 4.5 s) [*Monahan and Lu*, 1990; *Callaghan*, 2013].

The measured radiance can also be integrated over the time length of the whitecap to provide an indicator of the magnitude of the whitecap event. This term, defined here as the whitecap reflectivity factor, physically related to the breaking intensity, (I) can be estimated from the L' *or* R' measurements from the start of the feature (t_i) to the end of the feature (t_f) following:

$$I = \int_{t_i}^{t_f} R'(t)dt$$

3.4. Measurements

The methodology presented here was evaluated using data collected as a part of the Southern Ocean Gas Exchange Experiment (SO Gasex) conducted on the NOAA ship the *R.V. Ronald H. Brown* in the Atlantic sector of the Southern Ocean (50°S, 40°W) from March 7 to April 4, 2008. The primary objective of SO GasEx was to measure gas transfer at high wind speeds and to identify predictors, in addition to wind, for estimating gas transfer [*Ho et al.*, 2011]. Bubbles generated by breaking waves were measured as a part of this study [*Randolph et al.*, 2014]. A Lagrangian approach was taken to study relevant physical, chemical, and biological processes.

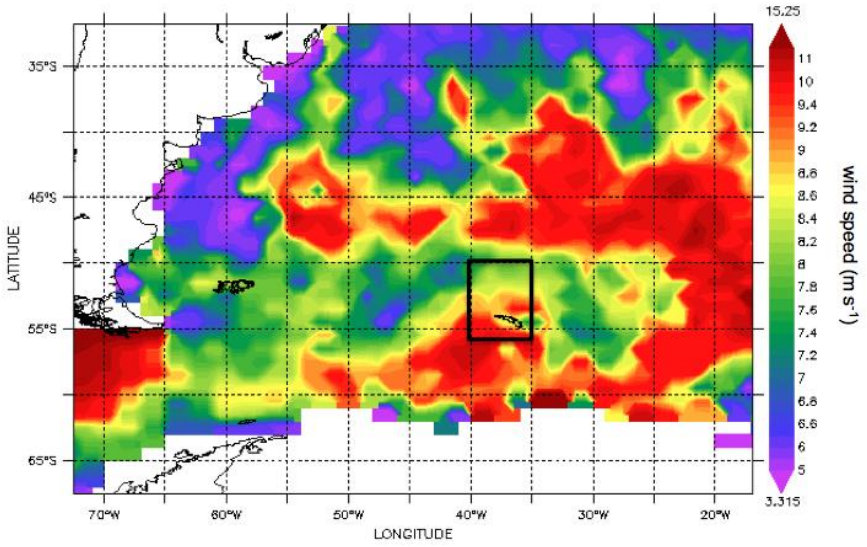

Figure 3: (a) The South Atlantic sampling region with the mean monthly AQUARIUS estimated wind speed (m s^{-1}) for the month of March and the SOGasEx sampling location (black box) from NASA JPL.

Two tracer patches were deployed lasting 6 and 15 days in duration, respectively. Measurements were collected at stations primarily north of South Georgia Island at a latitude of 51°S in a region characterized by moderate phytoplankton biomass and prone to high wind conditions, as shown in the satellite-derived average QuikSCAT wind speed imagery for March 2008 (Figure 3). During yeardays 75 to 77, the sampling stations were located approximately 300 km further south at a latitude of 54°S in waters surrounding South Georgia Island.

3.4.1. Radiometry

Radiometric data were collected as a 0.5~2.5 hour time series while on station and from 11:00 to 16:00 GMT, during which the ship maintained a constant heading. Three radiometric sensors were deployed, including a downwelling irradiance sensor measuring E_d (μW cm^{-2} nm^{-1}) and down-looking and sky-viewing radiance sensors measuring L_t (μW cm^{-2} nm^{-1} sr^{-1}) and L_r (μW cm^{-2} nm^{-1} sr^{-1}), each with 7 channels between 412 and 680 nm (10 nm spectral bandwidth) (Figure 4). The downwelling irradiance and sky-viewing radiance signals were collected to aid in the development of the methods, but are not essential for implementation of the method. The radiance sensors have a 9° FOV and were deployed from the bow of the ship, 5.5 m above the waterline. The downwelling irradiance sensor was mounted upward-looking and in a location unaffected by ship-shadow on the jackstaff of the ship at 18 m. The sea and sky-viewing radiometers were deployed at the bow and set to maintain the viewing angles outlined in Section 3.1. The down-looking radiometer was positioned ~8 m above the water surface, resulting in an ~1.5 m instantaneous field of view. Radiometric data was processed in Prosoft (Satlantic, Inc.) to produce calibrated, dark corrected data interpolated onto common time coordinates.

Figure 4: The three radiometric sensors deployed during SO GasEx, including (a) a downwelling irradiance sensor mounted on the top of the jackstaff at 18 m and (b) down-looking and (c) sky-viewing radiance sensors deployed at the bow. The downwelling irradiance and sky radiance signals are used as ancillary data and are not required in retrieving whitecap metrics. Proper viewing angles were maintained using a computer-based system that calculated the sun's azimuth angle relative to the ship and adjusted the position of the detectors using a stepping motor. A Bruce Bowler (Bigelow Research Labs) design, now available commercially.

3.4.2. Upper Ocean Dynamics

In addition to radiometric measurements, whitecap coverage was estimated using high-resolution digital images from two Imperx CCD cameras sampling 100 m^2 areas at 5 Hz from the Flying Bridge (port and starboard side looking) of the *RV Ronald Brown* [*Zappa et al.*, 2012]. Lens distortion effects were removed following Bouguet [2004] and a motion correction (*i.e.*, pitch, roll and yaw) was applied using the inertial motion unit measured angular rates. Background intensity gradients were removed and breaking statistics were determined using the approach of Callaghan and White [2009].

Neutral wind speeds at the reference height of 10 m (U_{10N}), were measured using an air-sea flux package deployed on the jack-staff of the ship [*Edson et al.*, 2011]. The wave frequency spectrum from 0.03 to 1.2 Hz was determined by combining measurements from a Wave Monitoring System (WaMoS II), a

Riegl LD-90 laser altimeter, and a TSKA SWHM wave height meter [*Cifuentes-Lorenzen et al.*, 2013]. Wave field statistics, including the significant wave height of the dominant waves (H_s) and the phase speed at the spectral peak (c_p) were determined from the measured wave frequency spectrum. Variables describing the state of the wind-wave field, including inverse wave age or wind forcing (U_{10}/c_p) were also derived from the measured wave number and frequency spectra. For open ocean conditions, high inverse wave age values (*i.e.*, $U_{10}/c_p > 0.82$) are considered young or developing seas, while low values (*i.e.* $U_{10}/c_p < 0.82$) are considered old or developed seas. The threshold, $U_{10}/c_p \sim 0.82$, is considered mature or fully developed. Wind and wave metrics were used to investigate deviations in the radiance-derived whitecap coverage from the published wind speed-whitecap parameterizations (*e.g.* Monahan and O'Muircheartaigh [1980]).

3.5. Assessment

The large range in the meteorological, sea, and sky conditions (*e.g.*, wave age, wind speed, cloud cover) measured during SO GasEx make the dataset ideal for assessing the robustness of the methodology presented here and in identifying its limitations (Table 1). A sensitivity analysis illustrating the record length necessary for retrieving a stable whitecap measurement is presented. Potential sources of error using Path 1 and 2 are addressed and recommendations for their application are made. A comparison between radiometrically-retrieved coverage and coverage from the traditional, digital imaging technique is presented. Radiometrically-retrieved whitecap measurements are presented in the context of concurrently measured meteorological and oceanographic data. The dependence of the whitecap coverage estimated here on wind speed is explored using ordinary least squares and the resulting relationship is compared to previously published and widely accepted wind speed-whitecap parameterizations.

Table 1: A summary of the fractional whitecap coverage estimates from the radiometric (W_R) and digital imaging (W_D) techniques in wind speed increments of 2 m s^{-1}. The difference between the mean whitecap coverage estimates for each bin from the two techniques is reported and the mean values were compared using a left-tailed t-test assuming unequal variances. When the two means were determined to be statistically significantly different (α=0.05), the p-values were reported. Other oceanographic measurements including the significant wave height (H_s), inverse wave age (U_{10}/c_p, where c_p is the peak phase speed in m s^{-1}), and the range in atmospheric stability ($\Delta T = T_{air} - T_{water}$) are presented to offer context for the W results.

Wind speed range	n	W_R [ste]	W_D [ste]	$d_{2(IQR)}$* (factor)	*p-value* (α=0.05)	H_s (m)	U_{10}/c_p (range)	ΔT (°) (range)
4-6	7	0.0019 [0.0011]	0.0012 [0.0004]	1.6		7.2	0.29 - 0.43	-0.13 - 0.99
6-8	5	0.0092 [0.0026]	0.0016 [0.0004]	5.8	0	12.4	0.36 - 0.63	0.01 - 1.95
8-10	35	0.0150 [0.0012]	0.0054 [0.0007]	2.8	0	13.4	0.38 - 0.64	-3.05 - 2.38
10-12	11	0.0194 [0.0029]	0.0087 [0.0010]	2.2	2.0×10^{-4}	13.4	0.42 - 0.72	-0.47 - 2.61
12-14	21	0.0315 [0.0026]	0.0202 [0.0027]	1.6	1.7×10^{-2}	5.14	0.68 - 0.97	-2.41 - 3.16
>14	6	0.0546 [0.007]	0.0337 [0.0042]	1.6	2.4×10^{-2}	7.7	0.97 - 1.05	1.37 - 1.57

*Factor of 2.6 difference on average

Over 35 hours of radiometric data collected while on station in the Southern Ocean was used to assess the whitecap retrieval methodology presented here. The use of a single sensor (*i.e.*, Path 1), which makes for a simple deployment and eliminates the need for two inter-calibrated radiometers, was considered here. Under most sea and sky conditions in this study, the baseline removal provided an effective means of accounting for both changing illuminations conditions and water column optical properties. Three, 20-minute L_t records collected under low (~3 m s^{-1}), moderate (~7 m s^{-1}), and high (14 m s^{-1}) wind conditions illustrate the strengths and limitations of following the Path 1 approach (Figure 5). While on station,

variation in L_w within the 15 s time interval was negligible and was accounted for in the Path 1 baseline removal. The running minimum was also effective in capturing most changes in E_d over a large dynamic range (Figure 5a). However, when the trend in E_d was steep and negative over time (Figure 5a inset; Figure 6 black line), the moving minimum filter underestimated the baseline, resulting in an overestimation of L' (Figure 5d, inset). While the moving minmax filter was not optimal under these conditions, the resulting slight overestimation did not produce an overestimation of W because the affected samples remained below the magnitude threshold.

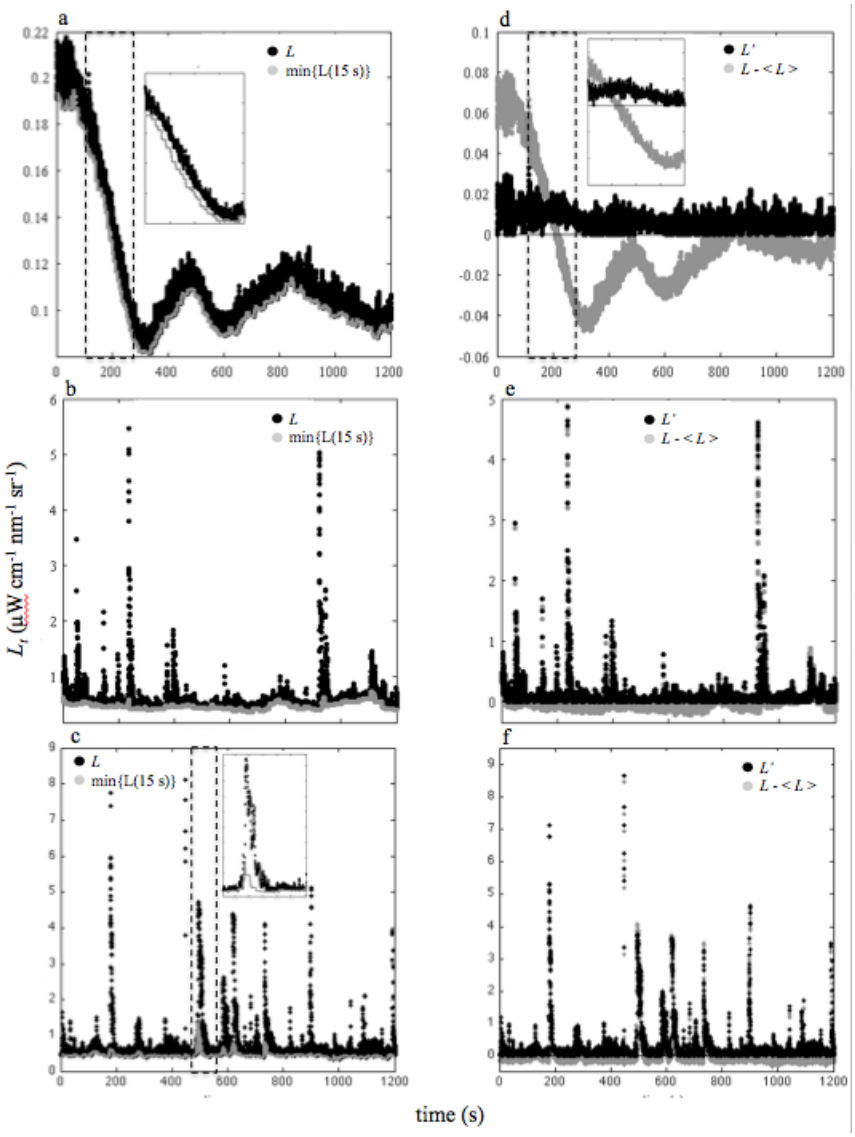

Figure 5: 20-minute records of L_t (black circles) and moving minmax filtered L_t (grey circles) collected under (a) low (yearday 86, mean U_{10}~3 m s^{-1}) (b) moderate (yearday 89, mean U_{10}~7 m s^{-1}) and (c) high (yearday 76, mean U_{10}~10 m s^{-1}) wind conditions and (d,e,f) the associated L' signals (black circles) shown with the detrended L_t signal for reference. (a, inset) Steep trends in downwelling irradiance (see Figure 7) are not well captured by the moving minmax filter, (d, inset) resulting in an overestimation of L'. (c, inset) For whitecap events lasting longer than 15 s in duration, the moving minmax filter (15 s window) will erroneously remove a portion of the whitecap feature with the baseline when following the Path 1 approach.

While the Path 1 approach was effective at capturing breaking events lasting 15 s or less in duration (*e.g.*, Figure 5b, e), high intensity breaking was better characterized and quantified following the Path 2 approach. For whitecap events lasting longer than 15 s, local minima occur within the event itself, therefore a portion of the whitecap feature was removed with the baseline (Figure 5c, f). Small window sizes did not impact the coverage metric because the foam features remained well above the magnitude threshold, but they appeared less bright resulting in an underestimation of breaking intensity. The Path 2 approach used E_d to account for changing illumination conditions to maximize the window size. Under overcast sky conditions (*e.g.*, sun not visible), irradiance data were not affected by an E_d sensor tilting ~3° in any direction due to ship motion and no filtering was required. Under non-uniform or clear sky conditions (true for three SO GasEx stations, including days 75, 76, and 94), low magnitude fluctuations in a non-gimbaled E_d instrument occurred due to slight changes in the look angle from ship motion (Figure 6). The small, motion-induced fluctuations in E_d resulted in large variance noise in R and the high frequency E_d data were filtered using a moving average based on the maximum time extent of the peak in the E_d frequency spectrum (Figure 7).

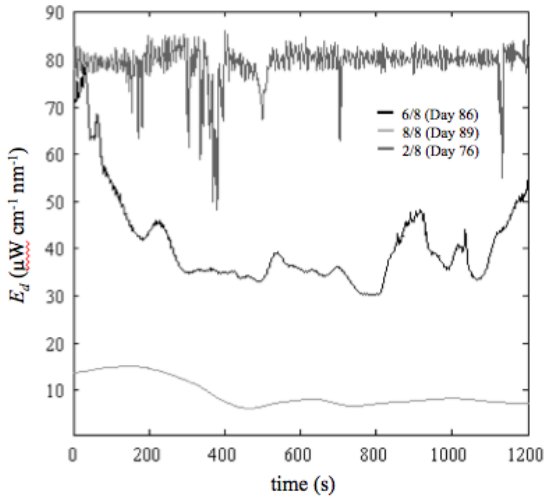

Figure 6: 20-minute records of E_d corresponding to the *L'* records in Figure 6 for yeardays 86 (black line), 89 (light grey line), and 76 (dark grey line) experiencing low, moderate and high wind speeds. Cloud conditions, presented in eighths, were 6/8, 8/8 and 2/8 respectively, where 0/8 indicates clear skies and 8/8 indicates overcast. Mostly clear skies on Day 76 resulted in an evenly distributed, high frequency, low magnitude variance throughout the record due to ship motion as the look angle of the detector tilted ~3° into and out of the plane of the sun (dark grey line).

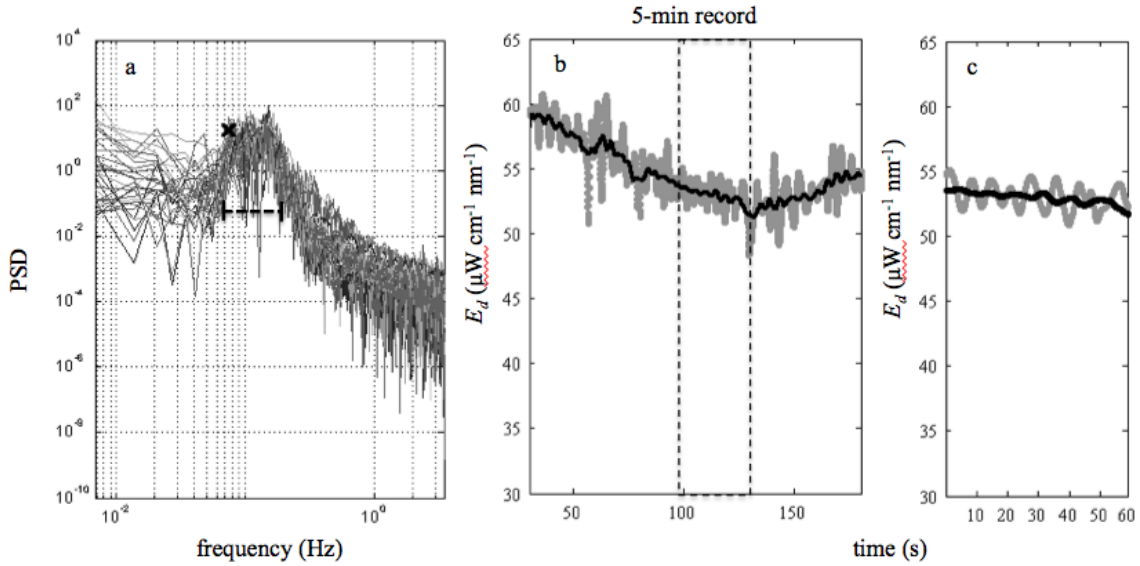

Figure 7: (a) The peak in the power spectrum of the E_d signal (denoted by the black dotted line), which coincides with the period of the swell, was used to remove the (b, c; grey line) low magnitude fluctuations in E_d due to slight changes in the look angle as a result of ship motion. (b, c; black line) Under non-uniform or clear sky conditions, the high frequency E_d data was filtered using a moving average where the window length was based on the maximum time extent of the (a, black x) PSD peak (*i.e.*, 14 s).

The Path 2 approach was used to detect and evaluate the long (~35 s) whitecap events observed during Day 76. Whitecap metrics were calculated for each 20-minute segment of radiometric data (8400 samples). The E_d signal was filtered using a moving average, order 1 with a window size of 14 s (Figure 8). The ratio of the raw L_t data to the moving-average filtered E_d data produced the reflectance term, R. Application of the running minmax filter with a window size of 35 s to the R signal resulted in a baseline that did not erroneously include a portion of the whitecap feature, unlike when the minmax filter with a 15 s window was applied to L (Figure 8a and b, pluses). The moving minimum approach offered only a low frequency approximation of the ambient illumination conditions whereas a high frequency measurement of E_d was used in the calculation of R', therefore the shapes of the L' and R' signals were similar but not identical (Figure 8, example indicated with stars).

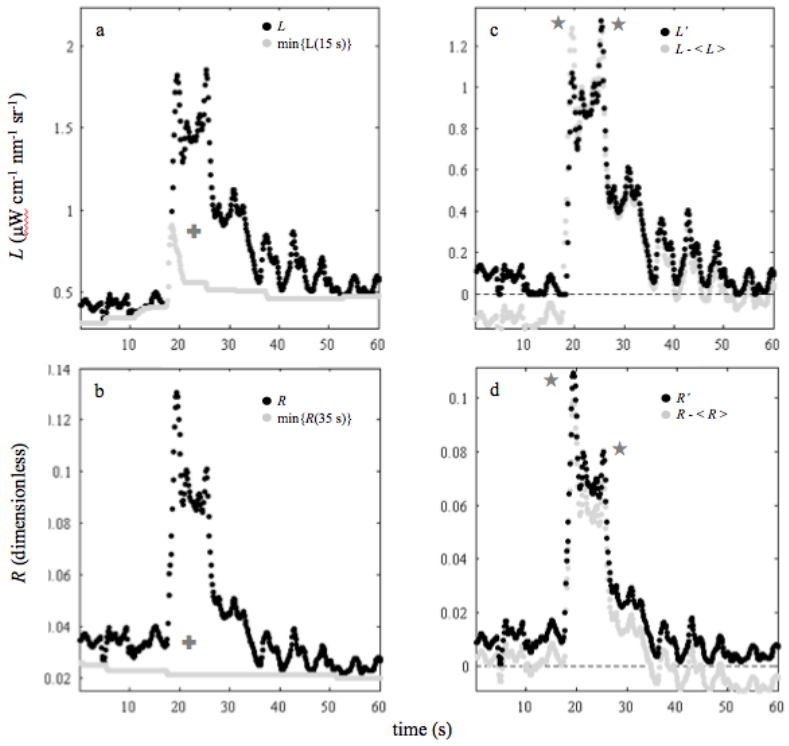

Figure 8: (a) When applied to a 35 s whitecap feature in *L'* following Path 1 (black circles), the running minmax filter with a 15 s window size produced a baseline (grey circles) that included a portion of the whitecap (grey plus), since local minima occur within the event itself. (b) A 35 s window size applied to the *R* signal resulted a baseline that did not erroneously include a portion of the whitecap feature (grey plus). (c, d) The moving minimum approach offered only an approximation of the ambient illumination conditions (unlike the E_d measurement used in the calculation of *R'*), therefore the shapes of the *L'* and *R'* signals were similar but not identical (examples indicated with stars).

Observations in the L_t' or *R'* record greater than the defined magnitude threshold were identified as whitecap candidates (Figure 9, +s). The extent of the IQR (the 25th to 75th percentiles identified by the extent of the boxes in Fig. 9b) was determined by the intensity of surface reflected skylight (L_r), dependent on the solar zenith angle, viewing geometry, the wavy surface and the sky conditions, and presented as low magnitude, high frequency variance distributed nearly equally across the length of the record (Figure 10, a). The lower detection limit for whitecap samples in *L'* or *R'* is dependent on the

magnitude of L_r. When L_r is large, the lowest magnitude features of the whitecap (*e.g.*, the mature bubble plume) become indiscernible from the background. The remaining non-whitecap, transient bright features (included as whitecap candidates after applying the magnitude threshold) were removed from the signal using a de-spiking procedure based on event duration. Bright, glint-like features lasting < 2 s (14 samples) in length (easily identified in an *L'* record which contains no whitecaps) were eliminated from the pool of whitecap candidates (Figure 10, b).

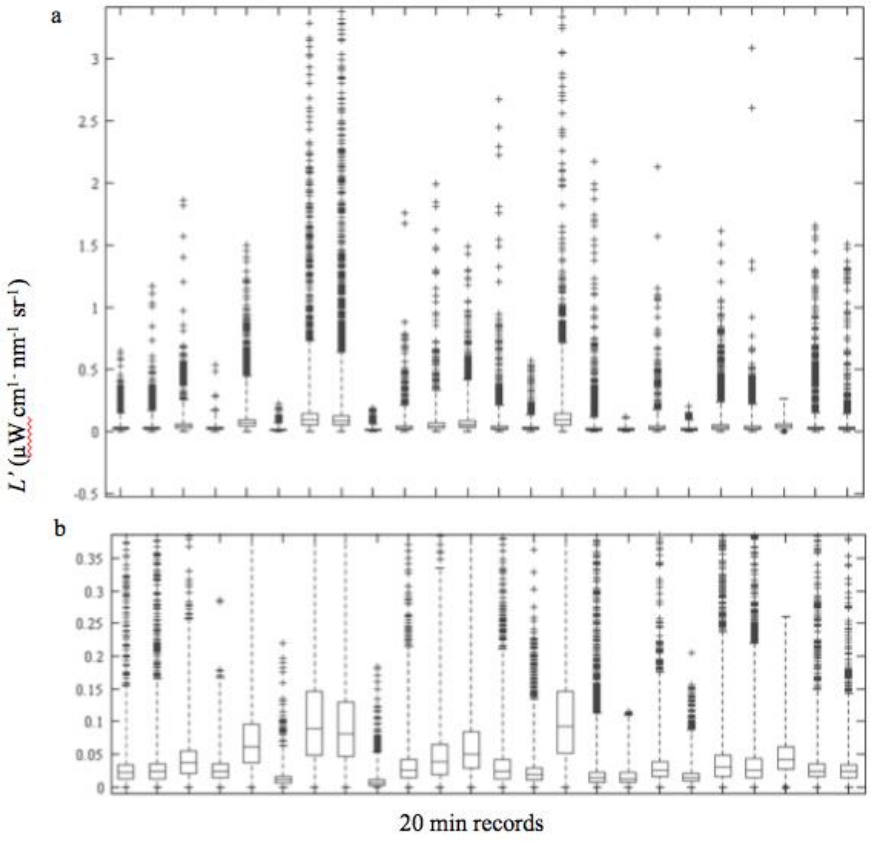

Figure 9: (a) Boxplot of *L'* data and (b) an enlargement of the boxes showing the interquartile range (IQR), where the top and bottom of the box represents the 25th and 75 percentiles of *L'* and the center of the box is the median. Whiskers are drawn to 2(IQR) and outliers (indicated by +s) are candidate whitecap samples. The quantity and magnitude of the outliers indicate the frequency and intensity of whitecaps.

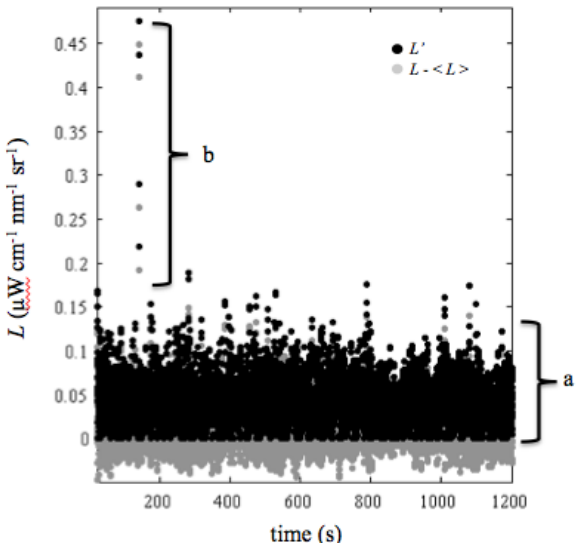

Figure 10: The detrended (grey circles) total upwelling radiance (L_t) and baseline removed L_t (L') signals for a low wind speed day (Day 94, U_{10}~5.66 m s^{-1}) with no whitecaps. (a) Most of the variance in the L' signal is attributable to reflected skylight (L_r) (b) A bright feature in the L' signal exceeds the magnitude threshold requirement identifying whitecaps, but is removed from the pool of whitecap candidates in the duration filter.

The resulting L'_W and R'_W records were used to calculate a selection of whitecap metrics. For events including Stages A and B of the whitecap, metrics describing individual events can be estimated. Decay and intensity metrics were calculated for whitecap events with duration and maximum radiance values above the 75th percentile for the record. For example, *e-folding* time and breaking intensity, were estimated for short (~12 s) and long (~30 s) breaking events measured during high wind speed (14 m s^{-1}) conditions (Figure 11). An exponential fit to the binned R'_W data produced an *e-folding* time of ~4 s for both events. An example of a decay rate retrieval from binned L'_W data for a single, short (~12 s) event can be found in Figure 14c. The lower magnitude (R'_{Wmax}~0.36), but longer lasting, breaking event produced an intensity metric of 3.5, while the higher magnitude (R'_{Wmax}~0.66) short-lived event had an

intensity of 2.2. The average reflectivities (*e.g.*, approximate albedo) of these breaking events were 20% (σ^2=0.16) and 11% (σ^2=0.08) respectively. The maximum whitecap albedo (LER) for the record (U_{10N} ~ 9 to 15 m s^{-1}) was 68%. On average, whitecap albedo ranged from 13% to 27%.

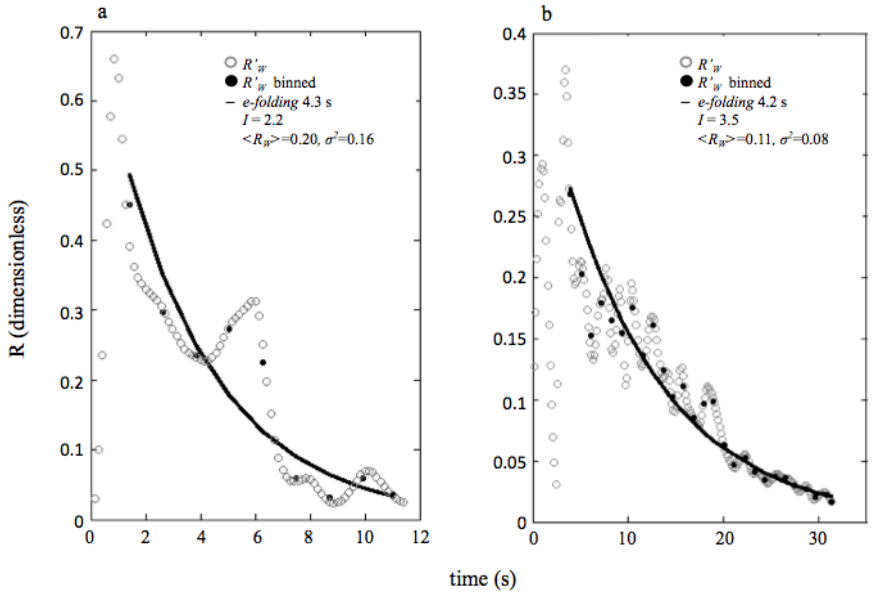

Figure 11: (a) An exponential fit to the binned R'_W data from a short (~12 s) breaking event measured during high wind speed conditions (14 m s^{-1}) produced an *e-folding* time of 4.3 s, an intensity (*I*) of 2.2, and an average reflectivity of 0.20 (σ^2=0.16). (b) The lower magnitude (R'_{Wmax}~0.36) but longer lasting (~30 s) breaking event produced an *e-folding* time of 4.2 s, an intensity metric of 3.5 and an average reflectivity of 0.11 (σ^2=0.08).

Whitecap retrievals in the L'_W and R'_W records were also used to calculate fractional whitecap coverage. Substantial scatter exists in the relationship between wind speed and fractional whitecap coverage, primarily because the extent of the sea surface covered by whitecaps at any given time is dependent on many additional factors (*e.g.*, marine atmospheric boundary layer stability, wind duration, fetch, sea state, etc.) (*e.g.*, Ross and Cardone [1974], Monahan and Monahan [1986], Bortkovskii and Novak [1993], Hanson and Phillips [1999], Zhao and Toba [2001], Stramska and Petelski [2003], and Woolf [2005]), but

also because of uncertainty in *W* due to undersampling [*Callaghan and White*, 2009]. Coverage estimates were produced using 5, 10, 20 and 30-minute segment lengths for stations experiencing different physical forcing conditions (Table 1; Figure 12). The number of samples included in each coverage estimate from the point-based radiometric approach is somewhat analogous to the number of images analyzed per *W* estimate using digital imaging.

Surface drift velocities estimated using atmospheric friction velocities measured in the Southern Ocean were $O(10^{-1})$ m s^{-1} (see Section 3.2.2.). For an IFOV of ~1.5 m and an average drift velocity of 0.3 m s^{-1} (*i.e.* wind friction velocity ~0.56 m s^{-1}) under 12 m s^{-1} wind speed conditions, a record length of 20 minutes produces an equivalent area of ~1.74 km^2. The predicted fractional whitecap coverage under these conditions is ~0.023. To test whether the record length is long enough to provide a good statistical sample, the number of independent events was estimated the area of individual whitecaps (0.75 to 2 m^2) from Bondur and Sharkov [1982a]. For a 12 m s^{-1} wind speed and an individual whitecap area of 1.5 m, the number of predicted events is 26. Under similar conditions in the Southern Ocean (*i.e.*, day 76), the radiometric method captured 8 to 13 independent events, ~29 to 50% of the total number of predicted events. If the area of the individual whitecaps increases, as would be expected with an increase in forcing, the number of predicted events decreases (*e.g.*, for a_{wc} = 2 m^2, N=16) and the capture rate for the radiometric method increases (*e.g.*, 53 to 81% of the predicted events).

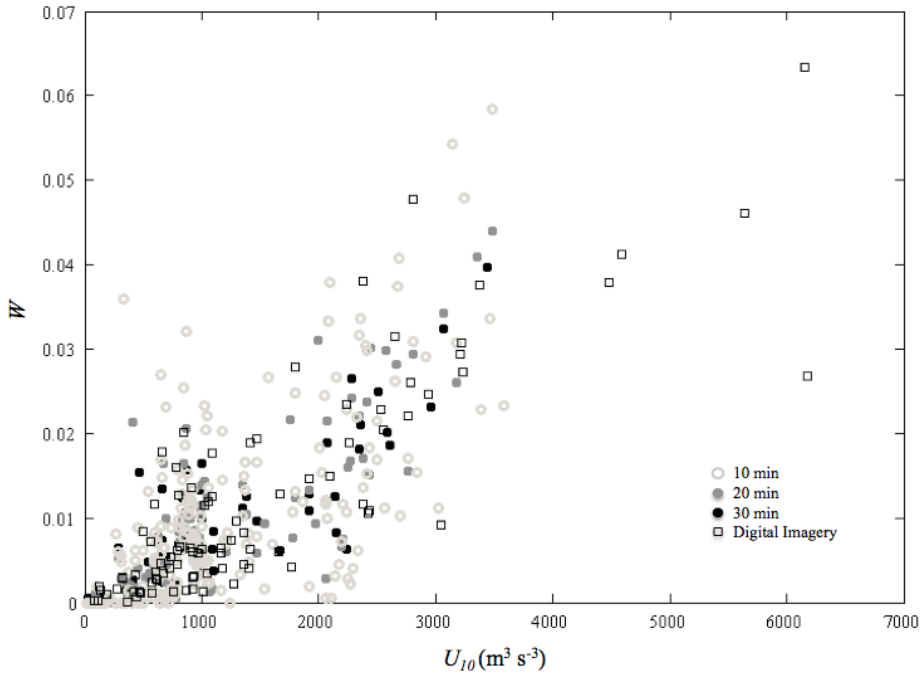

Figure 12: Whitecap coverage retrieval as a function of cubic wind speed using 10 (open circles), 20 (grey circles) and 30 (black circles) minute record lengths based on a 4(IQR) threshold for direct comparison to the 20-minute fractional whitecap coverage estimates retrieved using digital imagery.

During SO GasEx, 94 20-minute records were used in the Path 1 radiometric method to produce whitecap coverage estimates ranging from 1.2×10^{-4} to 0.076 (Figure 13, black circles, black errorbars). Nearly all (87%) of the radiometric coverage estimates were collected within 4 hours of those retrieved using digital imagery (Figure 13, grey circles, grey errorbars). The standard error metric in Figure 13 gives an indication of the spread in the whitecap coverage estimates retrieved each day (over a 1-4 hour period). The number of whitecap estimates produced by the radiometric and digital imaging techniques are not uniform across days (n~1-8).

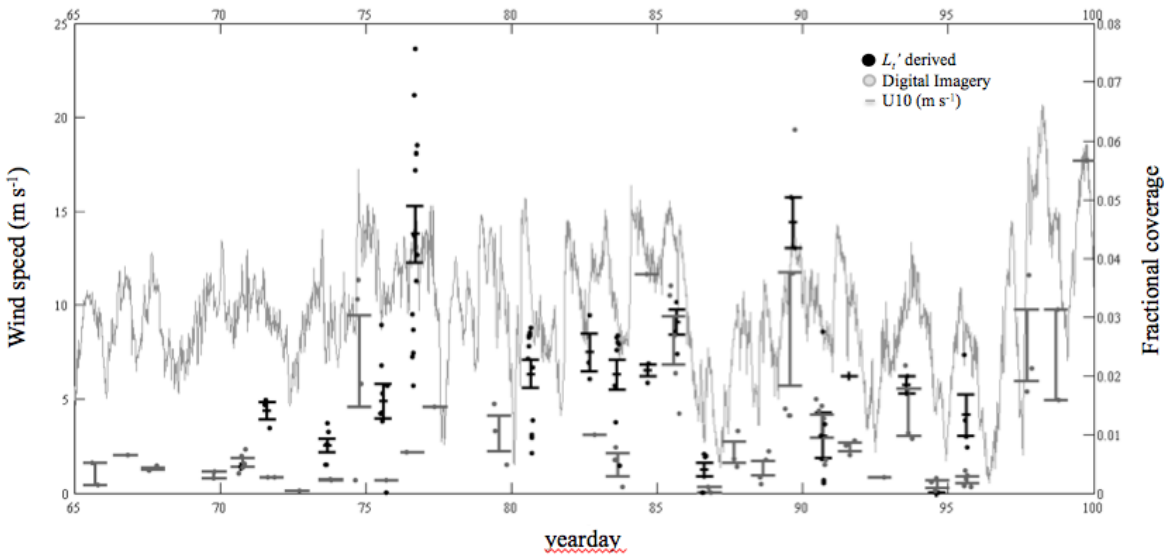

Figure 13: The wind speed record from SO GasEx (grey line) and the 94 fractional whitecap coverage retrievals using the Path 1 radiometric approach (black circles) with the standard error calculated for the data collected on each day ($1 \leq n \leq 8$) and the 80 whitecap coverage estimates retrieved using the digital imaging approach (grey circles) and the standard error for each day ($1 \leq n \leq 6$).

The large changes in whitecap coverage over short time scales made the direct comparison between coverage retrievals collected using the different techniques challenging. For example, 160 minutes of radiometric data were collected on yearday 76, resulting in eight coverage estimates (Figure 14a, b). Over a two-hour period during increasing wind forcing (Figure 15, blue line), a four-fold increase in whitecap coverage, from 0.018 to 0.076, resulted (Figure 15, black circles, black line). Four hours earlier on day 76, a fractional coverage of 0.0069 was estimated using digital imagery, an 89% difference relative to the nearest radiometrically derived coverage (Figure 15, black square). All radiometric data and digital imagery were collected with a host of meteorological measurements and proximal in time to one another. Because most of the coverage estimates retrieved using the two techniques were not within the same 20-minute interval, the whitecap coverage results were compared using the wind speed-whitecap relationship (Figure 16).

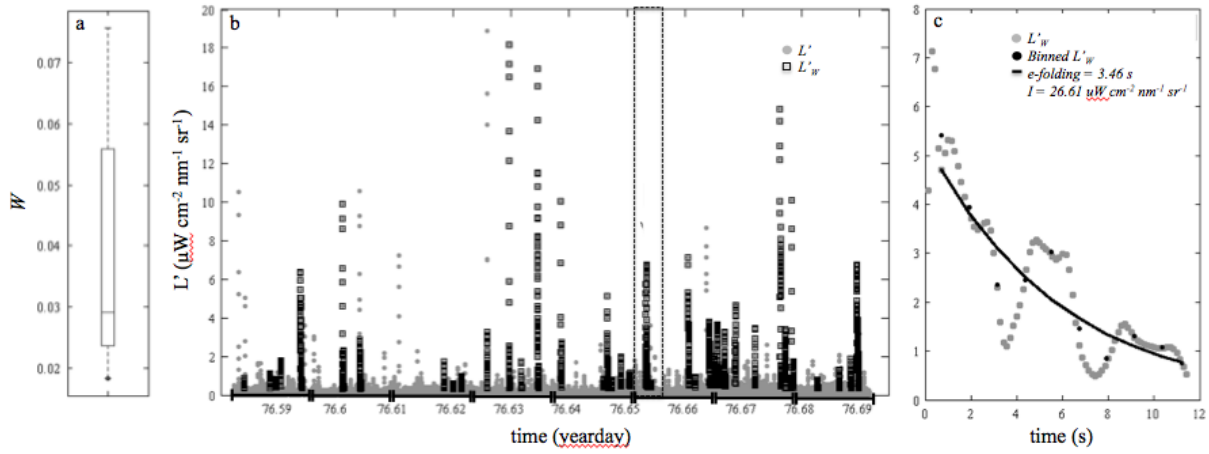

Figure 14: (a) Whitecap coverage estimates determined from (b) whitecap samples (black squares) identified in eight 20-minute records (black lines along the x-axis differentiate the eight segments) of *L'* from Day 76 (grey circles) following Path 1. Duration, decay rate and intensity metrics were determined for each event (black squares in b). (c) An example of a decay rate retrieval from binned L'_W data (black circles) for a single event (dashed box in b) yielded an e-folding time of ~3.5 s for an event lasting 12 s in duration.

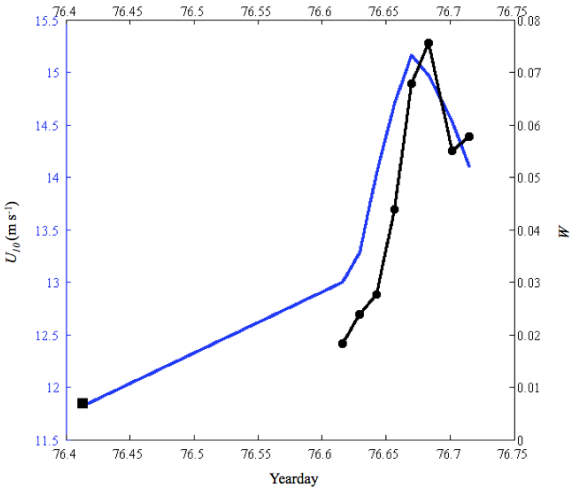

Figure 15: The wind speed record for yearday 76 (blue line, left y-axis) and the eight fractional whitecap

coverage estimates using the Path 1 radiometric approach (from Figure 13) (black line, black circles; right y-axis) and digital imagery (black square).

Coverage estimates retrieved using the radiometric (black lines, black points with standard error) and digital imaging (grey lines, grey points with standard error) techniques were compared by binning the data according to the neutral wind speed at 10 m (U_{10N}) in 2 m s^{-1} increments (Table 1; Figure 16a). Although U_{10} has been used to examine the wind-speed whitecap relationship in previously published research, here, in order to account for atmospheric stability, U_{10N} was used. For winds speeds < 6 m s^{-1}, there was no statistically significant difference whitecap coverages estimated using the two techniques, however whitecaps are rarely seen under these wind conditions. For wind speeds $\geq$ 6 m s^{-1}, the radiometric approach (Paths 1 & 2) produced coverage estimates that were consistently statistically significantly higher ($\alpha = 0.05$) than the digital image analysis ($0 \leq p\text{-value} \leq 0.024$), perhaps because it captures more of the whitecap feature, including the mature bubble plume. The difference between the coverage estimates was minimized when the magnitude threshold was increased from 2 to 4(IQR) to capture only the brightest features corresponding to Stage A whitecaps (Figure 16b). The use of a higher threshold with the radiometric data resulted in the retrieval of strictly the foam features, similar to retrievals using the digital imaging technique, which successfully differentiates the foam feature from the background, but does not see the bubble plume (Figure 17).

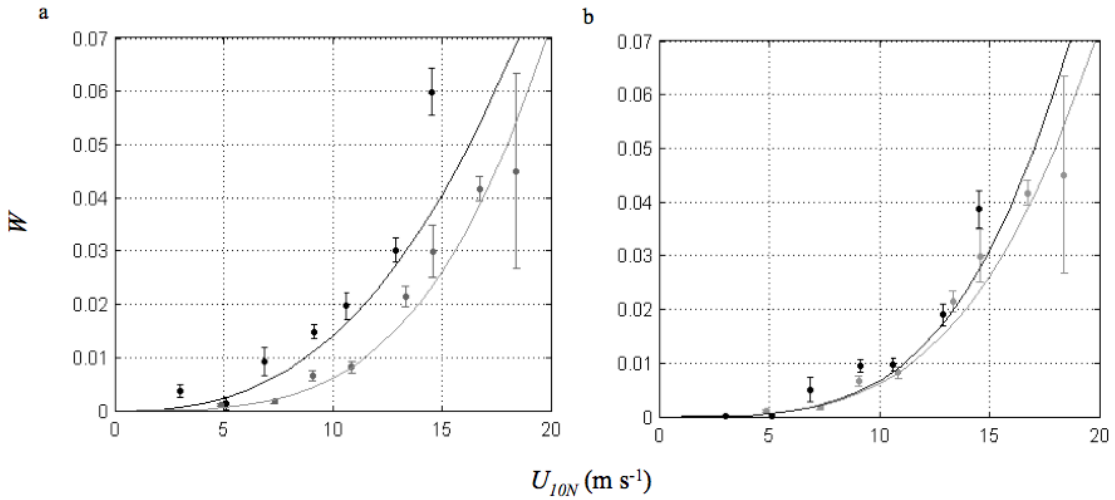

Figure 16: Whitecap coverage estimated using the radiometric (Path 1, black circles) and digital imaging (grey circles) techniques were binned according to neutral wind speeds in 2 m s^{-1} increments (*e.g.*, 4-6 m s^{-1}, 6-8 m s^{-1}, etc.). The mean whitecap coverage for each technique and wind speed increment were compared using a [left-tailed] t-test under the assumption of unequal variances. (a) The radiometric approach produced coverage estimates that were consistently statistically significantly higher than the digital imaging approach for $U_{10} \geq 6$ m s^{-1}. (b) The use of a 4(IQR) magnitude threshold, which included only the bright foam features in the estimation of *W*, minimized the difference between whitecap coverage estimates using the two techniques.

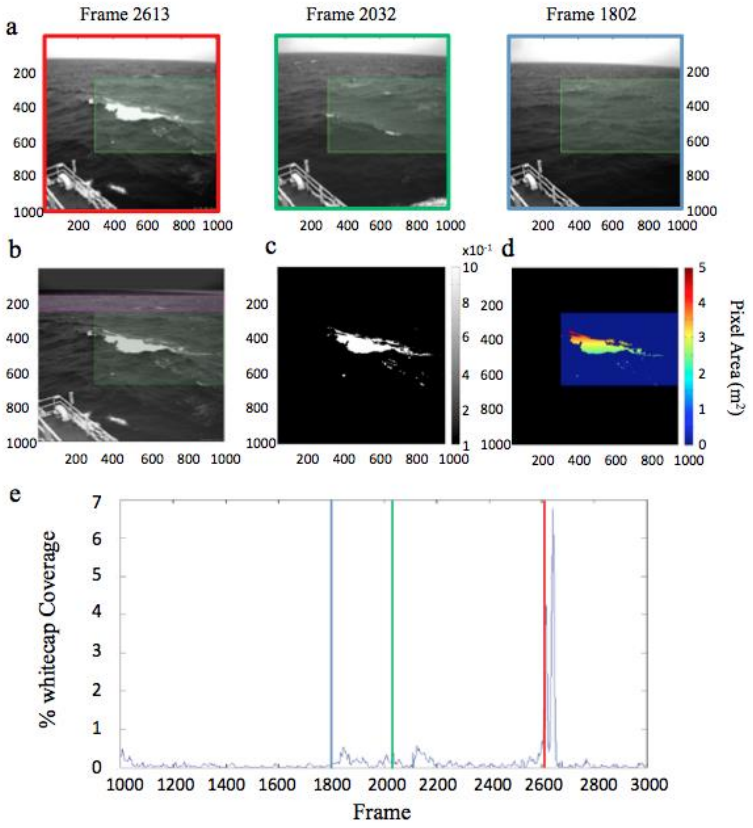

Figure 17: (a) High resolution digital imagery of whitecaps in the Southern Ocean collected using Imperx video cameras sampling 100 m^2 at 5 Hz [*Zappa et al.*, 2012]. The Background intensity gradients (*e.g.*, panel b) were removed (*e.g.*, panel c) and a threshold was applied to identify pixels containing foam. (e) Whitecap coverage was estimated using the whitecap pixel area (*e.g.*, panel d) for the three frames in panel (a) following the approach of Callaghan and White [2009].

The optimal fit of the radiometrically estimated whitecap coverage (Path 1) to the neutral windspeed at 10 m was determined using ordinary least squares (condition number O[10^1]). Whitecap coverage showed a near cubic dependence on wind speed (Figure 16a, black line) when the 2(IQR) threshold was used to capture the full whitecap feature. When the difference between whitecap coverage measured radiometrically (Figure 16b, black line) and using the digital imaging technique (Figure 16b, grey line) is

minimized (*i.e.*, 4[IQR), whitecap coverage showed a dependence on wind speed that is to the ~4th power and includes 88% of the total whitecap feature retrieved using the 2(IQR) threshold.

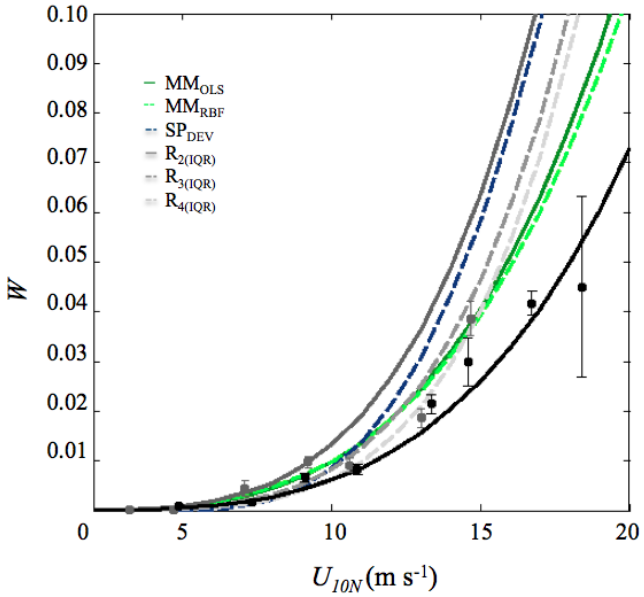

Figure 18: The relationship between wind speed (U_{10N}) and whitecap coverage (W) retrieved using the radiometric method was estimated using ordinary least squares (dark grey line). Other wind speed-whitecap parameterizations (based on the instantaneous wind speed at 10 m), including the Monahan and O'Muircheartaigh [1980] ordinary least squares (MM_{OLS}) and robust biweight fitting (MM_{RBF}) paramerizations (green lines) and the Stramska and Petelski [2003] parameterization for developed seas (blue line) are shown for comparison. The relationship between the neutral windspeed at 10 m (U_{10N}) and whitecap coverage relationships for 3(IQR) (medium grey line) and 4(IQR) (light grey line, grey points with standard error) and retrieved using digital imagery (black line and points with standard error) are also presented.

Previously published, widely recognized wind speed-whitecap relationships, including the Monahan & O'Muircheartaigh [1980] parameterizations using ordinary least squares (MM_{OLS}; Figure 18, dark green line) and robust bi-weight fitting (MM_{RBF}; Figure 18, light green line) and the Stramska and Petelski

[2003] (Figure 18, blue line) parameterization for developed seas (most appropriate for the SO GasEx dataset, see Table 1) are included for comparison. Increasing the magnitude threshold to 3(IQR) (Figure 18; medium grey dashed line) produced a wind speed-whitecap relationship most comparable to the widely used Monahan and O'Muircheartaigh [1980] parameterizations, particularly for wind speeds < 15 m s^{-1}, and includes 92% of the whitecap feature captured by 2(IQR). Further increasing the magnitude threshold to 4(IQR) (Figure 18, light grey dashed line) included 88% of the total whitecap feature retrieved using the 2(IQR) threshold.

The radiometric approach is conservative in its design to minimize the risk of producing false positive errors in the estimates of whitecap metrics. As a result, the high magnitude threshold (*i.e.* 2[IQR]) and the added duration filter (*i.e.* > 2 s) could result in the exclusion of the final portion of the mature or decaying bubble plume and of any foam streak or spume line features present. Also, certain environmental conditions result in the loss of some whitecap features or preclude the use of the radiometric method altogether. Surface reflected skylight determines the detection limit for whitecaps. When L_r is large, the darker, lower magnitude whitecap features (*i.e.*, the mature bubble plume) cannot be differentiated from surface reflected skylight and are not included as a whitecap retrieval in either the Path 1 or 2 approach. Although not seen here, strong trends in downwelling irradiance that are not effectively captured following Path 1 could, in extreme cases, result in false positive whitecap identification. Under such conditions, the Path 2 approach is recommended. The radiometric technique is not recommended for use under erratic downwelling irradiance conditions (*i.e.*, spikey E_d signal) when the E_d sensor is not gimbaled. Under such conditions, the Path 1 approach would not effectively capture the changing illumination conditions in the baseline estimation, producing false-positive whitecap identifications. Similarly, the filtering necessary to correct the downwelling irradiance data for ship motion using the Path 2 approach (*i.e.*, moving average with a window size based on the period of the swell) will not preserve fleeting spikes in E_d, resulting in erroneous R' values.

3.6. Conclusions

The methodology for retrieving whitecap statistics described here is simple, automated and robust, using radiometers mounted on a ship or mooring. The nature of the measurement allows more of the decaying whitecap feature, the surface manifestation of the gamma plume following Monahan and Lu [1990], to be retrieved than the traditional digital imaging approach. Capturing the mature portion of the whitecap (*i.e.*, bubble plume) has implications for gas transfer, specifically for lower solubility gases (*e.g.*, Woolf and Thorpe [1991]), and the production of primary marine sea salt aerosols (*e.g.*, Monahan *et al.* [1986]). When only the bright, foam features are included in the radiometric estimation of W (*e.g.*, 4[IQR] threshold), strong agreement was found with coverage measured concurrently using digital imagery collected in the Southern Ocean. When the tail-end of the bubble feature is excluded from the whitecap coverage estimate (*e.g.*, 3[IQR] threshold), strong agreement can be found between the radiometrically derived and previously published wind speed-whitecap parameterizations (*e.g.*, Monahan and O'Muircheartaigh [1980]).

References

Andreas, E. L., J. B. Edson, E. C. Monahan, M. P. Rouault, and S. D. Smith (1995), The spray contribution to net evaporation from the sea: A review of recent progress, *Boundary-Layer Meteorology*, *72*(1-2), 3–52.

Arrigo, K. R., D. Worthen, A. Schnell, and M. P. Lizotte (1998), Primary production in Southern Ocean waters, *J. Geophys. Res.*, *103*(C8), 15587–15600, doi:10.1029/98JC00930.

Asher, W., J. Edson, W. Mcgillis, R. Wanninkhof, D. T. Ho, and T. Litchendor (2002), Fractional Area Whitecap Coverage and Air-Sea Gas Transfer Velocities Measured During GasEx-98, in *Gas Transfer at Water Surfaces*, pp. 199–203, American Geophysical Union.

Austin, R. (1974), Inherent spectral radiance signatures of the ocean surface, *Ocean color analysis*, *7410*, 1–20.

Bailey, S. W. (2009), *Whitecap Reflectance*, NASA Ocean Biology Processing Group.

Balch, W. M., K. A. Kilpatrick, and C. C. Trees (1996), The 1991 coccolithophore bloom in the central North Atlantic. 1. Optical properties and factors affecting their distribution, *Limnol. Oceanogr.*, *41*(8), 1669–1683, doi:10.4319/lo.1996.41.8.1669.

Balch, W. M., D. T. Drapeau, T. L. Cucci, R. D. Vaillancourt, K. A. Kilpatrick, and J. J. Fritz (1999), Optical backscattering by calcifying algae: Separating the contribution of particulate inorganic and organic carbon fractions, *Journal of Geophysical Research: Oceans (1978–2012)*, *104*(C1), 1541–1558.

Balch, W. M., H. R. Gordon, B. C. Bowler, D. T. Drapeau, and E. S. Booth (2005), Calcium carbonate measurements in the surface global ocean based on Moderate-Resolution Imaging Spectroradiometer data, *J. Geophys. Res.*, *110*(C7), C07001, doi:10.1029/2004JC002560.

Balch, W. M., D. T. Drapeau, B. C. Bowler, E. Lyczskowski, E. S. Booth, and D. Alley (2011), The contribution of coccolithophores to the optical and inorganic carbon budgets during the Southern Ocean Gas Exchange Experiment: New evidence in support of the "Great Calcite Belt" hypothesis, *J. Geophys. Res.*, *116*, C00F06, doi:10.1029/2011JC006941.

Behrenfeld, M. J., and P. G. Falkowski (1997), Photosynthetic rates derived from satellite-based chlorophyll concentration, *Limnology and oceanography*, *42*(1), 1–20.

Bondur, V., and E. Sharkov (1982a), Statistical Characteristics of foam formations on a disturbed sea-surface, *Okeanologiya*, *22*(3), 372–379.

Bondur, V. G., and E. A. Sharkov (1982b), Statistical properties of whitecaps on a rough sea, *Oceanology*, *22*(3), 274–279.

Bortkovskii, R., and V. Novak (1993), Statistical dependencies of sea state characteristics on water temperature and wind-wave age, *Journal of marine systems*, *4*(2), 161–169.

Bortkovskii, R. S. (1987), *Air-sea exchange of heat and moisture during storms*, Kluwer Boston Inc., Hingham, MA.

Bouguet, J.-Y. (2004), *Camera calibration toolbox for matlab*, MRL - Intel Corp.

Briggs, N., M. J. Perry, I. Cetinić, C. Lee, E. D'Asaro, A. M. Gray, and E. Rehm (2011), High-resolution observations of aggregate flux during a sub-polar North Atlantic spring bloom, *Deep Sea Research Part I: Oceanographic Research Papers*, *58*(10), 1031–1039.

Brown, O. B., and H. R. Gordon (1973), Two component Mie scattering models of Sargasso Sea particles, *Applied optics*, *12*(10), 2461–2465.

Callaghan, A. H. (2013), An improved whitecap timescale for sea spray aerosol production flux modeling using the discrete whitecap method, *J. Geophys. Res. Atmos.*, *118*(17), 9997–10,010, doi:10.1002/jgrd.50768.

Callaghan, A. H., and M. White (2009), Automated processing of sea surface images for the determination of whitecap coverage, *Journal of Atmospheric and Oceanic Technology*, *26*(2), 383–394.

Carder, K., and R. Steward (1985), A remote-sensing reflectance model of a red-tide dinoflagellate off west Florida1, *Limnology and Oceanography*, *30*(2), 286–298.

Cifuentes-Lorenzen, A., J. B. Edson, C. J. Zappa, and L. Bariteau (2013), A Multisensor Comparison of Ocean Wave Frequency Spectra from a Research Vessel during the Southern Ocean Gas Exchange Experiment, *J. Atmos. Oceanic Technol.*, doi:10.1175/JTECH-D-12-00181.1.

Dierssen, H. M. (2010), Perspectives on empirical approaches for ocean color remote sensing of chlorophyll in a changing climate, *Proceedings of the National Academy of Sciences*, *107*(40), 17073–17078.

Dierssen, H. M., and R. C. Smith (2000), Bio-optical properties and remote sensing ocean color algorithms for Antarctic Peninsula waters, *J. Geophys. Res.*, *105*(C11), 26301–26312, doi:10.1029/1999JC000296.

Dierssen, H. M., R. C. Smith, and M. Vernet (2002), Glacial meltwater dynamics in coastal waters west of the Antarctic peninsula, *Proceedings of the National Academy of Sciences*, *99*(4), 1790–1795.

Donelan, M., M. S. LONGUET-HIGGINS, and J. S. TURNER (1972), Periodicity in Whitecaps, *Nature*, *239*(5373), 449–451, doi:10.1038/239449a0.

Fairall, C. W., E. F. Bradley, J. E. Hare, A. A. Grachev, and J. B. Edson (2003), Bulk Parameterization of Air–Sea Fluxes: Updates and Verification for the COARE Algorithm, *J. Climate*, *16*(4), 571–591, doi:10.1175/1520-0442(2003)016<0571:BPOASF>2.0.CO;2.

Flatau, P. J., M. Flatau, J. R. V. Zaneveld, and C. D. Mobley (2000), Remote sensing of bubble clouds in sea water, *Q.J.R. Meteorol. Soc.*, *126*(568), 2511–2523, doi:10.1002/qj.49712656808.

Franz, B. A. (2015), *Algorithm for Retrieval of Remote Sensing Relectance from Satellite Ocean Color Sensors*, NASA Ocean Biology Processing Group.

Frouin, R., M. Schwindling, and P.-Y. Deschamps (1996), Spectral reflectance of sea foam in the visible and near-infrared: In situ measurements and remote sensing implications, *J. Geophys. Res.*, *101*(C6), 14361–14371, doi:10.1029/96JC00629.

Goddijn-Murphy, L., D. K. Woolf, and A. H. Callaghan (2011), Parameterizations and algorithms for oceanic whitecap coverage, *Journal of Physical Oceanography*, *41*(4), 742–756.

Gordon, H. R. (1997), Atmospheric correction of ocean color imagery in the Earth Observing System era, *J. Geophys. Res.*, *102*(D14), 17081–17106, doi:10.1029/96JD02443.

Gordon, H. R., and M. Wang (1994), Influence of oceanic whitecaps on atmospheric correction of ocean-color sensors, *Applied Optics*, *33*(33), 7754–7763.

Hanson, J. L., and O. M. Phillips (1999), Wind Sea Growth and Dissipation in the Open Ocean, *J. Phys. Oceanogr.*, *29*(8), 1633–1648, doi:10.1175/1520-0485(1999)029<1633:WSGADI>2.0.CO;2.

Ho, D. T., C. L. Sabine, D. Hebert, D. S. Ullman, R. Wanninkhof, R. C. Hamme, P. G. Strutton, B. Hales, J. B. Edson, and B. R. Hargreaves (2011), Southern Ocean Gas Exchange Experiment: Setting the stage, *J. Geophys. Res.*, *116*, C00F08, doi:10.1029/2010JC006852.

Hooker, S. B., L. Van Heukelem, C. S. Thomas, H. Claustre, J. Ras, R. Barlow, H. Sessions, L. Schlüter, J. Perl, and C. Trees (2005), *Second SeaWiFS HPLC Analysis Round-robin Experiment (SeaHARRE-2)*, National Aeronautics and Space Administration, Goddard Space Flight Center.

Johnson, B. D., and R. C. Cooke (1980), Organic Particle and Aggregate Formation Resulting from the Dissolution of Bubbles in Seawater, *Limnology and Oceanography*, *25*(4), 653–661.

Johnson, B. D., and R. C. Cooke (1981), Generation of Stabilized Microbubbles in Seawater, *Science*, *213*(4504), 209 –211.

Jonasz, M., and G. Fournier (2011), *Light Scattering by Particles in Water: Theoretical and Experimental Foundations: Theoretical and Experimental Foundations*, Academic Press.

Koepke, P. (1984), Effective reflectance of oceanic whitecaps, *Appl. Opt.*, *23*(11), 1816–1824.

Kokhanovsky, A. A. (2004), Spectral reflectance of whitecaps, *J. Geophys. Res.*, *109*(C5), C05021, doi:10.1029/2003JC002177.

Lance, V. P., P. G. Strutton, R. D. Vaillancourt, B. R. Hargreaves, J.-Z. Zhang, and J. Marra (Submitted), Primary productivity, new productivity and carbon export during two Southern Ocean Gas Exchange (SO GasEx) tracer experiments, *J. Geophys. Res.*

Lance, V. P., P. G. Strutton, R. D. Vaillancourt, B. R. Hargreaves, J.-Z. Zhang, and J. Marra (2012a), Primary productivity, new productivity, and their relation to carbon flux during two Southern Ocean Gas Exchange tracer experiments, *J. Geophys. Res.*, *117*(C4), C00F14, doi:10.1029/2011JC007687.

Lance, V. P., P. G. Strutton, R. D. Vaillancourt, B. R. Hargreaves, J.-Z. Zhang, and J. Marra (2012b), Primary productivity, new productivity, and their relation to carbon flux during two Southern Ocean Gas Exchange tracer experiments, *J. Geophys. Res.*, *117*(C4), C00F14, doi:10.1029/2011JC007687.

Lee, M. E., and M. R. Lewis (2003), A New Method for the Measurement of the Optical Volume Scattering Function in the Upper Ocean, *J. Atmos. Oceanic Technol.*, *20*(4), 563–571, doi:10.1175/1520-0426(2003)20<563:ANMFTM>2.0.CO;2.

Lee, Z., K. L. Carder, and R. A. Arnone (2002), Deriving Inherent Optical Properties from Water Color: a Multiband Quasi-Analytical Algorithm for Optically Deep Waters, *Appl. Opt.*, *41*(27), 5755–5772.

Lee, Z., Y.-H. Ahn, C. Mobley, and R. Arnone (2010), Removal of surface-reflected light for the measurement of remote-sensing reflectance from an above-surface platform, *Optics Express*, *18*(25), 26313–26324.

Lee, Z., V. P. Lance, S. Shang, R. Vaillancourt, S. Freeman, B. Lubac, B. R. Hargreaves, C. Del Castillo, R. Miller, and M. Twardowski (2011), An assessment of optical properties and primary production derived from remote sensing in the Southern Ocean (SO GasEx), *Journal of Geophysical Research: Oceans (1978–2012)*, *116*(C4).

Lemire, D. (2006), Streaming maximum-minimum filter using no more than three comparisons per element, *arXiv preprint cs/0610046*.

Liss, P. S., and L. Merlivat (1986), Air-sea gas exchange rates: introduction and synthesis, in *The Role of Air-Sea Exchange in Geochemical Cycling*, edited by P. Buat-Menard, pp. 113–129, Reidel, Washington.

Longhurst, A., S. Sathyendranath, T. Platt, and C. Caverhill (1995), An estimate of global primary production in the ocean from satellite radiometer data, *Journal of Plankton Research*, *17*(6), 1245–1271.

Maritorena, S., D. A. Siegel, and A. R. Peterson (2002), Optimization of a semianalytical ocean color model for global-scale applications, *Appl. Opt.*, *41*(15), 2705–2714.

Miller, R. L., M. Belz, C. Del Castillo, and R. Trzaska (2002), Determining CDOM absorption spectra in diverse coastal environments using a multiple pathlength, liquid core waveguide system, *Continental Shelf Research*, *22*(9), 1301–1310.

Mitchell, B. G., and O. Holm-Hansen (1991), Observations of modeling of the Antartic phytoplankton crop in relation to mixing depth, *Deep Sea Research Part A. Oceanographic Research Papers*, *38*(8), 981–1007.

Mobley, C. D. (1994), *Light and Water*, Academic Press, San Diego, CA.

Monahan, E. (1993), Occurrence and Evolution of Acoustically Relevant Sub-Surface Bubble Plumes and their Associated, Remotely Monitorable, Surface Whitecaps, in *Natural Physical Sources of Underwater Sound*, edited by B. R. Kerman, pp. 503–517, Springer Netherlands.

Monahan, E. C. (1989), From the laboratory tank to the global ocean, *The climate and health implications of bubble-mediated sea-air exchange*, 43–63.

Monahan, E. C., and H. G. Dam (2001), Bubbles: An estimate of their role in the global oceanic flux of carbon, *J. Geophys. Res.*, *106*(C5), 9377–9383, doi:10.1029/2000JC000295.

Monahan, E. C., and M. Lu (1990), Acoustically relevant bubble assemblages and their dependence on meteorological parameters, *Oceanic Engineering, IEEE Journal of*, *15*(4), 340–349, doi:10.1109/48.103530.

Monahan, E. C., and C. F. Monahan (1986), The Influence of Fetch on Whitecap Coverage as Deduced from the Alte Weser Lightstation Observer's Log, in *Oceanic Whitecaps*, vol. 2, edited by E. Monahan and G. Niocaill, pp. 275–277, Springer Netherlands.

Monahan, E. C., and I. Muircheartaigh (1980), Optimal Power-Law Description of Oceanic Whitecap Coverage Dependence on Wind Speed, *J. Phys. Oceanogr.*, *10*(12), 2094–2099, doi:10.1175/1520-0485(1980)010<2094:OPLDOO>2.0.CO;2.

Monahan, E. C., and M. C. Spillane (1984), The role of oceanic whitecaps in air sea gas exchange, in *Gas Transfer at Water Surfaces*, edited by W. Brutsaert and G. H. Jirka, pp. 495–504, D. Reidel, Norwell, MA.

Monahan, E. C., and D. K. Woolf (1989), Comments on "Variations of Whitecap Coverage with Wind stress and Water Temperature, *J. Phys. Oceanogr.*, *19*(5), 706–709, doi:10.1175/1520-0485(1989)019<0706:COOWCW>2.0.CO;2.

Monahan, E. C., and C. R. Zietlow (1969), Laboratory comparisons of fresh-water and salt-water whitecaps, *J. Geophys. Res.*, *74*(28), 6961–6966, doi:10.1029/JC074i028p06961.

Monahan, E. C., P. Bowyer, D. Doyle, M. Higgins, and D. K. Woolf (1984), *Whitecaps and the marine atmosphere*, University College Rep. 7, Galway, Ireland.

Monahan, E. C., D. E. Spiel, and K. L. Davidson (1986), A model of marine aerosol generation via whitecaps and wave disruption, in *Oceanic whitecaps*, pp. 167–174, Springer.

Moore, K. D., K. J. Voss, and H. R. Gordon (1998), Spectral Reflectance of Whitecaps: Instrumentation, Calibration, and Performance in Coastal Waters, *J. Atmos. Oceanic Technol.*, *15*(2), 496–509, doi:10.1175/1520-0426(1998)015<0496:SROWIC>2.0.CO;2.

Moore, K. D., K. J. Voss, and H. R. Gordon (2000), Spectral reflectance of whitecaps: Their contribution to water-leaving radiance, *J. Geophys. Res.*, *105*(C3), 6493–6499, doi:10.1029/1999JC900334.

Mueller, J. L. et al. (2003), Ocean optics protocols for satellite ocean color sensor validation, revision 4, volume III: Radiometric Measurements and Data Analysis Protocols, edited by J. L. Mueller, G. S. Fargion, and C. R. McClain, *NASA Tech. Memo*, 01674–0.

Mueller, J. L., G. S. Fargion, C. R. McClain, J. Mueller, S. Brown, D. Clark, B. Johnson, H. Yoon, K. Lykke, and S. Flora (2004), *Ocean Optics Protocols For Satellite Ocean Color Sensor*

Validation, Revision 5, Volume VI: Special Topics in Ocean Optics Protocols, Part 2, NASA Report 211621, 2003, 1-36.

Nordberg, W., J. Conaway, D. B. Ross, and T. Wilheit (1971), Measurements of microwave emission from a foam-covered, wind-driven sea, *Journal of the Atmospheric Sciences*, *28*(3), 429–435.

O'Reilly, J. E., S. Maritorena, D. A. Siegel, M. C. O'Brien, D. Toole, B. G. Mitchell, M. Kahru, F. P. Chavez, P. Strutton, and G. F. Cota (2000), Ocean color chlorophyll a algorithms for SeaWiFS, OC2, and OC4: Version 4, *SeaWiFS postlaunch calibration and validation analyses, Part*, *3*, 9–23.

Petzold, T. J. (1972), *Volume scattering functions for selected ocean waters*, DTIC Document.

Randolph, K., H. M. Dierssen, M. Twardowski, A. Cifuentes-Lorenzen, and C. J. Zappa (2014), Optical measurements of small deeply penetrating bubble populations generated by breaking waves in the Southern Ocean, *J. Geophys. Res. Oceans*, n/a–n/a, doi:10.1002/2013JC009227.

Reynolds, R. A., D. Stramski, and B. G. Mitchell (2001), A chlorophyll-dependent semianalytical reflectance model derived from field measurements of absorption and backscattering coefficients within the Southern Ocean, *Journal of Geophysical Research: Oceans (1978–2012)*, *106*(C4), 7125–7138.

Roesler, C. S., and E. Boss (2002), A novel relfectance inversion model: retrieval of beam attenuation coefficients and particle size ditributions from ocean color, Office of Naval Research, Santa Fe, NM.

Ross, D. B., and V. Cardone (1974), Observations of oceanic whitecaps and their relation to remote measurements of surface wind speed, *Journal of Geophysical Research*, *79*(3), 444–452.

Scanlon, B., and B. Ward (2013), Oceanic wave breaking coverage separation techniques for active and maturing whitecaps, *Methods in Oceanography*, *8*(0), 1–12, doi:10.1016/j.mio.2014.03.001.

Stabeno, P. J., and E. C. Monahan (1986), The influence of whitecaps on the albedo of the sea surface, in *Oceanic Whitecaps and Their Role in Air-Sea Exchange Processes*, edited by E. C. Monahan and G. Mac Niocaill, pp. 261–266, Dordrecht, Holland.

Stramska, M., and T. Petelski (2003), Observations of oceanic whitecaps in the north polar waters of the Atlantic, *J. Geophys. Res.*, *108*(C3), 3086, doi:10.1029/2002JC001321.

Stramski, D., and J. Tegowski (2001), Effects of intermittent entrainment of air bubbles by breaking wind waves on ocean reflectance and underwater light field, *J. Geophys. Res.*, *106*(C12), 31345–31360, doi:10.1029/2000JC000461.

Stramski, D., R. A. Reynolds, M. Kahru, and B. G. Mitchell (1999), Estimation of particulate organic carbon in the ocean from satellite remote sensing, *Science*, *285*(5425), 239–242.

Sugihara, Y., H. Tsumori, T. Ohga, H. Yoshioka, and S. Serizawa (2007), Variation of whitecap coverage with wave-field conditions, *Journal of Marine Systems*, *66*(1), 47–60.

Terrill, E. J., W. K. Melville, and D. Stramski (1998), Bubble entrainment by breaking waves and their effects on the inherent optical properties of the upper ocean.

Terrill, E. J., W. K. Melville, and D. Stramski (2001), Bubble entrainment by breaking waves and their influence on optical scattering in the upper ocean, *J. Geophys. Res.*, *106*(C8), 16815–16823, doi:10.1029/2000JC000496.

Thorpe, S. A. (1982), On the Clouds of Bubbles Formed by Breaking Wind-Waves in Deep Water, and their Role in Air -- Sea Gas Transfer, *Philosophical Transactions of the Royal Society of London. Series A, Mathematical and Physical Sciences*, *304*(1483), 155–210.

Twardowski, M., X. Zhang, S. Vagle, J. Sullivan, S. Freeman, H. Czerski, Y. You, L. Bi, and G. Kattawar (2012), The optical volume scattering function in a surf zone inverted to derive sediment and bubble particle subpopulations, *J. Geophys. Res.*, *117*(C7), C00H17, doi:10.1029/2011JC007347.

Wang, Q., E. Monahan, W. Asher, and P. Smith (1995), Correlations of whitecap coverage and gas transfer velocity with microwave brightness temperature for plunging and spilling breaking waves, *Air-Water Gas Transfer*, 217–225.

Welschmeyer, N. A. (1994), Fluorometric analysis of chlorophyll a in the presence of chlorophyll b and pheopigments, *Limnology and Oceanography*, *39*(8), 1985–1992.

Whitlock, C. H., D. S. Bartlett, and E. A. Gurganus (1982), Sea foam reflectance and influence on optimum wavelength for remote sensing of ocean aerosols, *Geophys. Res. Lett.*, *9*(6), 719–722, doi:10.1029/GL009i006p00719.

Woolf, D. K. (2005), Parametrization of gas transfer velocities and sea-state-dependent wave breaking, *Tellus B*, *57*(2), 87–94, doi:10.1111/j.1600-0889.2005.00139.x.

Woolf, D. K., and S. A. Thorpe (1991), Bubbles and the air-sea exchange of gases in near-saturation conditions, *Journal of Marine Research*, *49*(3), 435–466, doi:10.1357/002224091784995765.

Wright, S., S. Jeffrey, and R. Mantoura (2005), *Phytoplankton pigments in oceanography: guidelines to modern methods*, Unesco Pub.

Wu, J. (1983), Sea-Surface Drift Currents Induced by Wind and Waves, *J. Phys. Oceanogr.*, *13*(8), 1441–1451, doi:10.1175/1520-0485(1983)013<1441:SSDCIB>2.0.CO;2.

Yount, D. E. (1982), On the evolution, generation, and regeneration of gas cavitation nuclei, *The Journal of the Acoustical Society of America*, *71*(6), 1473–1481.

Zaneveld, J. R. V., and H. Pak (1973), Method for the determination of the index of refraction of particles suspended in the ocean, *JOSA*, *63*(3), 321–324.

Zappa, C. J., M. L. Banner, H. Schultz, J. R. Gemmrich, R. P. Morison, D. A. LeBel, and T. Dickey (2012), An overview of sea state conditions and air-sea fluxes during RaDyO, *Journal of Geophysical Research: Oceans (1978–2012)*, *117*(C7).

Zhang, X., Marlon Lewis, M. Lee, B. Johnson, and G. Korotaev (2002), The Volume Scattering Function of Natural Bubble Populations, *Limnology and Oceanography*, *47*(5), 1273–1282.

Zhang, X., M. Lewis, W. P. Bissett, B. Johnson, and D. Kohler (2004), Optical Influence of Ship Wakes, *Appl. Opt.*, *43*(15), 3122–3132, doi:10.1364/AO.43.003122.

Zhang, X., L. Hu, and M.-X. He (2009), Scattering by pure seawater: effect of salinity, *Optics Express*, *17*(7), 5698–5710.

Zhang, X., M. Twardowski, and M. Lewis (2011), Retrieving composition and sizes of oceanic particle subpopulations from the volume scattering function, *Appl. Opt.*, *50*(9), 1240–1259.

Zhao, D., and Y. Toba (2001), Dependence of whitecap coverage on wind and wind-wave properties, *Journal of oceanography*, *57*(5), 603–616.

4. Spectral reflectance of whitecaps and bubbles: impact on ocean color remote sensing

4.1. Background

In Chapter 3, the use of radiometric techniques for measuring whitecaps and bubbles from breaking waves in the Southern Ocean was evaluated. In addition to an enhancement in the magnitude of reflectance, whitecaps also show a marked influence on the spectral shape of reflectance. As a result, the presence of whitecaps produces error in the correction routines used to process ocean color imagery and therefore in the estimation of a host of ocean color derived biogeochemical parameters from space. This

is particularly true when applying semi-analytical models that incorporate the magnitude of the reflected light in addition to the spectral distribution (*i.e.* Lee *et al.* [2002]; Maritorena *et al.* [2002]; Roesler & Boss [2002]; Balch *et al.* [2005]). For example, the application of the two-band, semi-analytical ocean color algorithm for retrieving particulate inorganic carbon concentration (PIC) from above water reflectance measurements in the blue (443 nm) and green (555 nm) wavelengths generated estimates that were two to three times the PIC measured in the water column in the Southern Ocean [*Balch et al.*, 2011]. It was hypothesized that the presence of bubbles was the source of additional scattering that was misallocated as PIC. Although a full investigation on the effects of whitecaps on ocean color is beyond the scope of this dissertation, preliminary results from a dataset collected in the Southern Ocean identify ways in which to improve the current whitecap correction routine applied to ocean color imagery.

The current approach for quantifying whitecap reflectance for ocean color remote sensing estimates a fractional whitecap coverage based on wind speed and then assumes a fixed spectral reflectance associated with the whitecap [*Franz*, 2015]. Specifically, fractional whitecap coverage (W) is assumed to be empirically related to wind speed following Stramska and Petelski [2003]; to have a 22% effective reflectance following Koepke [1984]; and to have a near-infrared wavelength dependence following Frouin *et al.* [1996]. The effective reflectance term, the product of the reflectance of dense foam, 55% according to Whitlock *et al.* [1982] and Stabeno and Monahan [1986], and an efficiency factor of 0.4 ± 0.2, carries a high amount of uncertainty. It accounts for the average reflectance of an individual whitecap from the active, breaking phase (Stage A) through the quiescent or mature phase (Stage B), where spatial extent increases and reflectance decreases with age. The age distribution of whitecaps is assumed constant, thus the mean effective reflectance of an individual whitecap is used with the wind estimated fractional whitecap coverage to determine the area weighted whitecap reflectance, generally spanning an area of several pixels [*Koepke*, 1984; *Gordon and Wang*, 1994].

Large errors can occur from implementation of the whitecap correction routine, reportedly due to the wind speed-whitecap coverage relationship [*Bailey*, 2009]. This is particularly true for high latitude regions experiencing frequent strong winds and high void fractions [*Flatau et al.*, 2000]. Furthermore, the application of the Frouin *et al.* [1996] approach to include a spectral dependence in the near infrared can result in overestimation of whitecap reflectance in regions experiencing high wind speeds (>12 m s^{-1}) that result in negative normalized water leaving radiance retrievals [*Gordon and Wang*, 1994; *Gordon*, 1997]. To avoid this outcome, a single, fixed correction is applied to any regions experiencing wind speeds greater than 12 m s^{-1}. Reflectance due to residual whitecaps is incorrectly treated as enhanced aerosol reflectance. Such assumptions can lead to inaccurate derivations of water-leaving radiance and/or a loss of otherwise useable data.

The current whitecap correction approach also assumes that whitecaps are spectrally flat in the visible wavelengths. Indeed, foam shows a spectrally flat response in that it reflects equally across all visible wavelengths and appears white (*e.g.*, Stabeno and Monahan [1986], Frouin *et al.* [1996], Moore *et al.* [2000]). As the whitecap matures, however, a decrease in reflectance occurs in the red portion of the spectrum due to the strong absorption properties of water molecules [*Frouin et al.*, 1996; *Moore et al.*, 1998]. Furthermore, the spectral shape in the blue and green changes depending on the optical properties of the water itself [*Moore et al.*, 1998; *Stramski and Tegowski*, 2001; *Kokhanovsky*, 2004; *Zhang et al.*, 2004]. The effect of whitecaps on the magnitude and shape of visible light leaving the ocean surface has been presented in previously published studies (*e.g.*, Koepke [1984], Frouin *et al.* [1996], Moore *et al.* [2000], Stramski and Tegowski [2001], and Zhang *et al.* [2002]). However, most of these measurements were collected over ship-generated foam and bubbles (e.g., Moore *et al.* [1998]) or their effects were modeled using radiative transfer (*e.g.*, Stramski and Tegowski [2001]) and none were directly compared to whitecap metrics measured simultaneously using traditional techniques (*e.g.*, Monahan and Spillane, [1984]).

Here, the whitecap correction routine used to process ocean color imagery is evaluated for its effectiveness in the Southern Ocean using optical, radiometric, meteorological and oceanographic measurements collected during the Southern Ocean Gas Exchange Experiment (SO GasEx). First, the relationship between wind speed and whitecap coverage measured radiometrically and using high resolution digital imagery is compared to the parameterizations used in the former and current whitecap correction procedures (*i.e.,* following Monahan and O'Muircheartaigh [1980] and Sramska and Petelski [2003]). Second, the signal of a whitecap-affected surface measured at the satellite (*i.e.*, the area weighted whitecap reflectance) was estimated using both time-averaged measurements of in-water and above-surface radiometry collected at high frequency during strong wind conditions (*i.e.*, containing whitecaps and bubbles) and reflectance measurements of the undisturbed sea surface (*i.e.,* the ideal signal for deriving biogeochemical parameters from ocean color reflectance). The mean spectral enhancement in reflectance over a large footprint (*e.g.*, 250 m^2 to 1 km^2) due to the presence of whitecaps is presented. Third, the average spectral lambertian equivalent reflectance of individual whitecaps is presented and compared to the fixed, 22% effective reflectance of Koepke [1984]. The reflectance measured here is parsed into two, including that of foam, or the spectrally flat portion of the whitecap (directly comparable to that of Koepke [1984]) and that of bubbles, which has a spectral shape in the visible (*i.e.*, 400 to 700 nm). Recommendations for the use of this and additional datasets (*e.g.*, wave field parameters relevant to wave breaking and light scattering) to improve upon the current whitecap correction procedure are discussed.

4.2. Methodology

The enhancement in ocean color reflectance due to whitecaps was determined from radiometric measurements collected above and beneath the sea surface at a high sampling frequency over long time periods. A time-to-space comparison was made to approximate the enhancement in reflectance over a large, 250 m^2 to 1 km^2 footprint (*i.e.*, that of ocean color sensors on satellite platforms) from point-based (IFOV~1 m) measurements. Descriptive statistics of whitecap reflectance, including the effective

reflectance following Koepke [1984], were calculated for breaking events extracted from the time series measurements of radiance using the methodology described in Chapter 3. Whitecap reflectance is presented in the context of the meteorological and biogeochemical conditions.

4.2.1.Radiometry

Time series measurements of the spectral reflectance of breaking waves were captured at high frequency (7 Hz) above the sea surface using a MicroSAS system (SeaWIFS Aircraft Simulator, Satlantic) comprised of three multispectral radiometers (OCR500, Satlantic), including a downwelling irradiance sensor measuring E_d ($\mu W\ cm^{-2}\ nm^{-1}$) and down-looking and sky-viewing radiance sensors measuring L_t ($\mu W\ cm^{-2}\ nm^{-1}\ sr^{-1}$) and L_r ($\mu W\ cm^{-2}\ nm^{-1}\ sr^{-1}$), each with 7 channels between 412 and 680 nm (10 nm spectral bandwidth). The irradiance sensor was mounted upward-looking at the top of the jackstaff at 18 m, where it was unaffected by ship-shadow. The sea and sky-viewing radiometers, deployed at the bow of the *RV Ronald Brown* approximately 5.5 m above the waterline (~1 m^2 instantaneous field of view), were configured to maintain proper viewing angles using a computer-based system that calculates the sun's azimuth angle relative to the ship and adjusts the position of the detector using a stepping motor (see Balch *et al.* [2011]). The MicroSAS data collection procedures are presented in detail by Balch *et al.* [2011]. The subsurface, bubble contribution to reflectance was determined by measuring hyperspectral (350 nm to 800 nm, 1 nm spectral resolution) upwelling radiance at a high sampling frequency (7 Hz) using a Hyperspectral Tethered Radiometer Buoy (HTSRB, Satlantic) equipped with radiance sensors at 0.65 m, 2 m and 5 m below the sea surface. Upwelling radiance measured at the three depths was extrapolated to immediately below the air-sea interface using a linear fit to a log transformed profile. Transmittance across the air-sea interface was estimated following Mobley [1994]. See Chapter 3 for additional background on the radiometric quantities measured.

Single, point-based measurements of remote sensing reflectance collected using a hand-held spectroradiometer following the protocol described by Austin [1974], Carder and Steward [1985], Lee *et*

al. [2010]. Details on the collection of this data can be found in Lee *et al.* [2011]. The mean enhancement in reflectance due to breaking waves was determined by subtracting the background reflectance (*i.e.*, reflectance of the undisturbed sea surface) from the mean of the 20 min time series of reflectance (see Section 4.2.4 for time-to-space comparison). At these stations, reflectance from the handheld spectroradiometer was compared to the lowest 5% of radiometric data collected using the MisrcoSAS and HTSRB for consistency. For stations without data from the handheld spectroradiometer, the lowest 5% of radiometric data from both instruments was used to as the background refectance.

In addition to remote sensing reflectance, R_{rs} (sr^{-1}), the lambertian equivalent reflectance (LER) was estimated by multiplying the MicroSAS and HTSRB measured upwelling radiance by pi. The time series LER of full individual whitecaps was extracted following the methodology presented in Chapter 3, Section 3.5. Descriptive statistics were calculated for all of the full whitecap events in the time series. The maximum and effective reflectance of the whitecaps measured here were compared to previously published values (*e.g.*, Whitelock *et al.* [1982] and Koepke [1984]).

4.2.2. Whitecap detection and metrics

Whitecap events were identified in the time series measurements of upwelling radiance collected using the down-looking multispectral radiometer deployed as a part the MicroSAS system. Background radiance was removed using a min-max filtering technique. Bright features lasting less than 2 s in duration were assumed to be glint and were eliminated from further analysis. Details on the retrieval of whitecap metrics, including fraction coverage, using radiometry are presented in Chapter 3. Whitecap coverage was also estimated using high-resolution digital images from two Imperx CCD cameras sampling 100 m^2 areas at 5 Hz from the Flying Bridge (port and starboard side looking) of the *RV Ronald Brown* [*Zappa et al.*, 2012]. Background intensity gradients were removed and breaking statistics were determined using the approach of Callaghan and White [2009].

4.2.3. Meteorological and oceanographic measurements

Neutral wind speeds at the reference height of 10 m (U_{10}), were measured using an air-sea flux package deployed on the jack-staff of the ship [*Edson et al.*, 2011]. The wind friction velocity (u∗), used to estimate the surface drift velocity, was determined from vertical and horizontal velocity fluctuations using the direct covariance method [*Edson et al.*, 2011]. The wave frequency spectrum from 0.03 to 1.2 Hz was determined by combining measurements from a Wave Monitoring System (WaMoS II), a Riegl LD-90 laser altimeter, and a TSKA SWHM wave height meter [*Cifuentes-Lorenzen et al.*, 2013]. Wave field statistics, including the significant wave height of the dominant waves (H_s) were determined from the measured wave frequency spectrum. Wind and wave metrics are reported here to provide a context for the mean whitecap enhanced reflectance and the effective reflectance of whitecaps measured during SO GasEx.

4.2.4. Time-to-space comparison

Here, a spatial (~ 1 km^2) estimate of the mean enhancement in reflectance due to whitecaps was estimated from time series measurements of radiance sampled at high frequency within a small footprint. The spatial coverage captured using the point-based sampling approach was estimated from the instantaneous field of view (IFOV) of the instrument, the record length, and an estimate of the drift velocity (*i.e.*, breaking velocity). For stationary radiance measurements (*i.e.*, speed over ground < 1 m s^{-1}) collected while the ship maintained a constant heading into the wind, the surface area advected past the instrument, *A*, is

$$A(\Delta t, L, u_o) = \pi\ (L\ u_o\ \Delta t)$$

where L is the diameter of the IFOV (m), Δt is the time interval of sampling (*i.e.*, record length), and u_o (m s^{-1}) is the surface drift velocity. The surface drift velocity is assumed to be the advection velocity associated with a passing whitecap and was approximated following Wu [1983]:

$$u_o = \alpha\, u_*$$

where u_* (m s^{-1}) is the atmospheric friction velocity and α is a numerical constant (α = 0.53). Here, record lengths were optimized so that A~1 km^2.

4.2.5.Optical and analytical measurements

Discrete measurements of chlorophyll *a* and total suspended material were made from surface water samples collected at each station. Chlorophyll *a* (Chl) was extracted and determined fluorometrically from filtered water according to Wright *et al.* [2005] and Welschmeyer [1994] and measured in triplicate for most stations [*Lance et al.*, 2012a]. Total suspended material was determined gravimetrically following the procedure outlined in NASA's Ocean Optics Protocols [*Mueller et al.*, 2004]. Absorption by CDOM at 440 nm [a_g(440)] was measured for water samples filtered through a 0.2 μm filter using an ultrapath spectroradiometer (WPI). Details on the analytical procedure for measuring a_g(440) can be found in Miller *et al.* [2002].

4.3. Results and discussion

4.3.1. The wind speed-whitecap coverage relationship

The wind speed-whitecap relationship based on fractional coverage retrievals using radiometry (black circles) and high-resolution digital imagery (grey circles) during a large range in wind (3 - 22 m s^{-1}) and wave (significant wave heights of 3 - 5 m) conditions in the Atlantic sector of the Southern Ocean showed substantial scatter, specifically at high wind speeds (Figure 1). The fractional whitecap coverage parameterization of Stramska and Petelski [2003] based on wind speed, currently used in the ocean color correction routines, was biased low for moderate wind speeds (*i.e.*, 6 to 12 m s^{-1}) relative to whitecap retrievals from radiometry, which include the full whitecap from initiation through decay. The Monahan and O'Muircheartaigh [1980] parameterization, used in the original whitecap correction routine, produced an improved estimate of fractional coverage in the Southern Ocean for wind speeds < 12 m s^{-1}. Strong agreement between the radiometrically derived whitecap coverage and the Stramska and Petelski [2003] parameterization was found among wind speeds in excess of 12 m s^{-1}, however a fixed correction is

applied to ocean color imagery for these wind conditions. When compared to fractional whitecap coverage measured using high resolution digital imagery, which captured the brightest whitecap features (see Chapter 2), the Stramska and Petelski [2003] wind speed-whitecap relationship provided a better estimate than the formerly used Monahan and O'Muircheartaigh [1980] parameterization for wind speeds < 11 m s^{-1}. During high wind conditions ($\geq$ 11 m s^{-1}), however, the Monahan and O'Muircheartaigh [1980] approach provided a more accurate prediction.

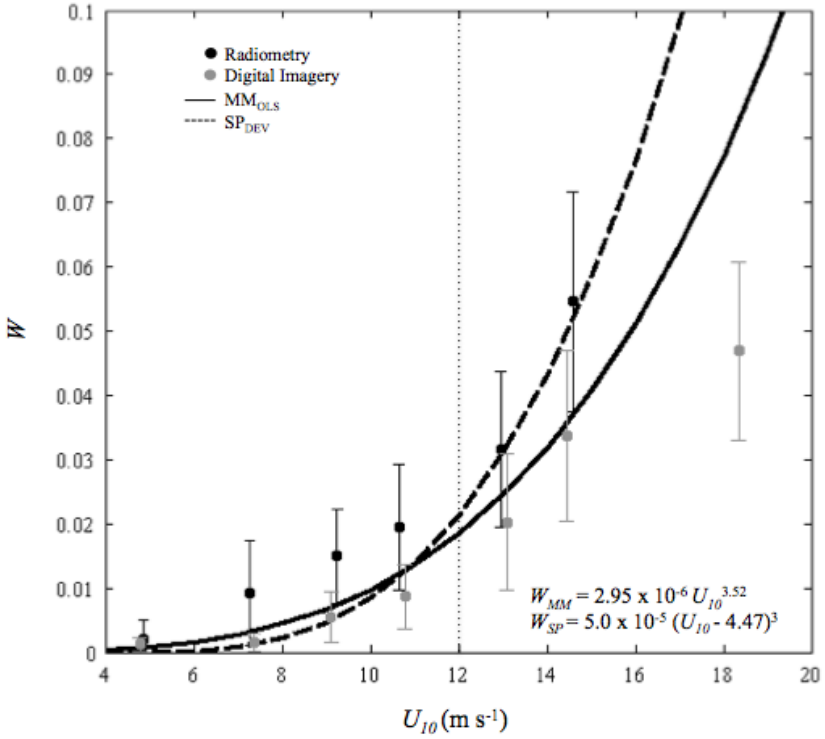

Figure 1: The relationship between wind speed (U_{10}) and whitecap coverage (W) retrieved using the radiometric method presented in Chapter 2 (black circles) and the traditional approach using high-resolution digital imagery (grey circles). Wind speed-whitecap parameterizations are shown for comparison, including Monahan and O'Muircheartaigh [1980], used in the original whitecap correction for ocean color imagery (equation 1, solid

line), and the Stramska and Petelski [2003] parameterization for developed seas (equation 2, dashed line) used in the new correction routine. For wind speeds > 12 m s^{-1} (dotted line) a single, fixed correction is applied.

4.3.2 Enhancement in the mean spectral reflectance due to whitecaps

The strong effect of whitecaps on upwelling radiance over short (*i.e.*, whitecap duration) time scales (see Chapter 3) results in a whitecap-induced enhancement in the mean of time series measurements of reflectance collected over a long (~20 min or more) sampling period, roughly equivalent to remote sensing reflectance for the ~1 km^2 pixel routinely measured using ocean color sensors on satellite platforms. The mean reflectance measurement containing foam and bubbles (Figure 2a, dark grey line with circles) and bubbles alone (Figure 2a, light gray line) show a change in the magnitude and spectral shape of reflectance when compared to measurements of the water column known to be whitecap free (Figure 2a, black line). The whitecap enhanced reflectance measured during high wind conditions (U_{10}~13 m s^{-1}) with wave breaking (Day 76, chlorophyll *a*~0.47 mg m^{-3}) demonstrated a magnitude increase of 40-50% in the blue (411 - 490 nm) and ~50-55% in the green (510 - 554 nm) portion of the spectrum measured above the surface (Table 1). Bubbles are the cause of the enhancement in reflectance in the green; the bubble plume at 0.65 m and deeper, observed in radiance measurements collected beneath the sea surface, produced enhancements of ~20-30% in the blue, ~30-40% in the green and <10% in the red (Figure 5b) above the background reflectance. Strong agreement was observed between the reflectance measurements collected using the three techniques during low wind conditions with no wave breaking (Figure 2b, dark and light grey lines with circles, black line) and between the 5^{th} percentile (*i.e.*, background) measurements during days with wave breaking (< 0.002 sr^{-1}; Figure 2a, dashed lines with x's).

Table 1: Physical, biological and optical measurements from discrete water samples collected in the Southern Ocean, including the mean neutral wind speed (at 10 m) for the sampling period (U_{10N}, m s^{-1}),

fractional whitecap coverage (*W*, dimensionless) from high resolution digital imagery (*DI*) and radiometry (*Rad.*), chlorophyll *a* concentration (*Chl*, mg m^{-3}), total suspended material (*TSM*; g m^{-3}), CDOM absorption at 440 nm (a_g[440]; m^{-1}). Empty fields indicate no data.

Station Day of year	**U_{10}** ($m\ s^{-1}$)	**W** *Rad.* *DI*	**H_S** (m)	**Chl**[1] ($mg\ m^{-3}$)	**TSM** ($g\ m^{-3}$)	**a_g(440)** (m^{-1})
76	13.8	0.032 0.007	2.8	0.47[a]	3.88	
84	13.0	0.012 0.037	3.4	0.72	0.55	0.0590
92	5.8	0.003	2.7	0.48	0.31	0.0506

[1]Measurements from Lance *et al.* [2012b]
[a]Chlorophyll calculated using remote sensing reflectance following O'Reilly *et al.* [2000]
Control Station, no whitecaps

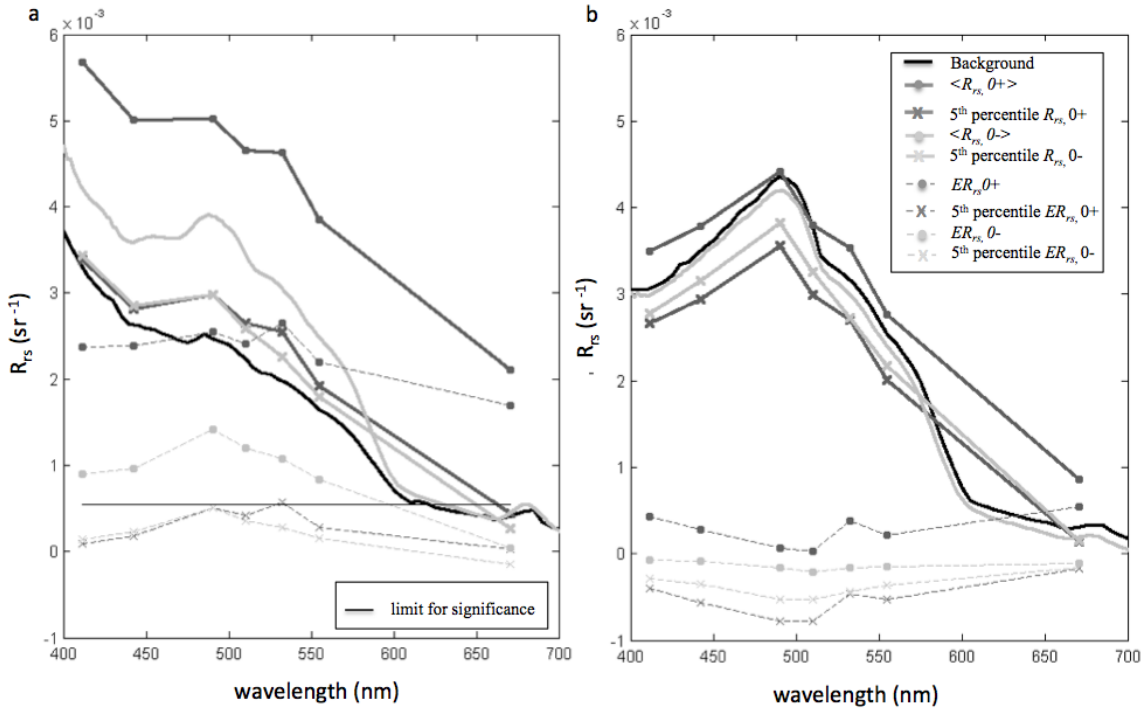

Figure 2: The mean (<R_{rs}>; solid lines) reflectance from a 20-minute time series of upwelling radiance measurements collected above the surface (0+, dark grey line with circles) and subsurface (0-, light grey line) and reflectance of the undisturbed water column (background, black line) (a) sampled during high

wind conditions with wave breaking (yearday 76) and (b) during low wind conditions without wave breaking (yearday 92). The lowest 5% (lines with x's) of the measurements collected at high sampling frequency both above and below the surface were assumed to represent the background reflectance. The whitecap induced enhancement in the mean reflectance (eR_{rs}) above surface (dark grey dashed line with circles) and below surface (light grey dashed line with circles) was determined by subtracting the background reflectance (bold black line). This is also shown for the 5th percentile reflectance (dashed lines with x's). A limit for significance in the whitecap-induced enhancement in reflectance was determined from data collected on days without whitecaps (*i.e.,* panel b) and is shown in panel a (thin black line).

Bubbles from breaking waves alter the spectral shape of reflectance in a manner dependent on the optical properties of the water. Here, the whitecap-induced spectral shape change in reflectance measured at two SO GasEx stations (days 76 and 84, thin solid lines), with similar fractional whitecap coverage (O[10^{-2}]) but markedly different biogeochemical conditions (Table 1) and background reflectance (Figure 3, bold lines), showed an enhancement primarily in the green portion of the spectrum. For these two stations, the magnitude of the spectral shape change is dependent on the background reflectance. The whitecap enhancement in reflectance normalized to 411 nm suggests that, for greener water (*i.e.*, day 84) the relative enhancement between 500 and 550 nm was 10% higher while, for bluer water (*i.e.*, day 76) the enhancement was 5% greater in the green relative to the blue (Figure 3, dashed lines with points). Application of a spectrally flat correction (*i.e.*, $eR_{rs}(650)$ subtraction) results in an overestimation of reflectance from 412 nm to (solid lines with points) by ~0.25 x10^{-3} to 0.62x10^{-3} (Figure 3, dot-dashed lines).

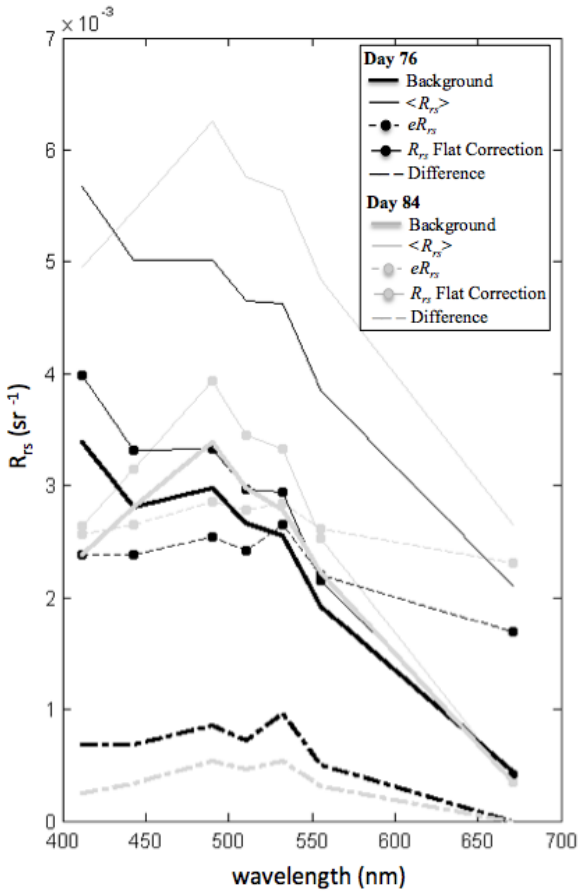

Figure 3: Remote sensing reflectance (R_{rs}; sr^{-1}) for two stations, day 76 (black lines) and day 84 (grey lines), with a similar fractional whitecap coverage (O[10^{-2}]) but different optical properties and background reflectance (solid, bold lines). Included are the whitecap-affected mean reflectance (solid, thin line), the whitecap-induced enhancement in reflectance (eR_{rs}) from foam and bubbles (dashed line with circles), and the background reflectance determined by applying a spectrally flat correction using $eR_{rs}(650)$. The difference between the measured background reflectance and the background reflectance retrieved by applying the $eR_{rs}(650)$ ranged from 0.25 x10^{-3} to 0.62x10^{-3} (dot-dashed lines).

4.3.3 Reflectance of individual whitecaps

The spectral effect of whitecaps on the mean reflectance is more easily understood when tracking the reflectance of an individual whitecap measured at a high sampling frequency above and beneath the surface over time. While the assumption that whitecaps are spectrally flat in the visible holds during the

active phase of wave breaking, whitecap events show strong changes the spectral distribution of reflectance as they mature (over time periods on the order of seconds to tens of seconds). When tracing a single event from breaking through decay in the above surface reflectance measurement of foam and bubbles, the whitecap initially appears spectrally flat (Figure 4a). As the whitecap matures, a rapid decrease in reflectance in the red portion of the spectrum occurs due to the strong absorption properties of water molecules. In the blue and green portions of the spectrum, the change in reflectance is driven by submerged bubbles and is dependent on the optical properties of the water such the water appears green enhanced throughout the decay of the whitecap (Figure 4b and c). The in-water, high frequency (1 Hz) measurements of reflectance (R_{rs}; sr^{-1}) for a single whitecap event presents as a bright, spectrally flat feature initially but as the whitecap matures, it becomes green-enhanced before returning to the background reflectance of the undisturbed surface (Figure 5).

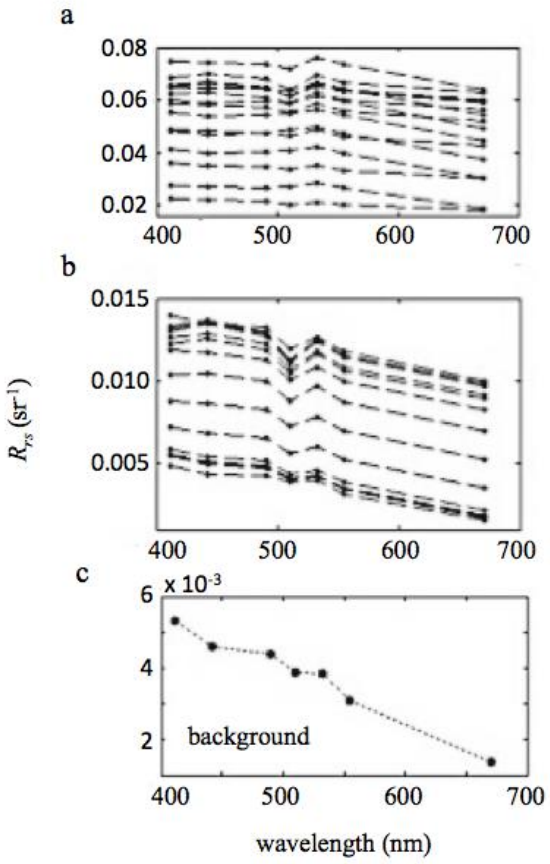

Figure 4: (a, b) Above surface, high temporal resolution reflectance (R_{rs}; sr^{-1}) for an ~25 s whitecap event (the lines represent 1 s averages of 7 Hz data) shows a strong enhancement in the magnitude of reflectance and the change in spectral shape over time compared to the (c) the median, background reflectance measured before the whitecap.

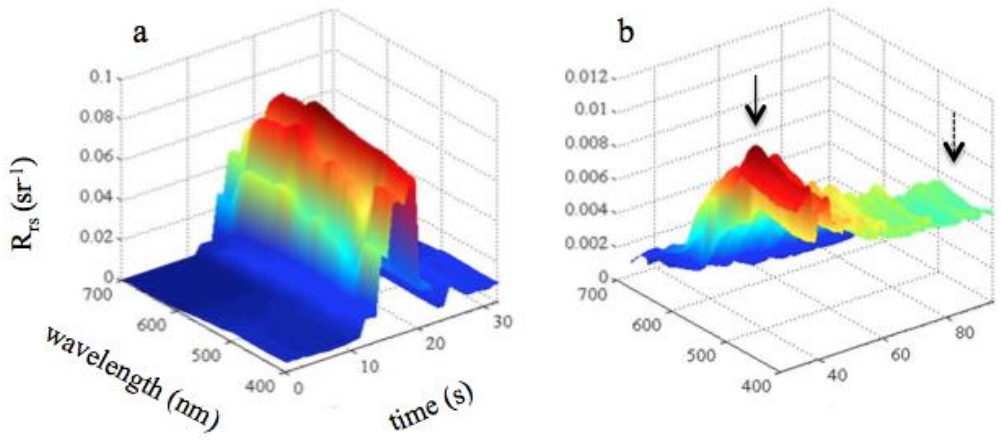

Figure 5: The in-water, high frequency (1 Hz) measurements of reflectance (R_{rs}; sr^{-1}) for a single whitecap event during high wind conditions (13 m s^{-1}) shows an enhancement in the magnitude of reflectance throughout the entire event, lasting ~50 s and spectral distribution of reflectance, where (a) the background reflectance (0-12 s) increased ten-fold and was similar across all wavelengths (spectrally flat) for the first ~10 s (12-20 s); (b) as the whitecap matures, reflectance is much lower and becomes green-enhanced (~20 to 60 s; solid arrow) before returning to the background reflectance signal (dashed arrow) measured for the undisturbed surface (60-80 s).

During any full individual whitecap event, a maximum lambertian equivalent reflectance of up to 68% (490 nm) was observed, exceeding the 55% reflectance of dense foam according to Whitlock *et al.* [1982] and Stabeno and Monahan [1986] (Figure 6a). The largest effective reflectance, or mean LER(490), observed during 9-15 m s^{-1} wind speed conditions, was 27%, slightly higher than the 22% effective reflectance of Koepke [1984]. On average, however, the effective reflectance measured here was closer to 13% (Figure 6b).

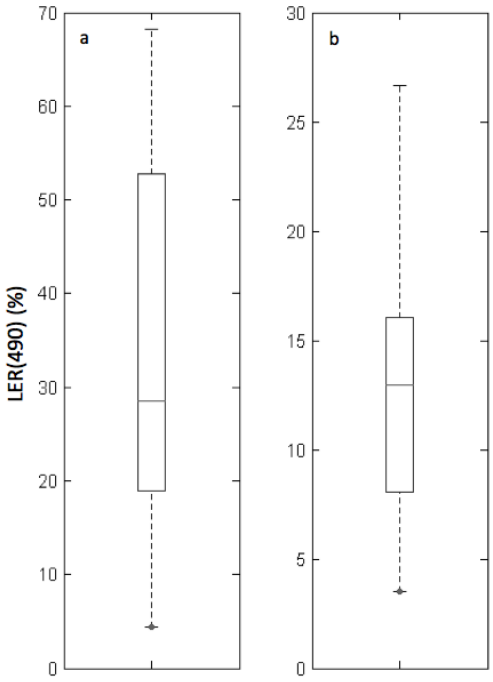

Figure 6: The (a) maximum and (b) mean lambertian equivalent reflectance at 490 nm (LER[490]; %) retrieved from the upper 75th percentile of 49 independent whitecap events (those considered to be fully captured by the radiometer) measured during 9-15 m s^{-1} wind speed conditions.

4.4 Conclusions

Preliminary results from the dataset presented herein emphasize the need for the validation of and improvements on the current whitecap correction routine used to process ocean color imagery. The wind speed-fractional whitecap coverage relationship for the Southern Ocean dataset shows large scatter and the currently used parameterization, upon which the ocean color whitecap correction routine is based, underestimates the total coverage (*i.e.*, Stage A through the late stage gamma plume) for wind speeds < 12 m s^{-1}. The average effective reflectance of individual whitecaps, retrieved using the radiometric method presented in this thesis, was 13%, highly variable and warrants further investigation. Finally, the mean enhanced reflectance for a 20 minute record (analogous to reflectance measured over a 1 km^2 footprint) and the high frequency measurement of individual whitecap events show strong changes in the

spectral distribution of reflectance as the whitecap matures, particularly in the green portion of the spectrum.

An area of continued research will be to investigate the relationship between wind speed and the spectral enhancement in reflectance due to whitecaps, achievable using the dataset presented here. Such relationships offer an alternative to using fractional coverage in the whitecap correction routine. Future research also includes further partitioning the fractional coverage and spectral shapes of each stage of the whitecap feature from initiation through decay (*i.e.*, Stage A, Stage B, and the gamma bubble plume). Such analysis will allow for better incorporation of the spectral influence of foam and bubbles on the magnitude and spectral shape of the derived ocean color spectrum and potentially lead to new methods to retrieve whitecap features from ocean color imagery.

References

Andreas, E. L., J. B. Edson, E. C. Monahan, M. P. Rouault, and S. D. Smith (1995), The spray contribution to net evaporation from the sea: A review of recent progress, *Boundary-Layer Meteorology*, *72*(1-2), 3–52.

Arrigo, K. R., D. Worthen, A. Schnell, and M. P. Lizotte (1998), Primary production in Southern Ocean waters, *J. Geophys. Res.*, *103*(C8), 15587–15600, doi:10.1029/98JC00930.

Asher, W., J. Edson, W. Mcgillis, R. Wanninkhof, D. T. Ho, and T. Litchendor (2002), Fractional Area Whitecap Coverage and Air-Sea Gas Transfer Velocities Measured During GasEx-98, in *Gas Transfer at Water Surfaces*, pp. 199–203, American Geophysical Union.

Austin, R. (1974), Inherent spectral radiance signatures of the ocean surface, *Ocean color analysis*, *7410*, 1–20.

Bailey, S. W. (2009), *Whitecap Reflectance*, NASA Ocean Biology Processing Group.

Balch, W. M., K. A. Kilpatrick, and C. C. Trees (1996), The 1991 coccolithophore bloom in the central North Atlantic. 1. Optical properties and factors affecting their distribution, *Limnol. Oceanogr.*, *41*(8), 1669–1683, doi:10.4319/lo.1996.41.8.1669.

Balch, W. M., D. T. Drapeau, T. L. Cucci, R. D. Vaillancourt, K. A. Kilpatrick, and J. J. Fritz (1999), Optical backscattering by calcifying algae: Separating the contribution of particulate inorganic and organic carbon fractions, *Journal of Geophysical Research: Oceans (1978–2012)*, *104*(C1), 1541–1558.

Balch, W. M., H. R. Gordon, B. C. Bowler, D. T. Drapeau, and E. S. Booth (2005), Calcium carbonate measurements in the surface global ocean based on Moderate-Resolution Imaging Spectroradiometer data, *J. Geophys. Res.*, *110*(C7), C07001, doi:10.1029/2004JC002560.

Balch, W. M., D. T. Drapeau, B. C. Bowler, E. Lyczskowski, E. S. Booth, and D. Alley (2011), The contribution of coccolithophores to the optical and inorganic carbon budgets during the Southern Ocean Gas Exchange Experiment: New evidence in support of the "Great Calcite Belt" hypothesis, *J. Geophys. Res.*, *116*, C00F06, doi:10.1029/2011JC006941.

Behrenfeld, M. J., and P. G. Falkowski (1997), Photosynthetic rates derived from satellite-based chlorophyll concentration, *Limnology and oceanography*, *42*(1), 1–20.

Bondur, V., and E. Sharkov (1982a), STATISTICAL CHARACTERISTICS OF FOAM FORMATIONS ON A DISTURBED SEA-SURFACE, *Okeanologiya*, *22*(3), 372–379.

Bondur, V. G., and E. A. Sharkov (1982b), Statistical properties of whitecaps on a rough sea, *Oceanology*, *22*(3), 274–279.

Bortkovskii, R., and V. Novak (1993), Statistical dependencies of sea state characteristics on water temperature and wind-wave age, *Journal of marine systems*, *4*(2), 161–169.

Bortkovskii, R. S. (1987), *Air-sea exchange of heat and moisture during storms*, Kluwer Boston Inc., Hingham, MA.

Bouguet, J.-Y. (2004), *Camera calibration toolbox for matlab*, MRL - Intel Corp.

Briggs, N., M. J. Perry, I. Cetinić, C. Lee, E. D'Asaro, A. M. Gray, and E. Rehm (2011), High-resolution observations of aggregate flux during a sub-polar North Atlantic spring bloom, *Deep Sea Research Part I: Oceanographic Research Papers*, *58*(10), 1031–1039.

Brown, O. B., and H. R. Gordon (1973), Two component Mie scattering models of Sargasso Sea particles, *Applied optics*, *12*(10), 2461–2465.

Callaghan, A. H. (2013), An improved whitecap timescale for sea spray aerosol production flux modeling using the discrete whitecap method, *J. Geophys. Res. Atmos.*, *118*(17), 9997–10,010, doi:10.1002/jgrd.50768.

Callaghan, A. H., and M. White (2009), Automated processing of sea surface images for the determination of whitecap coverage, *Journal of Atmospheric and Oceanic Technology*, *26*(2), 383–394.

Carder, K., and R. Steward (1985), A remote-sensing reflectance model of a red-tide dinoflagellate off west Florida1, *Limnology and Oceanography*, *30*(2), 286–298.

Cifuentes-Lorenzen, A., J. B. Edson, C. J. Zappa, and L. Bariteau (2013), A Multisensor Comparison of Ocean Wave Frequency Spectra from a Research Vessel during the Southern Ocean Gas Exchange Experiment, *J. Atmos. Oceanic Technol.*, doi:10.1175/JTECH-D-12-00181.1.

Dierssen, H. M. (2010), Perspectives on empirical approaches for ocean color remote sensing of chlorophyll in a changing climate, *Proceedings of the National Academy of Sciences*, *107*(40), 17073–17078.

Dierssen, H. M., and R. C. Smith (2000), Bio-optical properties and remote sensing ocean color algorithms for Antarctic Peninsula waters, *J. Geophys. Res.*, *105*(C11), 26301–26312, doi:10.1029/1999JC000296.

Dierssen, H. M., R. C. Smith, and M. Vernet (2002), Glacial meltwater dynamics in coastal waters west of the Antarctic peninsula, *Proceedings of the National Academy of Sciences*, *99*(4), 1790–1795.

Donelan, M., M. S. LONGUET-HIGGINS, and J. S. TURNER (1972), Periodicity in Whitecaps, *Nature*, *239*(5373), 449–451, doi:10.1038/239449a0.

Fairall, C. W., E. F. Bradley, J. E. Hare, A. A. Grachev, and J. B. Edson (2003), Bulk Parameterization of Air–Sea Fluxes: Updates and Verification for the COARE Algorithm, *J. Climate*, *16*(4), 571–591, doi:10.1175/1520-0442(2003)016<0571:BPOASF>2.0.CO;2.

Flatau, P. J., M. Flatau, J. R. V. Zaneveld, and C. D. Mobley (2000), Remote sensing of bubble clouds in sea water, *Q.J.R. Meteorol. Soc.*, *126*(568), 2511–2523, doi:10.1002/qj.49712656808.

Franz, B. A. (2015), *Algorithm for Retrieval of Remote Sensing Relectance from Satellite Ocean Color Sensors*, NASA Ocean Biology Processing Group.

Frouin, R., M. Schwindling, and P.-Y. Deschamps (1996), Spectral reflectance of sea foam in the visible and near-infrared: In situ measurements and remote sensing implications, *J. Geophys. Res.*, *101*(C6), 14361–14371, doi:10.1029/96JC00629.

Goddijn-Murphy, L., D. K. Woolf, and A. H. Callaghan (2011), Parameterizations and algorithms for oceanic whitecap coverage, *Journal of Physical Oceanography*, *41*(4), 742–756.

Gordon, H. R. (1997), Atmospheric correction of ocean color imagery in the Earth Observing System era, *J. Geophys. Res.*, *102*(D14), 17081–17106, doi:10.1029/96JD02443.

Gordon, H. R., and M. Wang (1994), Influence of oceanic whitecaps on atmospheric correction of ocean-color sensors, *Applied Optics*, *33*(33), 7754–7763.

Hanson, J. L., and O. M. Phillips (1999), Wind Sea Growth and Dissipation in the Open Ocean, *J. Phys. Oceanogr.*, *29*(8), 1633–1648, doi:10.1175/1520-0485(1999)029<1633:WSGADI>2.0.CO;2.

Ho, D. T., C. L. Sabine, D. Hebert, D. S. Ullman, R. Wanninkhof, R. C. Hamme, P. G. Strutton, B. Hales, J. B. Edson, and B. R. Hargreaves (2011), Southern Ocean Gas Exchange Experiment: Setting the stage, *J. Geophys. Res.*, *116*, C00F08, doi:10.1029/2010JC006852.

Hooker, S. B., L. Van Heukelem, C. S. Thomas, H. Claustre, J. Ras, R. Barlow, H. Sessions, L. Schlüter, J. Perl, and C. Trees (2005), *Second SeaWiFS HPLC Analysis Round-robin Experiment (SeaHARRE-2)*, National Aeronautics and Space Administration, Goddard Space Flight Center.

Johnson, B. D., and R. C. Cooke (1980), Organic Particle and Aggregate Formation Resulting from the Dissolution of Bubbles in Seawater, *Limnology and Oceanography*, *25*(4), 653–661.

Johnson, B. D., and R. C. Cooke (1981), Generation of Stabilized Microbubbles in Seawater, *Science*, *213*(4504), 209 –211.

Jonasz, M., and G. Fournier (2011), *Light Scattering by Particles in Water: Theoretical and Experimental Foundations: Theoretical and Experimental Foundations*, Academic Press.

Koepke, P. (1984), Effective reflectance of oceanic whitecaps, *Appl. Opt.*, *23*(11), 1816–1824.

Kokhanovsky, A. A. (2004), Spectral reflectance of whitecaps, *J. Geophys. Res.*, *109*(C5), C05021, doi:10.1029/2003JC002177.

Lance, V. P., P. G. Strutton, R. D. Vaillancourt, B. R. Hargreaves, J.-Z. Zhang, and J. Marra (Submitted), Primary productivity, new productivity and carbon export during two Southern Ocean Gas Exchange (SO GasEx) tracer experiments, *J. Geophys. Res.*

Lance, V. P., P. G. Strutton, R. D. Vaillancourt, B. R. Hargreaves, J.-Z. Zhang, and J. Marra (2012a), Primary productivity, new productivity, and their relation to carbon flux during two Southern Ocean Gas Exchange tracer experiments, *J. Geophys. Res.*, *117*(C4), C00F14, doi:10.1029/2011JC007687.

Lance, V. P., P. G. Strutton, R. D. Vaillancourt, B. R. Hargreaves, J.-Z. Zhang, and J. Marra (2012b), Primary productivity, new productivity, and their relation to carbon flux during two Southern Ocean Gas Exchange tracer experiments, *J. Geophys. Res.*, *117*(C4), C00F14, doi:10.1029/2011JC007687.

Lee, M. E., and M. R. Lewis (2003), A New Method for the Measurement of the Optical Volume Scattering Function in the Upper Ocean, *J. Atmos. Oceanic Technol.*, *20*(4), 563–571, doi:10.1175/1520-0426(2003)20<563:ANMFTM>2.0.CO;2.

Lee, Z., K. L. Carder, and R. A. Arnone (2002), Deriving Inherent Optical Properties from Water Color: a Multiband Quasi-Analytical Algorithm for Optically Deep Waters, *Appl. Opt.*, *41*(27), 5755–5772.

Lee, Z., Y.-H. Ahn, C. Mobley, and R. Arnone (2010), Removal of surface-reflected light for the measurement of remote-sensing reflectance from an above-surface platform, *Optics Express*, *18*(25), 26313–26324.

Lee, Z., V. P. Lance, S. Shang, R. Vaillancourt, S. Freeman, B. Lubac, B. R. Hargreaves, C. Del Castillo, R. Miller, and M. Twardowski (2011), An assessment of optical properties and primary

production derived from remote sensing in the Southern Ocean (SO GasEx), *Journal of Geophysical Research: Oceans (1978–2012), 116*(C4).

Lemire, D. (2006), Streaming maximum-minimum filter using no more than three comparisons per element, *arXiv preprint cs/0610046*.

Liss, P. S., and L. Merlivat (1986), Air-sea gas exchange rates: introduction and synthesis, in *The Role of Air-Sea Exchange in Geochemical Cycling*, edited by P. Buat-Menard, pp. 113–129, Reidel, Washington.

Longhurst, A., S. Sathyendranath, T. Platt, and C. Caverhill (1995), An estimate of global primary production in the ocean from satellite radiometer data, *Journal of Plankton Research, 17*(6), 1245–1271.

Maritorena, S., D. A. Siegel, and A. R. Peterson (2002), Optimization of a semianalytical ocean color model for global-scale applications, *Appl. Opt.*, *41*(15), 2705–2714.

Miller, R. L., M. Belz, C. Del Castillo, and R. Trzaska (2002), Determining CDOM absorption spectra in diverse coastal environments using a multiple pathlength, liquid core waveguide system, *Continental Shelf Research*, *22*(9), 1301–1310.

Mitchell, B. G., and O. Holm-Hansen (1991), Observations of modeling of the Antartic phytoplankton crop in relation to mixing depth, *Deep Sea Research Part A. Oceanographic Research Papers*, *38*(8), 981–1007.

Mobley, C. D. (1994), *Light and Water*, Academic Press, San Diego, CA.

Monahan, E.C. (1993), Occurrence and Evolution of Acoustically Relevant Sub-Surface Bubble Plumes and their Associated, Remotely Monitorable, Surface Whitecaps, in *Natural Physical Sources of Underwater Sound*, edited by B. R. Kerman, pp. 503–517, Springer Netherlands.

Monahan, E. C. (1989), From the laboratory tank to the global ocean, *The climate and health implications of bubble-mediated sea-air exchange*, 43–63.

Monahan, E. C., and H. G. Dam (2001), Bubbles: An estimate of their role in the global oceanic flux of carbon, *J. Geophys. Res.*, *106*(C5), 9377–9383, doi:10.1029/2000JC000295.

Monahan, E. C., and M. Lu (1990), Acoustically relevant bubble assemblages and their dependence on meteorological parameters, *Oceanic Engineering, IEEE Journal of*, *15*(4), 340–349, doi:10.1109/48.103530.

Monahan, E. C., and C. F. Monahan (1986), The Influence of Fetch on Whitecap Coverage as Deduced from the Alte Weser Lightstation Observer's Log, in *Oceanic Whitecaps*, vol. 2, edited by E. Monahan and G. Niocaill, pp. 275–277, Springer Netherlands.

Monahan, E. C., and I. Muircheartaigh (1980), Optimal Power-Law Description of Oceanic Whitecap Coverage Dependence on Wind Speed, *J. Phys. Oceanogr.*, *10*(12), 2094–2099, doi:10.1175/1520-0485(1980)010<2094:OPLDOO>2.0.CO;2.

Monahan, E. C., and M. C. Spillane (1984), The role of oceanic whitecaps in air sea gas exchange, in *Gas Transfer at Water Surfaces*, edited by W. Brutsaert and G. H. Jirka, pp. 495–504, D. Reidel, Norwell, MA.

Monahan, E. C., and D. K. Woolf (1989), Comments on "Variations of Whitecap Coverage with Wind stress and Water Temperature, *J. Phys. Oceanogr.*, *19*(5), 706–709, doi:10.1175/1520-0485(1989)019<0706:COOWCW>2.0.CO;2.

Monahan, E. C., and C. R. Zietlow (1969), Laboratory comparisons of fresh-water and salt-water whitecaps, *J. Geophys. Res.*, *74*(28), 6961–6966, doi:10.1029/JC074i028p06961.

Monahan, E. C., P. Bowyer, D. Doyle, M. Higgins, and D. K. Woolf (1984), *Whitecaps and the marine atmosphere*, University College Rep. 7, Galway, Ireland.

Monahan, E. C., D. E. Spiel, and K. L. Davidson (1986), A model of marine aerosol generation via whitecaps and wave disruption, in *Oceanic whitecaps*, pp. 167–174, Springer.

Moore, K. D., K. J. Voss, and H. R. Gordon (1998), Spectral Reflectance of Whitecaps: Instrumentation, Calibration, and Performance in Coastal Waters, *J. Atmos. Oceanic Technol.*, *15*(2), 496–509, doi:10.1175/1520-0426(1998)015<0496:SROWIC>2.0.CO;2.

Moore, K. D., K. J. Voss, and H. R. Gordon (2000), Spectral reflectance of whitecaps: Their contribution to water-leaving radiance, *J. Geophys. Res.*, *105*(C3), 6493–6499, doi:10.1029/1999JC900334.

Mueller, J. L. et al. (2003), Ocean optics protocols for satellite ocean color sensor validation, revision 4, volume III: Radiometric Measurements and Data Analysis Protocols, edited by J. L. Mueller, G. S. Fargion, and C. R. McClain, *NASA Tech. Memo*, 01674–0.

Mueller, J. L., G. S. Fargion, C. R. McClain, J. Mueller, S. Brown, D. Clark, B. Johnson, H. Yoon, K. Lykke, and S. Flora (2004), *Ocean Optics Protocols For Satellite Ocean Color Sensor Validation, Revision 5, Volume VI: Special Topics in Ocean Optics Protocols, Part 2*, NASA Report 211621, 2003, 1-36.

Nordberg, W., J. Conaway, D. B. Ross, and T. Wilheit (1971), Measurements of microwave emission from a foam-covered, wind-driven sea, *Journal of the Atmospheric Sciences*, *28*(3), 429–435.

O'Reilly, J. E., S. Maritorena, D. A. Siegel, M. C. O'Brien, D. Toole, B. G. Mitchell, M. Kahru, F. P. Chavez, P. Strutton, and G. F. Cota (2000), Ocean color chlorophyll a algorithms for SeaWiFS, OC2, and OC4: Version 4, *SeaWiFS postlaunch calibration and validation analyses, Part*, *3*, 9–23.

Petzold, T. J. (1972), *Volume scattering functions for selected ocean waters*, DTIC Document.

Randolph, K., H. M. Dierssen, M. Twardowski, A. Cifuentes-Lorenzen, and C. J. Zappa (2014), Optical measurements of small deeply penetrating bubble populations generated by breaking waves in the Southern Ocean, *J. Geophys. Res. Oceans*, n/a–n/a, doi:10.1002/2013JC009227.

Reynolds, R. A., D. Stramski, and B. G. Mitchell (2001), A chlorophyll-dependent semianalytical reflectance model derived from field measurements of absorption and backscattering coefficients within the Southern Ocean, *Journal of Geophysical Research: Oceans (1978–2012)*, *106*(C4), 7125–7138.

Roesler, C. S., and E. Boss (2002), A novel relfectance inversion model: retrieval of beam attenuation coefficients and particle size ditributions from ocean color, Office of Naval Research, Santa Fe, NM.

Ross, D. B., and V. Cardone (1974), Observations of oceanic whitecaps and their relation to remote measurements of surface wind speed, *Journal of Geophysical Research*, *79*(3), 444–452.

Scanlon, B., and B. Ward (2013), Oceanic wave breaking coverage separation techniques for active and maturing whitecaps, *Methods in Oceanography*, *8*(0), 1–12, doi:10.1016/j.mio.2014.03.001.

Stabeno, P. J., and E. C. Monahan (1986), The influence of whitecaps on the albedo of the sea surface, in *Oceanic Whitecaps and Their Role in Air-Sea Exchange Processes*, edited by E. C. Monahan and G. Mac Niocaill, pp. 261–266, Dordrecht, Holland.

Stramska, M., and T. Petelski (2003), Observations of oceanic whitecaps in the north polar waters of the Atlantic, *J. Geophys. Res.*, *108*(C3), 3086, doi:10.1029/2002JC001321.

Stramski, D., and J. Tegowski (2001), Effects of intermittent entrainment of air bubbles by breaking wind waves on ocean reflectance and underwater light field, *J. Geophys. Res.*, *106*(C12), 31345–31360, doi:10.1029/2000JC000461.

Stramski, D., R. A. Reynolds, M. Kahru, and B. G. Mitchell (1999), Estimation of particulate organic carbon in the ocean from satellite remote sensing, *Science*, *285*(5425), 239–242.

Sugihara, Y., H. Tsumori, T. Ohga, H. Yoshioka, and S. Serizawa (2007), Variation of whitecap coverage with wave-field conditions, *Journal of Marine Systems*, *66*(1), 47–60.

Terrill, E. J., W. K. Melville, and D. Stramski (1998), Bubble entrainment by breaking waves and their effects on the inherent optical properties of the upper ocean.

Terrill, E. J., W. K. Melville, and D. Stramski (2001), Bubble entrainment by breaking waves and their influence on optical scattering in the upper ocean, *J. Geophys. Res.*, *106*(C8), 16815–16823, doi:10.1029/2000JC000496.

Thorpe, S. A. (1982), On the Clouds of Bubbles Formed by Breaking Wind-Waves in Deep Water, and their Role in Air -- Sea Gas Transfer, *Philosophical Transactions of the Royal Society of London. Series A, Mathematical and Physical Sciences*, *304*(1483), 155–210.

Twardowski, M., X. Zhang, S. Vagle, J. Sullivan, S. Freeman, H. Czerski, Y. You, L. Bi, and G. Kattawar (2012), The optical volume scattering function in a surf zone inverted to derive sediment and bubble particle subpopulations, *J. Geophys. Res.*, *117*(C7), C00H17, doi:10.1029/2011JC007347.

Wang, Q., E. Monahan, W. Asher, and P. Smith (1995), Correlations of whitecap coverage and gas transfer velocity with microwave brightness temperature for plunging and spilling breaking waves, *Air-Water Gas Transfer*, 217–225.

Welschmeyer, N. A. (1994), Fluorometric analysis of chlorophyll a in the presence of chlorophyll b and pheopigments, *Limnology and Oceanography*, *39*(8), 1985–1992.

Whitlock, C. H., D. S. Bartlett, and E. A. Gurganus (1982), Sea foam reflectance and influence on optimum wavelength for remote sensing of ocean aerosols, *Geophys. Res. Lett.*, *9*(6), 719–722, doi:10.1029/GL009i006p00719.

Woolf, D. K. (2005), Parametrization of gas transfer velocities and sea-state-dependent wave breaking, *Tellus B*, *57*(2), 87–94, doi:10.1111/j.1600-0889.2005.00139.x.

Woolf, D. K., and S. A. Thorpe (1991), Bubbles and the air-sea exchange of gases in near-saturation conditions, *Journal of Marine Research*, *49*(3), 435–466, doi:10.1357/002224091784995765.

Wright, S., S. Jeffrey, and R. Mantoura (2005), *Phytoplankton pigments in oceanography: guidelines to modern methods*, Unesco Pub.

Wu, J. (1983), Sea-Surface Drift Currents Induced by Wind and Waves, *J. Phys. Oceanogr.*, *13*(8), 1441–1451, doi:10.1175/1520-0485(1983)013<1441:SSDCIB>2.0.CO;2.

Yount, D. E. (1982), On the evolution, generation, and regeneration of gas cavitation nuclei, *The Journal of the Acoustical Society of America*, *71*(6), 1473–1481.

Zaneveld, J. R. V., and H. Pak (1973), Method for the determination of the index of refraction of particles suspended in the ocean, *JOSA*, *63*(3), 321–324.

Zappa, C. J., M. L. Banner, H. Schultz, J. R. Gemmrich, R. P. Morison, D. A. LeBel, and T. Dickey (2012), An overview of sea state conditions and air-sea fluxes during RaDyO, *Journal of Geophysical Research: Oceans (1978–2012)*, *117*(C7).

Zhang, X., Marlon Lewis, M. Lee, B. Johnson, and G. Korotaev (2002), The Volume Scattering Function of Natural Bubble Populations, *Limnology and Oceanography*, *47*(5), 1273–1282.

Zhang, X., M. Lewis, W. P. Bissett, B. Johnson, and D. Kohler (2004), Optical Influence of Ship Wakes, *Appl. Opt.*, *43*(15), 3122–3132, doi:10.1364/AO.43.003122.

Zhang, X., L. Hu, and M.-X. He (2009), Scattering by pure seawater: effect of salinity, *Optics Express*, *17*(7), 5698–5710.

Zhang, X., M. Twardowski, and M. Lewis (2011), Retrieving composition and sizes of oceanic particle subpopulations from the volume scattering function, *Appl. Opt.*, *50*(9), 1240–1259.

Zhao, D., and Y. Toba (2001), Dependence of whitecap coverage on wind and wind-wave properties, *Journal of oceanography*, *57*(5), 603–616.

5 Epilogue

Evidence that small bubbles, generated by large-scale wave breaking, are present in the surface ocean and contribute to the magnitude and shape of ocean color reflectance has been presented in the preceding chapters. In an effort to estimate the contribution by bubbles, relative to other oceanic particle populations (*e.g.*, calcite, colloids, and phytoplankton), to reflectance or backscattered light in the Southern Ocean, a least-squares inversion technique was applied to surface measurements of the bulk optical volume scattering function. The results of the inversion were validated using field measurements of phytoplankton pigment concentrations, acid labile backscattering and the size-fractionated phytoplankton assemblage. The results are preliminary in their current form; future work includes analyzing the absolute, rather than relative, contribution by bubbles to backscattering under changing forcing conditions, and quantifying the uncertainty associated with the least-squares approach. This work serves to address the hypothesis that both biological and physical processes drive optical backscattering and reflectance. The least-squares inversion technique can provide an estimate of their respective contributions.

5.1 Background

Ocean color remote sensing has significantly advanced the knowledge of the Southern Ocean and its contribution to global biogeochemical cycles [*Longhurst et al.*, 1995; *Behrenfeld and Falkowski*, 1997; *Arrigo et al.*, 1998; *Stramski et al.*, 1999]. Differences in the spectral shape of reflectance can be observed from satellites and are routinely used to estimate the amount of Chlorophyll *a* (Chl), the predominant pigment in phytoplankton, in the ocean [*Dierssen*, 2010]. In the Southern Ocean in particular, many different relationships have been derived to quantitatively relate the spectral color to the amount of Chl for different regions and phytoplankton assemblages [*Mitchell and Holm-Hansen*, 1991; *Arrigo et al.*, 1998; *Dierssen and Smith*, 2000]. Such differences are commonly ascribed to pigment composition within the phytoplankton, which can influence light absorption, as well as the arrangement or packaging of pigments within the cells.

However, the color reflected from the ocean is not only related to the amount and spectral characteristics of light absorption by pigments, but also to the amount and type of backscattering material. For example, the amount of light leaving the water, herein referred to as remote sensing reflectance (R_{rs}), can be related to the backscattering from particles in the water column and biogeochemical parameters, including total suspended matter and particulate organic and inorganic carbon. Ocean color imagery and limited field data suggests the Southern Ocean has high R_{rs} compared to many other region of the world ocean. The "bright" waters characteristic of the Southern Ocean may be indicative of high levels of particulate backscattering. Reynolds *et al.* [2001] found that particulate backscattering in the polar front zone of the Southern Ocean was four times higher compared to waters in the more coastal Ross Sea sector. The source of high backscattering was attributed to elevated concentrations of unidentified small particles. Moreover, in the polar front zone, particulate organic carbon (POC) was found to be correlated to higher levels of backscattering compared to the Ross Sea [*Stramski et al.*, 1999]. Coastal waters can also have elevated reflectance due to the massive additions of glacial meltwater into the coastal ecosystem each summer [*Dierssen et al.*, 2002].

Another explanation for the highly reflective waters of Southern Ocean is the presence of coccolithophores and coccoliths, which are part of the calcite or particulate inorganic carbon (PIC) pool. Backscattering by detached coccoliths routinely accounts for 10-20% of the total backscattering in the world's oceans [*Balch et al.*, 1999]. During coccolithophore blooms, however, backscattering is greatly amplified and calcite can be responsible for over 90% of the total backscattering [*Balch et al.*, 1996]. The two-band, semi-analytical ocean color algorithm for retrieving estimates of PIC from ocean color uses the magnitude of normalized water leaving radiance (*nLw*) in the blue (443 nm) and green (555 nm) wavelengths [*Balch et al.*, 2005]. This algorithm consistently shows the Southern Ocean to have some of the highest calcite concentrations in the world's oceans and has been dubbed the "Great Calcite Belt" [*Balch et al.*, 2011]. When applied to the above water reflectance measurement collected in the Atlantic

sector of the Southern Ocean, however, the PIC generated estimates were 2-3x the PIC measured in the water column [*Balch et al.*, 2011]. It was hypothesized that microbubble populations, at least in part, contributed the additional scattering that was misallocated as PIC.

High backscattering in the Southern Ocean may be associated with the consistently high winds that flow from the west unimpeded by continental landmasses. Climatological wind speeds in the region during the austral summer are 10 ± 3 m s^{-1} with mean wave heights of 3 m. High winds cause whitecaps and bubble entrainment by breaking waves that can significantly impact ocean color remote sensing. Whitecaps and foam elevate the amount of upward reflected photons from the sea surface. Bubbles entrained in the water column are effective at scattering light because their refractive index is significantly less than that of the surrounding medium [*Marston and Kingsbury*, 1981; *Stramski*, 1994; *Terrill, et al.*, 2001]. Remote sensing reflectance can be significantly enhanced due to bubble entrainment at temporal scales of minutes and the spectral nature of the light field can be shifted towards green wavelengths [*Stramski and Tegowski*, 2001; *Zhang, et al.*, 2004; *Zhang, et al.*, 1998]. If the Southern Ocean is prone to chronic high winds, then background levels of bubbles may contribute to overall enhanced reflectance.

Bubbles in natural waters tend to be coated by dissolved organic material (DOC) because the bubble-water interface minimizes the energy required of the DOC to remain in solution. Such coatings can weaken forward scattering and enhance the backscattering efficiency by as much as 4 times [*Zhang, et al.*, 2004; *Zhang, et al.*, 1998]. Organic coatings can also increase the residence time of bubbles in the water column [*Johnson and Cooke*, 1981] as well as generate particulate organic carbon (POC) [*Johnson and Cooke*, 1980, 1981; *Monahan and Dam*, 2001]. A strong correlation has been found between the size spectra of POC in seawater and the bubbles that facilitate POC formation [*Johnson and Cooke*, 1980]. Most previous measurements of bubbles have been made acoustically of the bubble fraction greater than 10 um, which may not be the fraction responsible for most of the backscattering. A hypothetical extension of the bubble size distribution to 0.1 μm, where the Junge size distribution slope followed an

exponent of -4, elicited a doubling of the backscattering ratio (backscattering/total scattering). Recent optical measurements show microbubble populations extending to sizes at least as small as 2 μm radius [*Randolph et al.*, 2014].

Here, these hypotheses are explored using *in situ* data collected in conjunction with the Southern Ocean Gas Exchange Experiment along the polar front zone of the Atlantic sector of the Southern Ocean. The sources of particulate backscattering were investigated using measurements of the volume scattering function, which describes the angular distribution of scattered light (*e.g.*, Petzold [1972], Lee and Lewis [2003] Twardowski, and Zhang [2002]). In theory, the scattering properties (*i.e.*, VSF) of a particle population suspended in water can be determined if the concentration, composition, shape, and size of the particles are known. Therefore, the VSF can be inverted to estimate the composition and size distribution of the particulate material present (*e.g.*, Brown and Gordon [1973], Zaneveld and Pak [1973], Zhang *et al.* [2002], Zhang *et al.* [2011]). Here, particle populations ranging from 0.1 to 100 μm in radius and with varying indices of refraction were investigated a least-squares inversion technique applied to measurements of the bulk optical volume scattering function. The resulting particle populations identified using the model are grouped into candidate particle types representative of oceanic particles, including populations of bubbles, colloids, coccolithophores and coccoliths, and diatoms. These data are used to estimate the biological and physical sources of optical backscattering in the highly reflective Southern Ocean.

5.2 Methodology

This investigation was conducted on the NOAA ship the *R.V. Ronald H. Brown* in the Atlantic sector of the Southern Ocean between the Polar Front (PF) and the Southern Antarctic Circumpolar Current Front (SACCF), nominally 50°S 40°W, during austral summer, March - April 2008 (Figure 1a). A Lagrangian approach was taken to study gas transfer at high wind speeds and two tracer patches were deployed lasting 6 and 15 days in duration, respectively [*Ho et al.*, 2011]. Optical measurements were collected

during wind conditions ranging from 3 to 15 m s^{-1} at 10 total stations within patches 2 and at a single station located 300 km north of South Georgia Island. A thorough analysis of a subset of the SOGasEx dataset is presented contrasting stations sampled during high wind conditions with stations sampled during low wind conditions (Figure 1b).

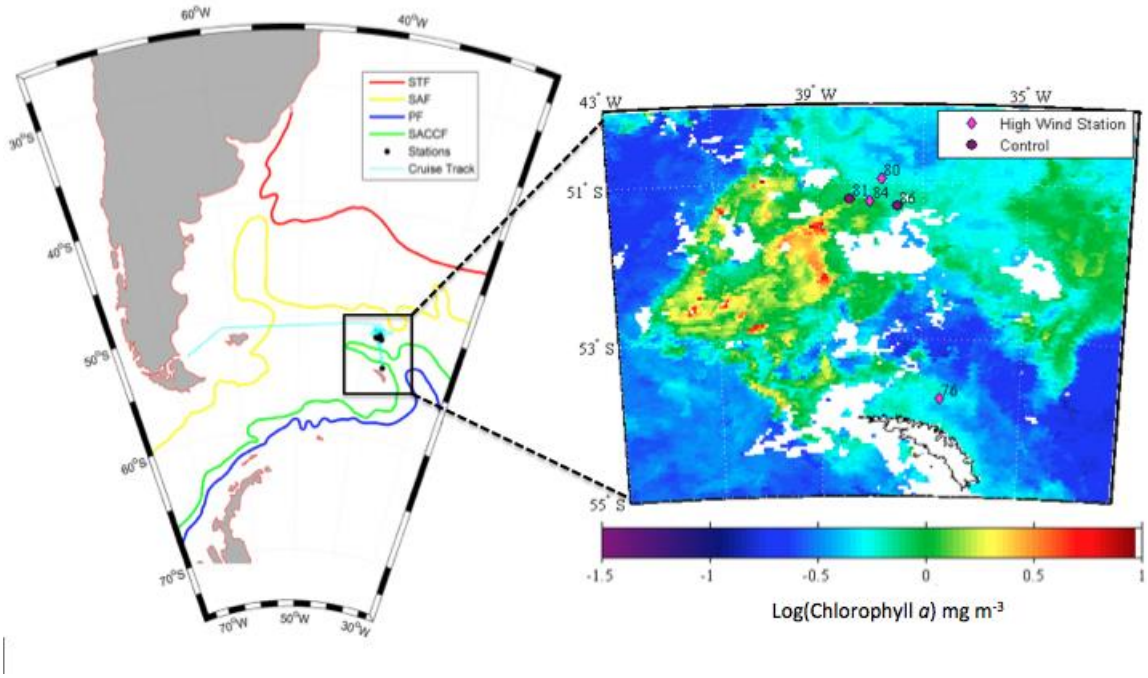

Figure 1: (a) The South Atlantic sampling region, cruise track (blue line), and stations locations (black circles) for the Southern Ocean Gas Exchange Experiment (SOGasEx) (b) A subset of the SOGasEx dataset to be analyzed here (labeled with the yearday), including three stations sampled during high wind conditions (pink diamonds) and two stations sampled during low wind conditions (purple circles), is overlaid on the satellite-derived average chlorophyll *a* (mg m^{-3}) from the MODIS Aqua sensor (nominal 4 km resolution) for the month of March 2008.

5.2.1 Measurements of the volume scattering function and inversion technique

Profiles were conducted close to noon daily in the center of the patch area to measure a suite of optical properties during SOGasEx, including the volume scattering function (VSF; $\beta(\theta)$, using a MASCOT (Multi-Angle SCattering Optical Tool, WET Labs). The VSF describes the angular distribution of

scattered light, following $I(\theta)/EdV$ ($m^{-1}sr^{-1}$), where I (sr^{-1}) is the scattered intensity in the direction θ by the volume dV and E (W m^2) is incident irradiance. The particulate contribution to the VSF, $\beta_p(\theta)$, is determined by removing the effects of seawater following Zhang *et al.* [2009]. Finally, the particulate backscattering coefficient, b_{bp} (m^{-1}) describes the amount of light scattered by particles in the water column into the backward direction following $2\pi \int_{\pi/2}^{\pi} \sin(\theta)\,\beta(\theta)d(\theta)$. The MASCOT measures scattering at 17 angles between 10° and 170° (in 10° increments) at high frequency (20 Hz). Estimates of particulate backscattering were determined from MASCOT measurements of $\beta_p(\theta)$, binned to 1 Hz, by interpolating $2\pi\beta_p(\theta)\sin(\theta)$ to 1° and integrating from 90 to 180, where sin(180)=0. Details of the MASCOT design, calibration, and processing procedures can be found in Sullivan and Twardowski [2009] and Twardowski *et al.* [2012].

The size distribution and scattering contribution of each particle subpopulation present was estimated using an inversion technique, based on a linear least squares algorithm, applied to bulk measurements of the volume scattering function following Zhang *et al.* [2011]. The total particulate volume scattering function is the linear sum of scattering from subpopulations with a given refractive index, shape, structure, concentration, and size distribution, where the location of the size distribution peak (r_{mode}) and the real part of the index of refraction (n_r) are the primary determinants of the VSF shape (see Zhang *et al.* [2011] Twardowski *et al.* [2012]). By inverting the Fredholm linear integral equation with the use of a kernel function, a set of size distributions and refractive indices for several particle subpopulations were retrieved from measurements of the VSF [*Zhang et al.*, 2011]. The kernel function constructed by Zhang *et al.* [2011] and used here was built using Lorenz-Mie theory modeling (*i.e.*, particles are assumed to be spherical and microbubbles are coated with a 2 nm lipid-type monolayer), assuming lognormal particle size distributions with size limits (radii from 0.001 to 300 μm) and refractive indices (1 to 1.20 and 0.75 for bubbles) characteristic of oceanic particles (see Zhang *et al.* [2011], Table 3 and Figure 3). The peak of the lognormal particle size distributions for subpopulations was allowed to vary between 0.01 and 10

μm (σ~0.1 to 1.6) The validity and consequences of applying the assumptions used to build the kernel are tested and discussed at length in Zhang *et al.* [2011] and Twardowski *et al.* [2012].

The inversion produces estimates of the characteristic size distributions (*e.g.*, mode size and standard deviation) and indices of refraction for 10 to 12 particle subpopulations and their associated VSFs. Ultimately, the resulting particle subpopulations are aggregated when appropriate (*i.e.*, based on their size distribution and refractive index) and are presented as a candidate particle types (*e.g.*, coccolithophores and coccoliths, phytoplankton, bubbles, and colloids). The effectiveness of the VSF inversion technique in resolving particle populations is assessed using independent optical and analytical measurements of particle populations, including the contribution of PIC to backscattering, coccolith and coccolithophore enumeration, the presence of bubbles, and the composition of the phytoplankton assemblage (*i.e.*, size-fraction and accessory pigments).

5.2.2 Validation dataset

Analytical and optical measurements of particulate populations were collected for comparison to the subpopulations resolved using the VSF inversion. Discrete measurements of chlorophyll *a* and total suspended material were made from surface water samples collected at each station. Chlorophyll *a* was extracted and determined fluorometrically from filtered surface water samples according to Wright *et al.* [2005] and Welschmeyer [1994] and measured in triplicate for most stations [*Lance et al.*, 2012a]. For several stations, the size-fractionated phytoplankton contribution to the total chlorophyll concentration was determined. Three operationally defined size classes, including picoplankton (< 2 μm), nanoplankton (2 to 20 μm) and microplankton (>20 μm) were differentiated using polycarbonate filters with 2-20 μm pore sizes [*Lance et al.*, 2012a]. Phytoplankton pigments were determined from filtered water samples using accepted HPLC methods following Hooker *et al.* [2005]. The presence of major diagnostic pigments, including fucoxanthin (*e.g.*, FUCO, diatoms) and 19'hexanoyloxyfucoxanthin (*e.g.*, HEXA, primnesiophytes) and peridinin (e.g., PERI, dinoflagellates), is reported.

Calcite, a birefringent material produced by coccolithophores, also contributes significantly to scattering when present [*Balch et al.*, 2011]. Acid labile backscattering, b_{bp}', calculated as the difference between raw backscattering and backscattering after the addition of acid, which dissolves calcite, was measured by *Balch et al.* [2011] following Balch *et al.* [2001] using an ECO-VSF (WET Labs). Acid labile backscattering is presented here as the mean percent contribution of b_{bp}' to the total b_{bp} measured during the time-series at each station. A detailed description of the coccolithophorid and coccoliths populations measured during SOGasEx can be found in Balch *et al.* [2011].

The presence of foam and bubble populations was quantified using measurements of fractional whitecap coverage. Whitecap coverage estimates from high-resolution digital imagery and using radiometry, which captures more of the decaying bubble plume, are reported (see Chapter 3). The vertical extent of bubble populations was estimated using measurements of acoustic backscatter (120 kHz) over 15 m of the water column. The Acoustic Doppler Current Profiler (ADCP), deployed on a drifting, autonomous MAPCO$_2$ Buoy, collected data at high sampling frequency (20 Hz) in 75 bins, each 25 cm. The portion of the signal attributable to bubbles, referred to as the acoustic backscatter anomaly, was determined by the removal of the mean signal of backscatter known to be bubble free [Zappa, pers. comm.]. Finally, meteorological data, including the neutral wind speeds at the reference height of 10 m (U_{10}), were measured using an air-sea flux package deployed on the jack-staff of the ship [*Edson et al.*, 2011]. A detailed description of the mixed layer and physical dynamics measured during SOGasEx is presented in Ho *et al.* [2011].

5.3 Results and Discussion

Analytical and optical measurements from discrete samples indicated the presence of particulate populations varying in quantity and composition (table 1). Substantial differences in hydrography, total suspended matter, backscattering and the types of phytoplankton present in the water column were

observed within patch 2 (days 80-95). Samples from within patch 2 (51.3°S, 37.7°W) were in 4-5°C water, where average wind speeds ranged from 3 to 15 m s^{-1}. High winds and large significant wave heights resulted in intense, deep-going bubble plumes at four stations within patch 2. Measurements of total suspended material (0.31 to 1.27 g m^{-3}) suggested a large range in particulate loading during the experiment. The chlorophyll values ranged from 0.34 to 0.91 mg m^{-3} throughout the 15-day period [*Lance et al.*, Submitted] where initially, the phytoplankton contribution to chlorophyll was nanoplankton dominanted (54%) and the remaining fraction was comprised of near equal parts of pico and microplankton. Late in the patch, pico and nanoplankton were dominant with scarcely any microplankton present (8%). Throughout the lifetime of the patch, the diatom dominated phytoplankton assemblage (FUCO:HEXA~3.5) transitioned towards an even diatom-coccolithophore community (FUCO:HEXA~1.4). On the final day, an increase in the presence of dinoflagellates occurred.

The South Georgia Island (53.8°S and 36.6°W) waters were colder, ~3°C and the average wind speed measured 12.4 to 13.4 m s^{-1}. These stations exhibited the highest reported amounts of total suspended material (3.88 g m^{-3}). Furthermore, the total absorption by dissolved and particulate material was significantly higher at this location, likely due to the presence of particulates from glacial meltwater off of the neighboring island (*i.e.*, glacial flour, see Dierssen and Smith [2000]). Bubble populations were observed in the optical data collected from this station.

Table 1: Physical, biological and optical measurements from discrete water samples collected in the Southern Ocean, including the mean neutral wind speed (at 10 m) for the sampling period (U_{10}, m s^{-1}), fractional whitecap coverage from high resolution digital imagery and radiometry (*W*, dimensionless), chlorophyll *a* concentration (Chl, mg m^{-3}), size-fractionated chlorophyll (including pico, nano and microplankton in %), phytoplankton pigment concentrations from HPLC (mg m^{-3}), total suspended material (TSM; g m^{-3}), acid labile backscattering (b_{bp}', %). Empty fields indicate no data. An in-depth analysis is provided for the stations in bold.

Station Day of year	**Depth** of measure-ment (m)	**U_{10}** (m s^{-1})	***W*** *Rad.* *DI*	**Chl** (mg m^{-3})	**Size fraction**[2] (% pico, nano, micro)	**Pigments**[2] Total, FUCO, HEXA, PERI	**TSM** (g m^{-3})	**b_{bp}'**[1] (% of the total b_{bp})
76	**1.5**	**13.8**	**0.032** **0.007**	**0.47**[c]			**3.88**	
80	**5.2**	**11.1**	**0.009**	**0.65**			**1.27**	**7%** **±6**
81	**3.1**	**4.6**		**0.34**[c]			**1.19**[1]	
82	3.4	10.5	0.012 0.010	0.91		1.96, 0.43 0.12, 0.02	1.19	13% ±7
84	**3.1**	**13.0**	**0.012** **0.037**	0.72 [c]	**22, 54** **24**		**0.55**	**23%** **±11**
86	**1.5**	**3.1**	**<0.001** **<0.001**	0.72[c]	**13[a], 52** **35**		**0.60**	**18.5%** **±7**
87	4.9	5.9	0.007	0.41		0.81[b], 0.13 0.08, 0.02	0.42	18% ±6
90	5.3	9.0	0.005 0.011	0.49			0.47	31% ±7
92	5.1	5.8	0.003	0.48	8[b], 42 50		0.31	31% ±8
94	3.3	4.9	<0.001 0.002	0.54			0.55	34% ±14
95	4.2	8.4	0.012 0.002	0.57		1.19[b], 0.19 0.11, 0.024	0.39	30% ±7

[1]Measurements from Balch *et al.* [2011]

[2]Measurements from Lance *et al.* [2012b]

[a]Collected one day previous at the same location

[b]Collected one day after with same Chlorophyll concentration

[c]Chlorophyll calculated using remote sensing reflectance following O'Reilly *et al.* [2000]

5.3.1 VSF classification of particle populations

The least squares inversion produced 9 to 13 unique particle subpopulations from the bulk VSF measurements. The VSFs (panel 1, identified using n_r) of the individual subpopulations, their size distributions (panel 2, identified using r_{mode} and r_σ) and the contribution of each to the particulate backscattering are shown in Appendix A. Colors are assigned to each subpopulation according to the index of refraction (*e.g.*, shades of blue are used for populations with n_r=0.75). Reconstruction of the VSF from the subpopulations resolved using the inversion is in good agreement with the original measured VSF (Appendix A, panel 1j, red dashed line).

In general, the most significant contributors to particulate backscattering include particles very small in size, O(0.01) or with low water content (*i.e.*, high n_r or n_r=0.75). Preliminary results from the VSF inversion suggest that the very small particle (VSP) subpopulation (mode d~ 0.02-0.08, n~1.06) contributed as much a 75% (days 82 and 87) of the total particulate backscattering and 50% on average (*e.g.*, Figure 1c, Figure 2f). This result is consistent with the estimate of Zhang *et al.* [2011] using the inversion technique and laboratory measurements of particulate concentrations (Wells).

According to the VSF inversion, the hardest particle populations (n_r~1.14-1.20) contributed between 3% and 22% of the total b_{bp}. Generally, two to three hard-particle subpopulations were resolved from each bulk VSF measurement including the following: a narrow size distribution (σ~0.1) with a small mode size (~0.8 μm) and n_r~1.14, a slightly broader size distribution (0.3) with the same mode size and a n_r~1.20, and a broad (σ~1.1) size distribution with a large mode size (~10 μm) and n_r~1.20. The composition and size distributions of these particle populations are consistent with those found for coccolithophores (mode size~10μm) and detached coccoliths (~0.1 μm) [*Balch et al.*, 1999; *Jonasz and Fournier*, 2011].

As many as four bubble-type populations (n_r=0.75) were present during SOGasEx and collectively

contributed as much as 25% to the total particulate backscattering. For all stations, the VSF inversion resolved a narrow bubble size distribution (σ~0.1) centered at r_{mode}~0.2 µm. This subpopulation alone contributed between 2 and 24% of the b_{bp}. Often (8 out of 10 stations), another narrow (σ~0.1) subpopulation with a similar, small mode size (0.4 µm) was present (see Appendix A). For two stations (*i.e.*, days 90 and 94), a third slightly broader (σ~0.3) subpopulation, also centered at 0.2 µm radius, accounted for 4-5% of the b_{bp}. Finally, a fourth bubble population with a broad (σ~0.9) size distribution centered near ~0.2 µm was resolved during days with high wind conditions (*e.g.*, days 80, 84, 90 and 94) (Figure 2). Even in high concentrations, this subpopulation generally only contributed ~1% of the total particulate backscattering.

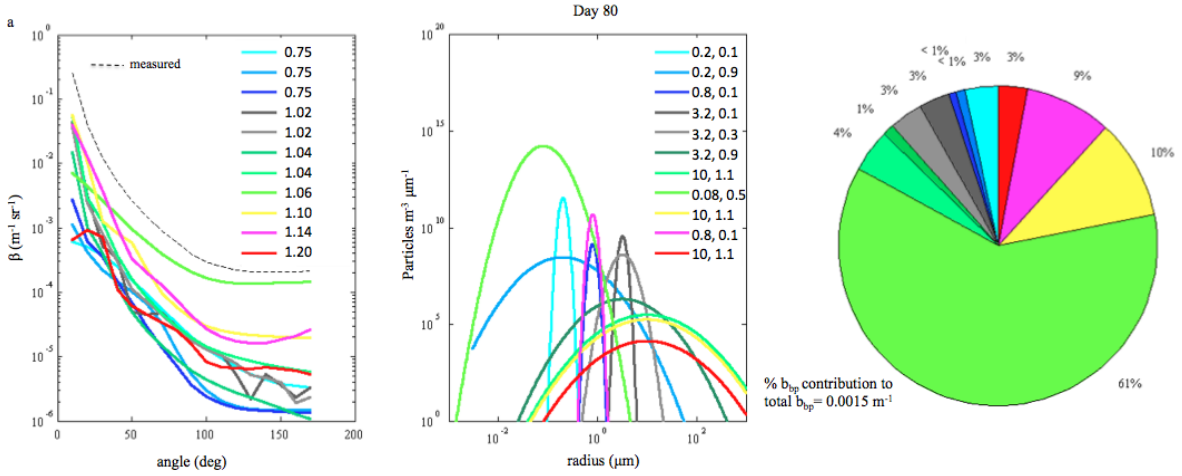

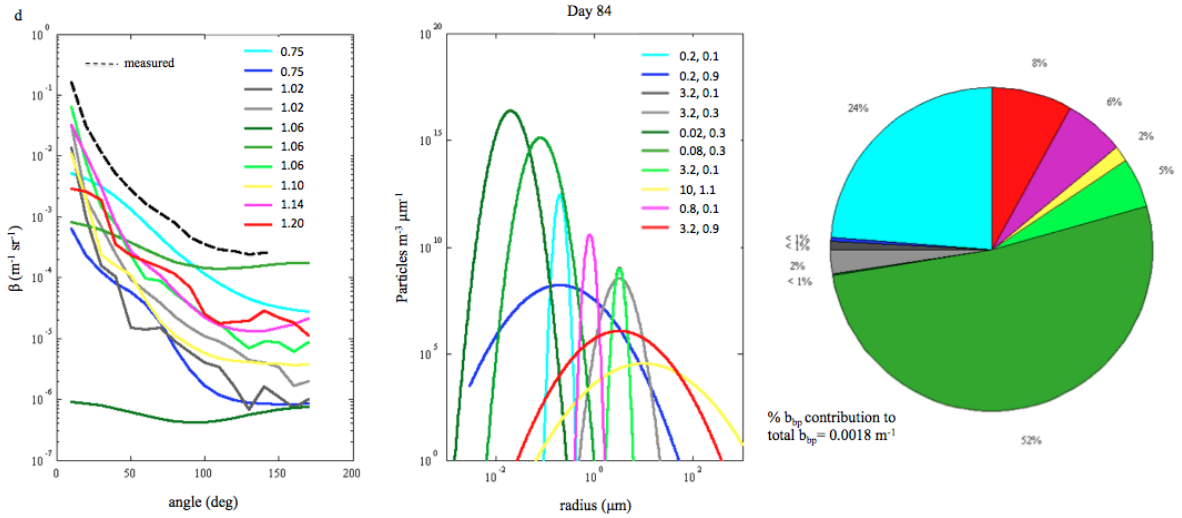

Figure 2: The VSFs (panel 1, identified using n_r) and size distributions (panel 2, identified using r_{mode} and r_σ) of individual subpopulations determined by inversion of the bulk VSF (panel 1, dashed line) measured during high wind conditions (9 - 13 m s^{-1}) and the contribution of each subpopulation to backscattering (panel 3, %). Colors are assigned according to n_r (*e.g.*, shades of blue are used for populations with n_r=0.75).

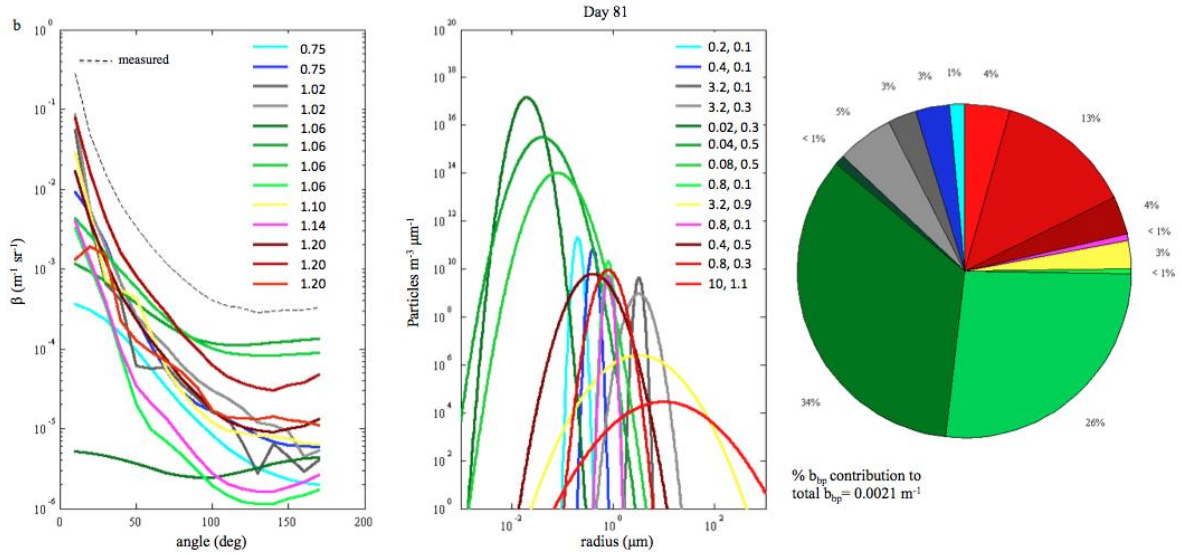

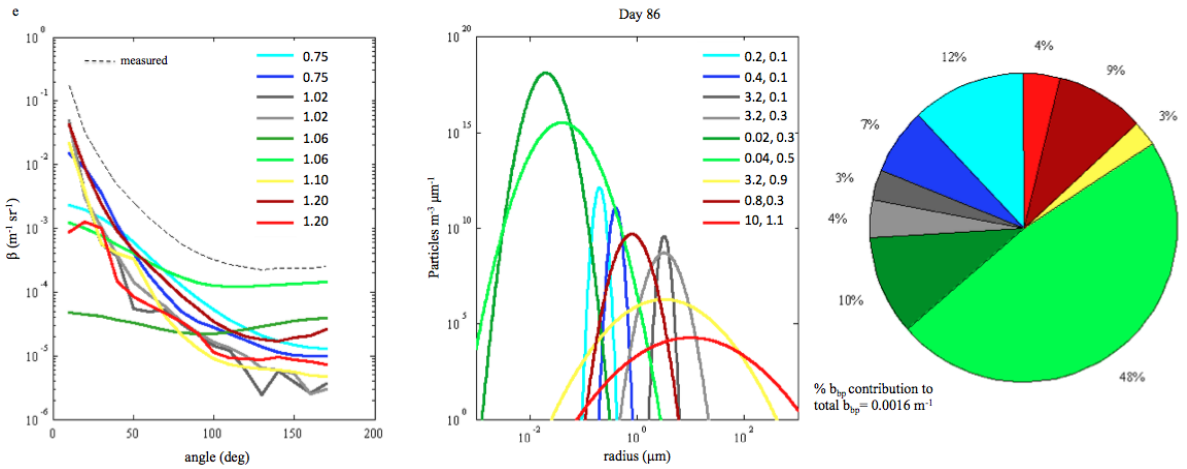

Figure 3: The VSFs (panel 1, identified using n_r) and size distributions (panel 2, identified using r_{mode} and r_σ) of individual subpopulations determined by inversion of the bulk VSF (panel 1, dashed line) measured during high wind conditions (3 - 5 m s^{-1}) and the contribution of each subpopulation to backscattering (panel 3, %).

To assess the relative contribution of bubbles to backscattering in the Southern Ocean, particle subpopulations were aggregated when appropriate (*i.e.*, based on n_r and r_{mode}) and presented as a candidate particle types (*e.g.*, coccolithophores and coccoliths, phytoplankton, bubbles, and colloids) for each station. A subset of stations collected in close succession but subject to different wind forcing were selected for comparison. The relative role of bubbles in the backscattering of a particulate population is easily determined using Days 84 and 86, stations with similar water column properties (*e.g.*, particulate backscattering of 0.0018 m^{-1} and 0.0016 m^{-1}), sampled under markedly different wind conditions (~13 and 3 m s^{-1}) (Figure 4b and d). Although Days 80 and 81 show dissimilar particulate compositions (b_{bp} ~ 0.0015 and 0.0021 m^{-1} and Chl~0.65 and 0.34 mg m^{-3}), the influence of wind (~11 and 4 m s^{-1}) on retrievals of bubbles is evident in the comparison (Figure 4a and c).

The sampling method employed here (*i.e.*, profile deployment) cannot capture the contribution of clouds of large bubbles formed by breaking waves. However, the inversion technique resolved a large bubble

population that contributed an average of approximately 1% to b_{bp} during high wind conditions (Figure 4a and b) and disappear during low wind conditions (Figure 4c and d). A persistent, small bubble population with a narrow size distribution contributed between 3% and 20% of the total b_{bp} (Figure 4). The submicron bubble population appears to persist for at least a day after high winds. For example, this persistent bubble population contributed 5% and 19% of the total backscattering on the days following high conditions (Figure 4c and d). A substantial portion of this bubble population are decayed, wind-generated bubbles. The submicron population of persistent bubbles present at all stations is likely cavitation nuclei, which are ubiquitous throughout the ocean [*Yount*, 1982; *Zhang et al.*, 2002; *Twardowski et al.*, 2012].

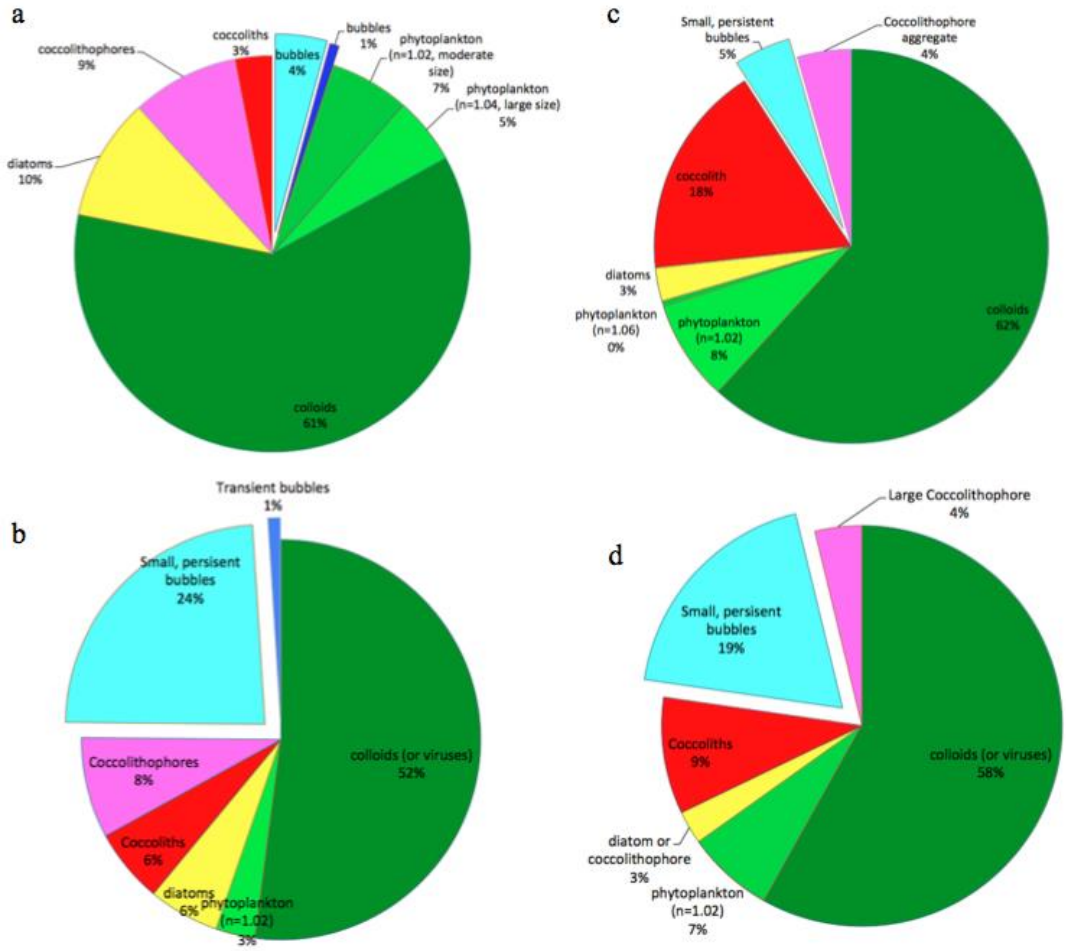

Figure 4: Particle subpopulations resolved using the bulk volume scattering function measured in the surface water of stations experiencing (a, b) high (days 80 and 84) and (c, d) low (days 81 and 86) wind conditions. Particle subpopulations were grouped according to candidate particle type using the resolved mode size and refractive index.

5.4 Future directions for the quantification of the bubble signal in remote sensing of ocean color and uncertainty analysis

The results presented here are preliminary, however, initial analysis of Southern Ocean data using the least-squares inversion technique applied to surface measurements of the bulk optical volume scattering function suggest that persistent, very small bubble populations with a narrow size distribution and small mode size (r~0.2 μm) could be contributing between 5% and 20% of the total backscattering in the Atlantic sector of the Southern Ocean. A standing stock of decayed, wind-generated bubbles in the Southern Ocean could be contributing ~5% of the total backscattering days after high winds have subsided. The results are preliminary in their current form; a rigorous quantification of uncertainty associated with the least-squares approach is required. The inversion results presented here will be further analyzed in concert with independent optical, acoustic and analytical measurements of particle populations in an effort to validate the backscattering partitioning. Ultimately, these analyses will lead to a well-validated backscattering budget for the Atlantic sector of the Southern Ocean under a large range of wind and wave conditions. The contribution of each particle subpopulation to reflectance will be investigated with the goal of understanding reflectance measured at the satellite.

Appendix A: The volume scattering inversion results for ten Southern Ocean stations

The volume scattering functions (VSF; panel 1, identified using n_r) and size distributions (panel 2; identified using the mode and standard deviation of the size distribution, r_{mode} and r_σ) of individual subpopulations determined by inversion of the bulk volume scattering function (panel 1, dashed line) measured at 10 stations during the Southern Ocean Gas Exchange Experiment and the contribution of

each subpopulation to backscattering (panel 3, %). Colors are assigned according to the refractive index, n_r. Reconstruction of the VSF from the subpopulations resolved using the inversion is in good agreement with the original measured VSF (panel 1j, red dashed line).

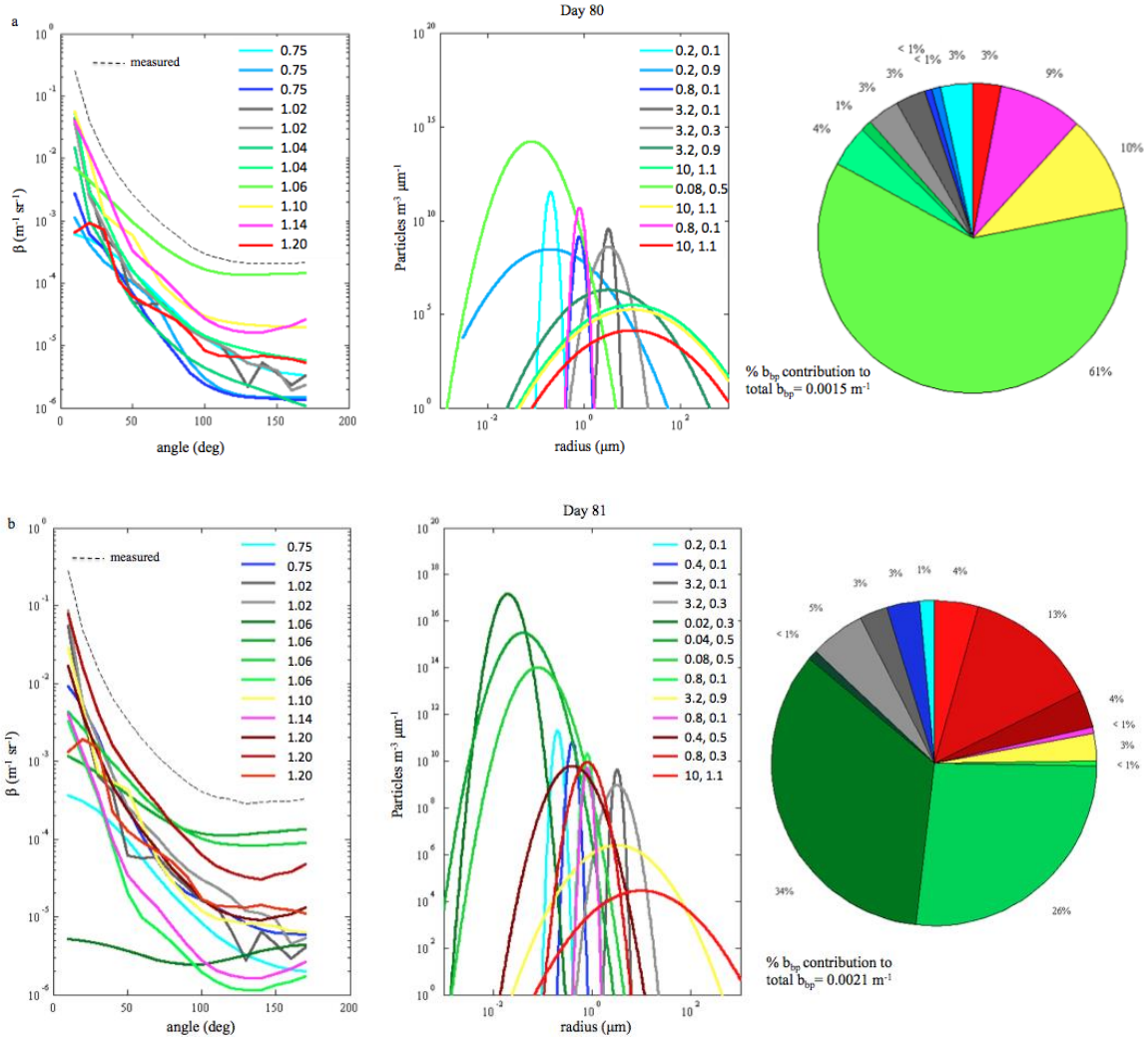

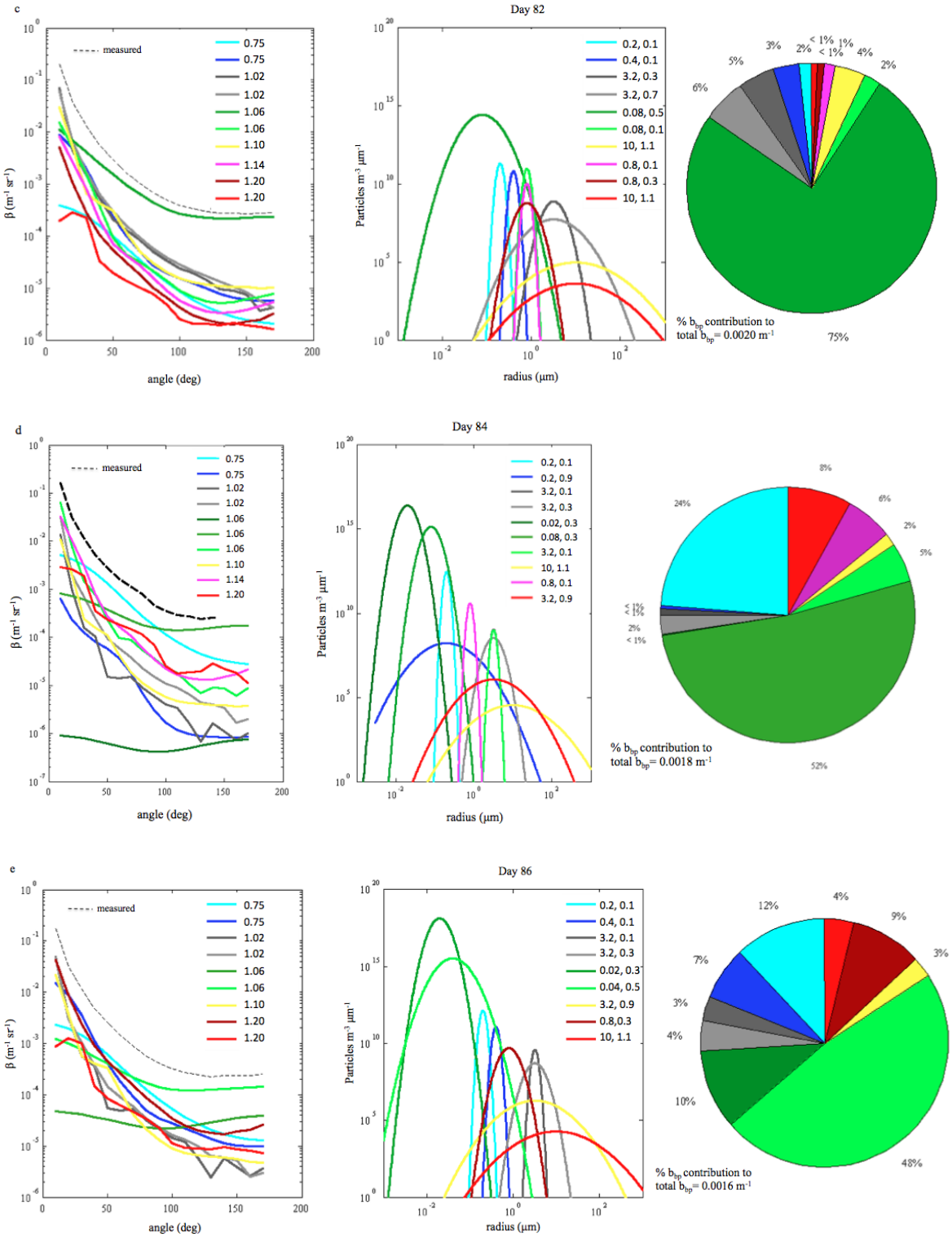
c
measured
0.75
0.75
1.02
1.02
1.06
1.06
1.10
1.14
1.20
1.20
β (m⁻¹ sr⁻¹)
angle (deg)
Day 82
0.2, 0.1
0.4, 0.1
3.2, 0.3
3.2, 0.7
0.08, 0.5
0.08, 0.1
10, 1.1
0.8, 0.1
0.8, 0.3
10, 1.1
Particles m⁻³ µm⁻¹
radius (µm)
% b_bp contribution to total b_bp = 0.0020 m⁻¹
75%
6%
5%
3%
2%
< 1%
< 1%
4%
2%
d
measured
0.75
0.75
1.02
1.02
1.06
1.06
1.06
1.10
1.14
1.20
β (m⁻¹ sr⁻¹)
angle (deg)
Day 84
0.2, 0.1
0.2, 0.9
3.2, 0.1
3.2, 0.3
0.02, 0.3
0.08, 0.3
3.2, 0.1
10, 1.1
0.8, 0.1
3.2, 0.9
Particles m⁻³ µm⁻¹
radius (µm)
% b_bp contribution to total b_bp = 0.0018 m⁻¹
52%
24%
8%
6%
2%
5%
2%
< 1%
< 1%
< 1%
e
measured
0.75
0.75
1.02
1.02
1.06
1.06
1.10
1.20
1.20
β (m⁻¹ sr⁻¹)
angle (deg)
Day 86
0.2, 0.1
0.4, 0.1
3.2, 0.1
3.2, 0.3
0.02, 0.3
0.04, 0.5
3.2, 0.9
0.8,0.3
10, 1.1
Particles m⁻³ µm⁻¹
radius (µm)
% b_bp contribution to total b_bp = 0.0016 m⁻¹
48%
10%
4%
3%
7%
12%
4%
9%
3%

References

Andreas, E. L., J. B. Edson, E. C. Monahan, M. P. Rouault, and S. D. Smith (1995), The spray contribution to net evaporation from the sea: A review of recent progress, *Boundary-Layer Meteorology*, *72*(1-2), 3–52.

Arrigo, K. R., D. Worthen, A. Schnell, and M. P. Lizotte (1998), Primary production in Southern Ocean waters, *J. Geophys. Res.*, *103*(C8), 15587–15600, doi:10.1029/98JC00930.

Asher, W., J. Edson, W. Mcgillis, R. Wanninkhof, D. T. Ho, and T. Litchendor (2002), Fractional Area Whitecap Coverage and Air-Sea Gas Transfer Velocities Measured During GasEx-98, in *Gas Transfer at Water Surfaces*, pp. 199–203, American Geophysical Union.

Austin, R. (1974), Inherent spectral radiance signatures of the ocean surface, *Ocean color analysis*, *7410*, 1–20.

Bailey, S. W. (2009), *Whitecap Reflectance*, NASA Ocean Biology Processing Group.

Balch, W. M., K. A. Kilpatrick, and C. C. Trees (1996), The 1991 coccolithophore bloom in the central North Atlantic. 1. Optical properties and factors affecting their distribution, *Limnol. Oceanogr.*, *41*(8), 1669–1683, doi:10.4319/lo.1996.41.8.1669.

Balch, W. M., D. T. Drapeau, T. L. Cucci, R. D. Vaillancourt, K. A. Kilpatrick, and J. J. Fritz (1999), Optical backscattering by calcifying algae: Separating the contribution of particulate inorganic and organic carbon fractions, *Journal of Geophysical Research: Oceans (1978–2012)*, *104*(C1), 1541–1558.

Balch, W. M., H. R. Gordon, B. C. Bowler, D. T. Drapeau, and E. S. Booth (2005), Calcium carbonate measurements in the surface global ocean based on Moderate-Resolution Imaging Spectroradiometer data, *J. Geophys. Res.*, *110*(C7), C07001, doi:10.1029/2004JC002560.

Balch, W. M., D. T. Drapeau, B. C. Bowler, E. Lyczskowski, E. S. Booth, and D. Alley (2011), The contribution of coccolithophores to the optical and inorganic carbon budgets during the Southern Ocean Gas Exchange Experiment: New evidence in support of the "Great Calcite Belt" hypothesis, *J. Geophys. Res.*, *116*, C00F06, doi:10.1029/2011JC006941.

Behrenfeld, M. J., and P. G. Falkowski (1997), Photosynthetic rates derived from satellite-based chlorophyll concentration, *Limnology and oceanography*, *42*(1), 1–20.

Bondur, V., and E. Sharkov (1982a), Statistical characteristics of foam formations on a disturbed sea-surface, *Okeanologiya*, *22*(3), 372–379.

Bondur, V. G., and E. A. Sharkov (1982b), Statistical properties of whitecaps on a rough sea, *Oceanology*, *22*(3), 274–279.

Bortkovskii, R., and V. Novak (1993), Statistical dependencies of sea state characteristics on water temperature and wind-wave age, *Journal of marine systems*, *4*(2), 161–169.

Bortkovskii, R. S. (1987), *Air-sea exchange of heat and moisture during storms*, Kluwer Boston Inc., Hingham, MA.

Bouguet, J.-Y. (2004), *Camera calibration toolbox for matlab*, MRL - Intel Corp.

Briggs, N., M. J. Perry, I. Cetinić, C. Lee, E. D'Asaro, A. M. Gray, and E. Rehm (2011), High-resolution observations of aggregate flux during a sub-polar North Atlantic spring bloom, *Deep Sea Research Part I: Oceanographic Research Papers*, *58*(10), 1031–1039.

Brown, O. B., and H. R. Gordon (1973), Two component Mie scattering models of Sargasso Sea particles, *Applied optics*, *12*(10), 2461–2465.

Callaghan, A. H. (2013), An improved whitecap timescale for sea spray aerosol production flux modeling using the discrete whitecap method, *J. Geophys. Res. Atmos.*, *118*(17), 9997–10,010, doi:10.1002/jgrd.50768.

Callaghan, A. H., and M. White (2009), Automated processing of sea surface images for the determination of whitecap coverage, *Journal of Atmospheric and Oceanic Technology*, *26*(2), 383–394.

Carder, K., and R. Steward (1985), A remote-sensing reflectance model of a red-tide dinoflagellate off west Florida1, *Limnology and Oceanography*, *30*(2), 286–298.

Cifuentes-Lorenzen, A., J. B. Edson, C. J. Zappa, and L. Bariteau (2013), A Multisensor Comparison of Ocean Wave Frequency Spectra from a Research Vessel during the Southern Ocean Gas Exchange Experiment, *J. Atmos. Oceanic Technol.*, doi:10.1175/JTECH-D-12-00181.1.

Dierssen, H. M. (2010), Perspectives on empirical approaches for ocean color remote sensing of chlorophyll in a changing climate, *Proceedings of the National Academy of Sciences*, *107*(40), 17073–17078.

Dierssen, H. M., and R. C. Smith (2000), Bio-optical properties and remote sensing ocean color algorithms for Antarctic Peninsula waters, *J. Geophys. Res.*, *105*(C11), 26301–26312, doi:10.1029/1999JC000296.

Dierssen, H. M., R. C. Smith, and M. Vernet (2002), Glacial meltwater dynamics in coastal waters west of the Antarctic peninsula, *Proceedings of the National Academy of Sciences*, *99*(4), 1790–1795.

Donelan, M., M. S. LONGUET-HIGGINS, and J. S. TURNER (1972), Periodicity in Whitecaps, *Nature*, *239*(5373), 449–451, doi:10.1038/239449a0.

Fairall, C. W., E. F. Bradley, J. E. Hare, A. A. Grachev, and J. B. Edson (2003), Bulk Parameterization of Air–Sea Fluxes: Updates and Verification for the COARE Algorithm, *J. Climate*, *16*(4), 571–591, doi:10.1175/1520-0442(2003)016<0571:BPOASF>2.0.CO;2.

Flatau, P. J., M. Flatau, J. R. V. Zaneveld, and C. D. Mobley (2000), Remote sensing of bubble clouds in sea water, *Q.J.R. Meteorol. Soc.*, *126*(568), 2511–2523, doi:10.1002/qj.49712656808.

Franz, B. A. (2015), *Algorithm for Retrieval of Remote Sensing Relectance from Satellite Ocean Color Sensors*, NASA Ocean Biology Processing Group.

Frouin, R., M. Schwindling, and P.-Y. Deschamps (1996), Spectral reflectance of sea foam in the visible and near-infrared: In situ measurements and remote sensing implications, *J. Geophys. Res.*, *101*(C6), 14361–14371, doi:10.1029/96JC00629.

Goddijn-Murphy, L., D. K. Woolf, and A. H. Callaghan (2011), Parameterizations and algorithms for oceanic whitecap coverage, *Journal of Physical Oceanography*, *41*(4), 742–756.

Gordon, H. R. (1997), Atmospheric correction of ocean color imagery in the Earth Observing System era, *J. Geophys. Res.*, *102*(D14), 17081–17106, doi:10.1029/96JD02443.

Gordon, H. R., and M. Wang (1994), Influence of oceanic whitecaps on atmospheric correction of ocean-color sensors, *Applied Optics*, *33*(33), 7754–7763.

Hanson, J. L., and O. M. Phillips (1999), Wind Sea Growth and Dissipation in the Open Ocean, *J. Phys. Oceanogr.*, *29*(8), 1633–1648, doi:10.1175/1520-0485(1999)029<1633:WSGADI>2.0.CO;2.

Ho, D. T., C. L. Sabine, D. Hebert, D. S. Ullman, R. Wanninkhof, R. C. Hamme, P. G. Strutton, B. Hales, J. B. Edson, and B. R. Hargreaves (2011), Southern Ocean Gas Exchange Experiment: Setting the stage, *J. Geophys. Res.*, *116*, C00F08, doi:10.1029/2010JC006852.

Hooker, S. B., L. Van Heukelem, C. S. Thomas, H. Claustre, J. Ras, R. Barlow, H. Sessions, L. Schlüter, J. Perl, and C. Trees (2005), *Second SeaWiFS HPLC Analysis Round-robin Experiment (SeaHARRE-2)*, National Aeronautics and Space Administration, Goddard Space Flight Center.

Johnson, B. D., and R. C. Cooke (1980), Organic Particle and Aggregate Formation Resulting from the Dissolution of Bubbles in Seawater, *Limnology and Oceanography*, *25*(4), 653–661.

Johnson, B. D., and R. C. Cooke (1981), Generation of Stabilized Microbubbles in Seawater, *Science*, *213*(4504), 209 –211.

Jonasz, M., and G. Fournier (2011), *Light Scattering by Particles in Water: Theoretical and Experimental Foundations: Theoretical and Experimental Foundations*, Academic Press.

Koepke, P. (1984), Effective reflectance of oceanic whitecaps, *Appl. Opt.*, *23*(11), 1816–1824.

Kokhanovsky, A. A. (2004), Spectral reflectance of whitecaps, *J. Geophys. Res.*, *109*(C5), C05021, doi:10.1029/2003JC002177.

Lance, V. P., P. G. Strutton, R. D. Vaillancourt, B. R. Hargreaves, J.-Z. Zhang, and J. Marra (Submitted), Primary productivity, new productivity and carbon export during two Southern Ocean Gas Exchange (SO GasEx) tracer experiments, *J. Geophys. Res.*

Lance, V. P., P. G. Strutton, R. D. Vaillancourt, B. R. Hargreaves, J.-Z. Zhang, and J. Marra (2012a), Primary productivity, new productivity, and their relation to carbon flux during two Southern Ocean Gas Exchange tracer experiments, *J. Geophys. Res.*, *117*(C4), C00F14, doi:10.1029/2011JC007687.

Lance, V. P., P. G. Strutton, R. D. Vaillancourt, B. R. Hargreaves, J.-Z. Zhang, and J. Marra (2012b), Primary productivity, new productivity, and their relation to carbon flux during two Southern

Ocean Gas Exchange tracer experiments, *J. Geophys. Res.*, *117*(C4), C00F14, doi:10.1029/2011JC007687.

Lee, M. E., and M. R. Lewis (2003), A New Method for the Measurement of the Optical Volume Scattering Function in the Upper Ocean, *J. Atmos. Oceanic Technol.*, *20*(4), 563–571, doi:10.1175/1520-0426(2003)20<563:ANMFTM>2.0.CO;2.

Lee, Z., K. L. Carder, and R. A. Arnone (2002), Deriving Inherent Optical Properties from Water Color: a Multiband Quasi-Analytical Algorithm for Optically Deep Waters, *Appl. Opt.*, *41*(27), 5755–5772.

Lee, Z., Y.-H. Ahn, C. Mobley, and R. Arnone (2010), Removal of surface-reflected light for the measurement of remote-sensing reflectance from an above-surface platform, *Optics Express*, *18*(25), 26313–26324.

Lee, Z., V. P. Lance, S. Shang, R. Vaillancourt, S. Freeman, B. Lubac, B. R. Hargreaves, C. Del Castillo, R. Miller, and M. Twardowski (2011), An assessment of optical properties and primary production derived from remote sensing in the Southern Ocean (SO GasEx), *Journal of Geophysical Research: Oceans (1978–2012)*, *116*(C4).

Lemire, D. (2006), Streaming maximum-minimum filter using no more than three comparisons per element, *arXiv preprint cs/0610046*.

Liss, P. S., and L. Merlivat (1986), Air-sea gas exchange rates: introduction and synthesis, in *The Role of Air-Sea Exchange in Geochemical Cycling*, edited by P. Buat-Menard, pp. 113–129, Reidel, Washington.

Longhurst, A., S. Sathyendranath, T. Platt, and C. Caverhill (1995), An estimate of global primary production in the ocean from satellite radiometer data, *Journal of Plankton Research*, *17*(6), 1245–1271.

Maritorena, S., D. A. Siegel, and A. R. Peterson (2002), Optimization of a semianalytical ocean color model for global-scale applications, *Appl. Opt.*, *41*(15), 2705–2714.

Miller, R. L., M. Belz, C. Del Castillo, and R. Trzaska (2002), Determining CDOM absorption spectra in diverse coastal environments using a multiple pathlength, liquid core waveguide system, *Continental Shelf Research*, *22*(9), 1301–1310.

Mitchell, B. G., and O. Holm-Hansen (1991), Observations of modeling of the Antartic phytoplankton crop in relation to mixing depth, *Deep Sea Research Part A. Oceanographic Research Papers*, *38*(8), 981–1007.

Mobley, C. D. (1994), *Light and Water*, Academic Press, San Diego, CA.

Monahan, E. (1993), Occurrence and Evolution of Acoustically Relevant Sub-Surface Bubble Plumes and their Associated, Remotely Monitorable, Surface Whitecaps, in *Natural Physical Sources of Underwater Sound*, edited by B. R. Kerman, pp. 503–517, Springer Netherlands.

Monahan, E. C. (1989), From the laboratory tank to the global ocean, *The climate and health implications of bubble-mediated sea-air exchange*, 43–63.

Monahan, E. C., and H. G. Dam (2001), Bubbles: An estimate of their role in the global oceanic flux of carbon, *J. Geophys. Res.*, *106*(C5), 9377–9383, doi:10.1029/2000JC000295.

Monahan, E. C., and M. Lu (1990), Acoustically relevant bubble assemblages and their dependence on meteorological parameters, *Oceanic Engineering, IEEE Journal of*, *15*(4), 340–349, doi:10.1109/48.103530.

Monahan, E. C., and C. F. Monahan (1986), The Influence of Fetch on Whitecap Coverage as Deduced from the Alte Weser Lightstation Observer's Log, in *Oceanic Whitecaps*, vol. 2, edited by E. Monahan and G. Niocaill, pp. 275–277, Springer Netherlands.

Monahan, E. C., and I. Muircheartaigh (1980), Optimal Power-Law Description of Oceanic Whitecap Coverage Dependence on Wind Speed, *J. Phys. Oceanogr.*, *10*(12), 2094–2099, doi:10.1175/1520-0485(1980)010<2094:OPLDOO>2.0.CO;2.

Monahan, E. C., and M. C. Spillane (1984), The role of oceanic whitecaps in air sea gas exchange, in *Gas Transfer at Water Surfaces*, edited by W. Brutsaert and G. H. Jirka, pp. 495–504, D. Reidel, Norwell, MA.

Monahan, E. C., and D. K. Woolf (1989), Comments on "Variations of Whitecap Coverage with Wind stress and Water Temperature, *J. Phys. Oceanogr.*, *19*(5), 706–709, doi:10.1175/1520-0485(1989)019<0706:COOWCW>2.0.CO;2.

Monahan, E. C., and C. R. Zietlow (1969), Laboratory comparisons of fresh-water and salt-water whitecaps, *J. Geophys. Res.*, *74*(28), 6961–6966, doi:10.1029/JC074i028p06961.

Monahan, E. C., P. Bowyer, D. Doyle, M. Higgins, and D. K. Woolf (1984), *Whitecaps and the marine atmosphere*, University College Rep. 7, Galway, Ireland.

Monahan, E. C., D. E. Spiel, and K. L. Davidson (1986), A model of marine aerosol generation via whitecaps and wave disruption, in *Oceanic whitecaps*, pp. 167–174, Springer.

Moore, K. D., K. J. Voss, and H. R. Gordon (1998), Spectral Reflectance of Whitecaps: Instrumentation, Calibration, and Performance in Coastal Waters, *J. Atmos. Oceanic Technol.*, *15*(2), 496–509, doi:10.1175/1520-0426(1998)015<0496:SROWIC>2.0.CO;2.

Moore, K. D., K. J. Voss, and H. R. Gordon (2000), Spectral reflectance of whitecaps: Their contribution to water-leaving radiance, *J. Geophys. Res.*, *105*(C3), 6493–6499, doi:10.1029/1999JC900334.

Mueller, J. L. et al. (2003), Ocean optics protocols for satellite ocean color sensor validation, revision 4, volume III: Radiometric Measurements and Data Analysis Protocols, edited by J. L. Mueller, G. S. Fargion, and C. R. McClain, *NASA Tech. Memo*, 01674–0.

Mueller, J. L., G. S. Fargion, C. R. McClain, J. Mueller, S. Brown, D. Clark, B. Johnson, H. Yoon, K. Lykke, and S. Flora (2004), *Ocean Optics Protocols For Satellite Ocean Color Sensor Validation, Revision 5, Volume VI: Special Topics in Ocean Optics Protocols, Part 2*, NASA Report 211621, 2003, 1-36.

Nordberg, W., J. Conaway, D. B. Ross, and T. Wilheit (1971), Measurements of microwave emission from a foam-covered, wind-driven sea, *Journal of the Atmospheric Sciences*, *28*(3), 429–435.

O'Reilly, J. E., S. Maritorena, D. A. Siegel, M. C. O'Brien, D. Toole, B. G. Mitchell, M. Kahru, F. P. Chavez, P. Strutton, and G. F. Cota (2000), Ocean color chlorophyll a algorithms for SeaWiFS, OC2, and OC4: Version 4, *SeaWiFS postlaunch calibration and validation analyses, Part*, *3*, 9–23.

Petzold, T. J. (1972), *Volume scattering functions for selected ocean waters*, DTIC Document.

Randolph, K., H. M. Dierssen, M. Twardowski, A. Cifuentes-Lorenzen, and C. J. Zappa (2014), Optical measurements of small deeply penetrating bubble populations generated by breaking waves in the Southern Ocean, *J. Geophys. Res. Oceans*, n/a–n/a, doi:10.1002/2013JC009227.

Reynolds, R. A., D. Stramski, and B. G. Mitchell (2001), A chlorophyll-dependent semianalytical reflectance model derived from field measurements of absorption and backscattering coefficients

within the Southern Ocean, *Journal of Geophysical Research: Oceans (1978–2012)*, *106*(C4), 7125–7138.

Roesler, C. S., and E. Boss (2002), A novel relfectance inversion model: retrieval of beam attenuation coefficients and particle size ditributions from ocean color, Office of Naval Research, Santa Fe, NM.

Ross, D. B., and V. Cardone (1974), Observations of oceanic whitecaps and their relation to remote measurements of surface wind speed, *Journal of Geophysical Research*, *79*(3), 444–452.

Scanlon, B., and B. Ward (2013), Oceanic wave breaking coverage separation techniques for active and maturing whitecaps, *Methods in Oceanography*, *8*(0), 1–12, doi:10.1016/j.mio.2014.03.001.

Stabeno, P. J., and E. C. Monahan (1986), The influence of whitecaps on the albedo of the sea surface, in *Oceanic Whitecaps and Their Role in Air-Sea Exchange Processes*, edited by E. C. Monahan and G. Mac Niocaill, pp. 261–266, Dordrecht, Holland.

Stramska, M., and T. Petelski (2003), Observations of oceanic whitecaps in the north polar waters of the Atlantic, *J. Geophys. Res.*, *108*(C3), 3086, doi:10.1029/2002JC001321.

Stramski, D., and J. Tegowski (2001), Effects of intermittent entrainment of air bubbles by breaking wind waves on ocean reflectance and underwater light field, *J. Geophys. Res.*, *106*(C12), 31345–31360, doi:10.1029/2000JC000461.

Stramski, D., R. A. Reynolds, M. Kahru, and B. G. Mitchell (1999), Estimation of particulate organic carbon in the ocean from satellite remote sensing, *Science*, *285*(5425), 239–242.

Sugihara, Y., H. Tsumori, T. Ohga, H. Yoshioka, and S. Serizawa (2007), Variation of whitecap coverage with wave-field conditions, *Journal of Marine Systems*, *66*(1), 47–60.

Terrill, E. J., W. K. Melville, and D. Stramski (1998), Bubble entrainment by breaking waves and their effects on the inherent optical properties of the upper ocean.

Terrill, E. J., W. K. Melville, and D. Stramski (2001), Bubble entrainment by breaking waves and their influence on optical scattering in the upper ocean, *J. Geophys. Res.*, *106*(C8), 16815–16823, doi:10.1029/2000JC000496.

Thorpe, S. A. (1982), On the Clouds of Bubbles Formed by Breaking Wind-Waves in Deep Water, and their Role in Air -- Sea Gas Transfer, *Philosophical Transactions of the Royal Society of London. Series A, Mathematical and Physical Sciences*, *304*(1483), 155–210.

Twardowski, M., X. Zhang, S. Vagle, J. Sullivan, S. Freeman, H. Czerski, Y. You, L. Bi, and G. Kattawar (2012), The optical volume scattering function in a surf zone inverted to derive sediment and bubble particle subpopulations, *J. Geophys. Res.*, *117*(C7), C00H17, doi:10.1029/2011JC007347.

Wang, Q., E. Monahan, W. Asher, and P. Smith (1995), Correlations of whitecap coverage and gas transfer velocity with microwave brightness temperature for plunging and spilling breaking waves, *Air-Water Gas Transfer*, 217–225.

Welschmeyer, N. A. (1994), Fluorometric analysis of chlorophyll a in the presence of chlorophyll b and pheopigments, *Limnology and Oceanography*, *39*(8), 1985–1992.

Whitlock, C. H., D. S. Bartlett, and E. A. Gurganus (1982), Sea foam reflectance and influence on optimum wavelength for remote sensing of ocean aerosols, *Geophys. Res. Lett.*, *9*(6), 719–722, doi:10.1029/GL009i006p00719.

Woolf, D. K. (2005), Parametrization of gas transfer velocities and sea-state-dependent wave breaking, *Tellus B*, *57*(2), 87–94, doi:10.1111/j.1600-0889.2005.00139.x.

Woolf, D. K., and S. A. Thorpe (1991), Bubbles and the air-sea exchange of gases in near-saturation conditions, *Journal of Marine Research*, *49*(3), 435–466, doi:10.1357/002224091784995765.

Wright, S., S. Jeffrey, and R. Mantoura (2005), *Phytoplankton pigments in oceanography: guidelines to modern methods*, Unesco Pub.

Wu, J. (1983), Sea-Surface Drift Currents Induced by Wind and Waves, *J. Phys. Oceanogr.*, *13*(8), 1441–1451, doi:10.1175/1520-0485(1983)013<1441:SSDCIB>2.0.CO;2.

Yount, D. E. (1982), On the evolution, generation, and regeneration of gas cavitation nuclei, *The Journal of the Acoustical Society of America*, *71*(6), 1473–1481.

Zaneveld, J. R. V., and H. Pak (1973), Method for the determination of the index of refraction of particles suspended in the ocean, *JOSA*, *63*(3), 321–324.

Zappa, C. J., M. L. Banner, H. Schultz, J. R. Gemmrich, R. P. Morison, D. A. LeBel, and T. Dickey (2012), An overview of sea state conditions and air-sea fluxes during RaDyO, *Journal of Geophysical Research: Oceans (1978–2012)*, *117*(C7).

Zhang, X., Marlon Lewis, M. Lee, B. Johnson, and G. Korotaev (2002), The Volume Scattering Function of Natural Bubble Populations, *Limnology and Oceanography*, *47*(5), 1273–1282.

Zhang, X., M. Lewis, W. P. Bissett, B. Johnson, and D. Kohler (2004), Optical Influence of Ship Wakes, *Appl. Opt.*, *43*(15), 3122–3132, doi:10.1364/AO.43.003122.

Zhang, X., L. Hu, and M.-X. He (2009), Scattering by pure seawater: effect of salinity, *Optics Express*, *17*(7), 5698–5710.

Zhang, X., M. Twardowski, and M. Lewis (2011), Retrieving composition and sizes of oceanic particle subpopulations from the volume scattering function, *Appl. Opt.*, *50*(9), 1240–1259.

Zhao, D., and Y. Toba (2001), Dependence of whitecap coverage on wind and wind-wave properties, *Journal of oceanography*, *57*(5), 603–616.